Studies on the Effect of Gas Contaminations in Micromegas Detectors and Production of Micromegas Detectors for the New Small Wheel of the ATLAS Detector

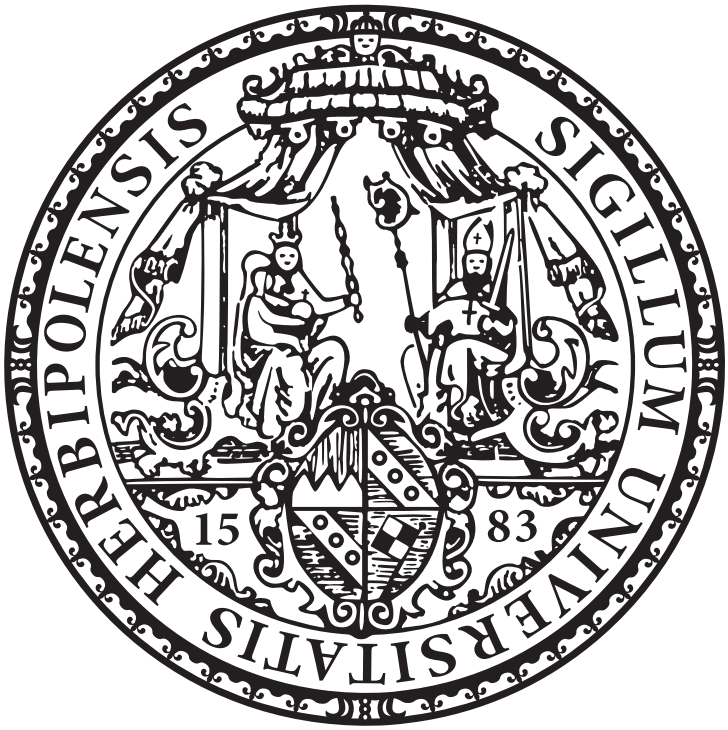

Dissertation zur Erlangung des naturwissenschaftlichen Doktorgrades der Julius-Maximilians-Universität Würzburg

vorgelegt von

Thorben Swirski

aus

Freiburg im Breisgau

Würzburg, 2021

Eingereicht am:
bei der Fakultät für Physik und Astronomie

1. Gutachter: Prof. Dr. Raimund Ströhmer
2. Gutachter:
3. Gutachter:
der Dissertation

Vorsitzender:
1. Prüfer:
2. Prüfer:
3. Prüfer:
im Promotionskolloquium

Tag des Promotionskolloquiums:

Doktorurkunde ausgehändigt am:

Studies on the Effect of Gas Contaminations in Micromegas Detectors and Production of Micromegas Detectors for the New Small Wheel of the ATLAS Detector

Thorben Swirski

June 14, 2021

Contents

Zusammenfassung

Diese Arbeit beinhaltet zwei Teile. Zum einen behandelt sie die Simulation und die Messung des Effekts von Verunreinigungen des Detektorgases auf Teilchendetektoren, im speziellen vom Typ Micromegas. Zum anderen beinhaltet sie den Aufbau einer Produktionsstätte zur Vollendung von Driftpaneelen, die im ATLAS NSW Einsatz finden werden. Der erste Teil dieser Arbeit nimmt die Rolle eines Einführungsteiles ein, der die theoretischen Grundlagen von gasgefüllten Detektoren bespricht.

Die Effekte von Verunreinigungen des Detektorgases auf Micromegas

Gasgefüllte Teilchendetektoren existieren mittlerweile seit mehr als einhundert Jahren. Die wohl bekannteste Variante ist das Geiger-Müller-Zählrohr. Moderne Teilchendetektoren benutzen das gleiche Prinzip der Gasverstärkung wie ihre Vorgänger, allerdings besitzen sie einige Anpassungen an die Anforderungen moderner Experimente der Teilchenphysik, wie niedrigere Totzeit oder feinere Ortsauflösung. Zur gleichen Zeit werden die Grenzen der Gasverstärkung immer weiter ausgenutzt, wodurch die Effekte von Verunreinigungen des Detektorgases eine immer größere Rolle spielen. Da bisher nur wenige quantitative Messungen zu diesem Thema existieren, wurde diese Arbeit angefertigt. Die Effekte wurden zuerst durch eine Simulation vorhergesagt, um eine Größenordnung der üblichen Konzentrationen und deren Auswirkungen auf den Detektor zu bekommen. Der am Lehrstuhl für Physik und ihre Didaktik befindliche Messraum wurde daraufhin erweitert, um Micromegas Detektoren benutzen zu können. Außerdem wurde das Gassystem erweitert, sodass Verunreinigungen von Sauerstoff und Wasser dem Detektorgas selbst in geringsten Mengen hinzugefügt werden können und auch Quellen für diese Kontaminationen gemessen werden können. Um die neuen Detektoren auslesen zu können, mussten neue Ausleseelektronik angeschafft werden. Außerdem wurde die Hochspannungsversorgung um eine Karte erweitert, die in der Lage ist, niedrige Ströme zu messen, sodass die Hochspannungsstabilität der Detektoren untersucht werden konnte. Der zweite Teil dieser Arbeit beschäftigt sich mit diesen Untersuchungen.

Contents

Bau von Micromegas Detektoren für das ATLAS NSW

Der ATLAS-Detektor am LHC wurde von 2003 bis 2008 für die erste Stufe des LHC-Projektes gebaut. Im Zuge der Verbesserungen im Projekt *High-Luminosity*-LHC muss auch der Detektor den neuen Gegebenheiten, wie Raten und Strahlungintensität, angepasst werden. Ein Detektorsubsystem, das *Small Wheel* wird dabei komplett ausgetauscht und durch das *New Small Wheel* (NSW) ersetzt. Dabei werden zwei Detektortechnologien eingesetzt, small-strip thin gap chambers (sTGC) und Micromegas. Der Bau der Detektorkomponenten ist auf Universitäten auf der ganzen Welt verteilt. Während die sTGC aufgrund ihrer Größe leichter zu transportieren sind, sind die großen Micromegas-Module weit schwieriger zu transportieren. Deswegen wurde die Arbeit an sTGC von Universitäten außerhalb Europas durchgeführt, während die Micromegas in Europa hergestellt wurden. Von den vier verschiedenen Geometrien an Micromegas-Detektoren für das NSW wurde eine, das SM2, in einer Kollaboration deutscher Universitäten hergestellt. Würzburg erhielt hierbei die Aufgabe, die in Mainz hergestellten und in München veredelten Driftpaneele mit einem Micromesh zu bestücken. Um die von der ATLAS-Kollaboration geforderte Taktzahl von einem Paneel pro Woche zu gewährleisten, musste eine Produktionslinie in einem zur Universität Würzburg gehörendem Reinraum aufgebaut werden. Außerdem mussten Handgriffe und Prozeduren standardisiert werden, um eine gleichbleibende und vorhersehbare Qualität zu gewährleisten, so dass diese Paneele in München dann mit den entsprechenden Auslesepaneelen zu ganzen Modulen verheiratet werden können, die zuverlässig gleiche Eigenschaften zeigen. Neben dem Aufbau dieser Produktionsstätte werden auch noch die Untersuchungen bezüglich der Meshqualität und -handhabung besprochen, die notwendig waren, als einzelne technische Probleme mit den fertigen Modulen auftraten, die vorher nicht bekannt waren. Der letzte Teil dieser Arbeit ist der Produktion der SM2 gewidmet.

Abstract

This work consists of two parts. On the one hand, it describes simulation and measurement of the effect of contaminations of the detector gas on the performance of particle detectors, with special focus on Micromegas detectors. On the other hand, it includes the setup of a production site for the finalization of drift panels which are going to be used in the ATLAS NSW. The first part augments these two parts to give an introdution into the theoretical fundations of gaseous particle detectors.

Effects of Contaminations on Micromegas Detectors

By now, gaseous particle detectors exist for more than 100 years. The most known variant is the Geiger-Müller-Counter. Modern particle detectors use the same basic principle of gas amplification as their predecessors, but contain several improvements to accomodate the new requirements for modern experiments in particle physics, like lower dead times or better spatial resolution. At the same time, the physical limitation of gas amplification are exhausted more and more, because of which the effects of contaminants in the detector gas play more and more of a role. Since only very few quantitative measurements exist, this work was performed. The effects were first predicted using simulations so that an order of magnitude for the concentrations of the contaminants that are needed to cause a degradation of the detector could be gauged. The measurement room belonging to the Chair for Physics and its Didactics was augmented such that new Micromegas detectors could be used for measurements. In addition, the gas system was expanded to allow both oxygen and water contents in the detector gas could both be measured precisely and also added in very small quantities. Also, sources for contaminants in detector setups can be identified that way. Not only were new readout electronics added to the lab to allow for Micromegas detectors, but the high voltage supply was augmented. A new power supply card was added which allowed to measure lower voltages and made it possible to investigate the high voltage stability of the detectors. The second part of the thesis is dedicated to these topics.

Construction of Micromegas Detectors for the ATLAS NSW

The ATLAS detector at the LHC was built from 2003 to 2008 for the first stage of the LHC research project. For the upgrade called *High-Luminosity*-LHC the detectors also need to be upgraded to be able to cope with the new enivronment, like high rates and the requirement for radiation hardness. One of the detector subsystems, the *Small Wheel* is being completely replaced by the *New Small Wheel*. The NSW uses new detector technologies, small-strip thin gap chambers and Micromegas. The construction of the detector modules is split among universities around the world. While the sTGC modules are smaller and easier to transport, the larger Micromegas modules are by far harder to move around. As such the work on sTGCs was performed by universities outside of Europe, while the Micromegas detectors were built in Europe. Of the four different geometries of Micromegas-Modules for the NSW, one of them, the SM2, was constructed by a collaboration of German universities. In this project, the University of Würzburg performed the finalisation, transfering the mesh onto drift panels, which had been built in Mainz and prepared for transfer in Munich. To be able to produce panels at the rate of one per week, as requested by the ATLAS collaboration, a dedicated production line had to be set up in the cleanroom provided by the University of Würzburg. Procedures and tasks had to be standardized to guarantee a high and constant quality, so that the panels could be used with the corresponding readout panels for assembly into modules in Munich which always exhibit the same properties. In addition to the set up of the production line and procedures, this part will also explain the investigations into the mesh quality and handling that became necessary as some unexpected technical problems with finished panels occured. The last part of this thesis is dedicated to the construction of the SM2.

Part I.

Introduction

1. Motivation

Gaseous particle detectors are widely used in particle physics. As such, interest in detector developement for this class of detectors is high. Newer technologies, like MicroPattern Gaseous Detectors (MPGD) are beginning to replace technologies like the Monitored Drift Tube (MDT) in applications where low dead times and high spatial resolution are required. These technologies are still relatively new and are still experiencing high degrees of research and developement. The Chair for Physics and Didactics of the University of Würzburg is part of these research efforts. Especially in recent times, many questions about these new technologies, like high voltage stability and stability against gas contaminations, have arisen. Especially the gas contaminations cannot be easily investigated without a specialised lab, since adding contaminants in a controlled way in the low concentrations needed poses significant problems. As such, a goal of this thesis was to create such a lab and investigate the effects of oxygen and water on micropattern detectors more closely. These investigations are becoming more important as new detector technologies get used in experiments. Many experiments do not allow access to the detector for prolonged periods of time, so knowing the properties of a detector beforehand, and knowing how to recalibrate if necessary, becomes paramount for a successful measurement.

To access new physics and rarer processes, the LHC has a long and broad update schedule reaching into the late 2020s, see figure 1.1. The high-luminosity LHC project will increase the rates of charged particles, especially in the forward parts of the detectors, from 2027 onwards. Therefore, the ATLAS collaboration decided to replace their Small Wheel with a new one that is able to cope with the new high-rate environment. To achieve this, the New Small Wheel (NSW) will incorporate Micromegas technology, a first in the history of the ATLAS detector. Construction of these Micromegas modules is underway in several European countries, including Germany. The Würzburg group has contributed to this effort by joining in the construction of one of the Micromegas modules, the SM2. To be able to produce modules of reliable quality, the processes had to be devised and documented in such a way that they could be repeated again and again, giving the same results every time. At the same time, new challenges that arose from the novel technologies in conjunction with the never before achieved module sizes of several square meters had to be confronted and the processes used in the detector production adapted so that the performance of the detector modules can be guaranteed.

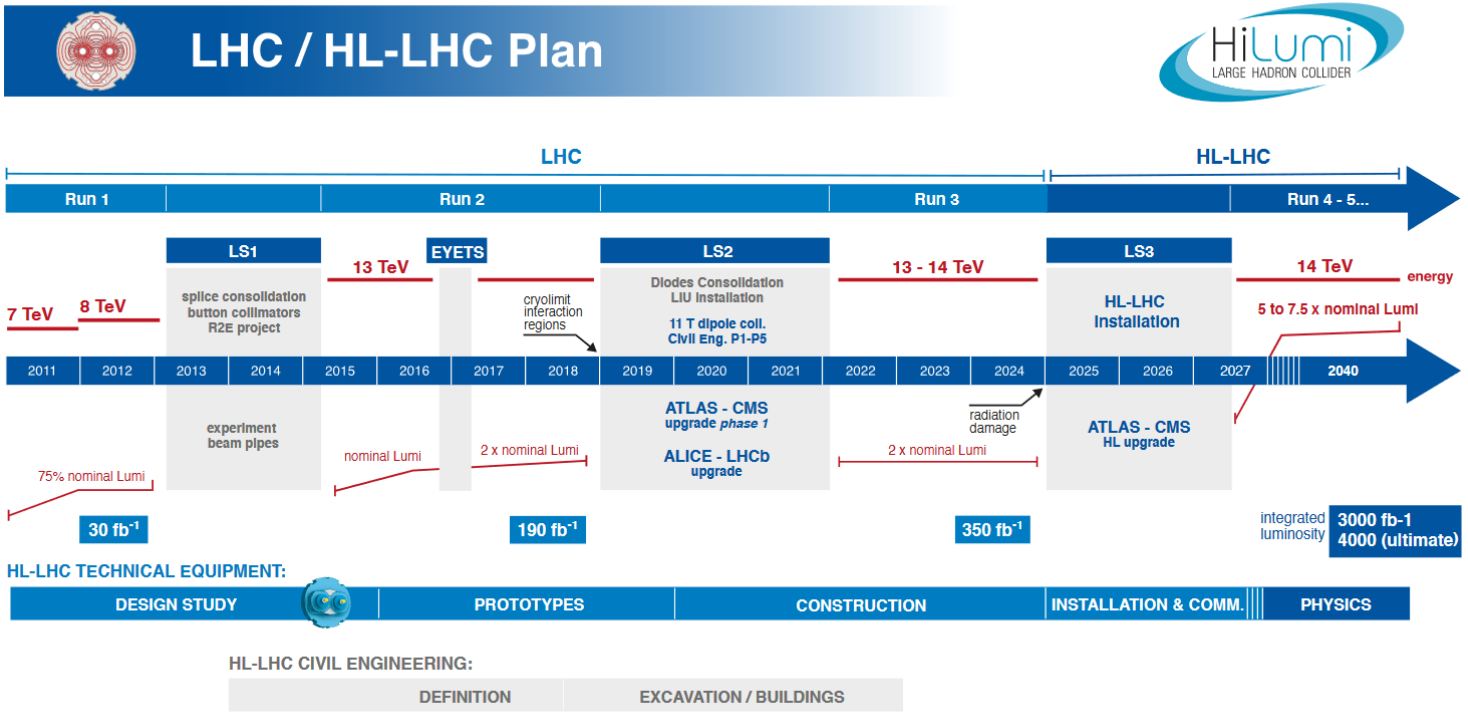

Figure 1.1.: Schedule of the LHC project. The upgrade to the high-luminosity LHC will take place starting around 2025, as of August 2020, from [1]

2. Gaseous Particle Detectors

One of the first gaseous particle detectors was proposed by Hans Geiger in 1908[2]. An improved version, the Geiger-Müller counter, is still well-known and used today[3]. Since then, many different types of gaseous particle detectors, all using more or less the same basic principles, have been developed. These basic principles of particle-matter-interaction in gaseous detectors will be discussed in this chapter, including a look at the Geiger-Müller counter, which will also be used to explain several physical processes that influence signal formation in gaseous detectors. In addition, a closer look into one modern development, the MicroPattern Gaseous Detectors (MPGD), will be taken. Different kinds of MPGD will also be discussed. To conclude the chapter, effects of contaminations on MPGDs are being highlighted.

2.1. Interaction of Radiation with Matter

Discussions about the interactions of particles and matter have filled many books over the more than a century of active developement. As such, this chapter is just giving an overview over this topic. For further reading, several textbooks [4, 5] are recommended. In gaseous detectors, the ionizing particles, charged or not, interact with the atoms in the gas creating primary charges by knocking electrons out of the shells of their respective atom. Naturally, one electron alone is hard to detect. Therefore, the signal needs to be amplified. This amplification often takes place in a different region of the detector, with the distance being covered by the elctrons *drifting*, a process that poses inherent challenges on its own. All three steps, ionization, drift and amplification, will be detailed further in the following.

2.1.1. Primary Ionisation

The primary ionization process depends on the properties of the particle like charge, mass and momentum, and the matter it is interacting with, the so called *active medium*. Due to its large size compared to the nucleus, interactions usually involve the electron shells of the atoms or molecules in the gases. Of special interest are the interactions with incident muons and photons, both of which are readily available for studies in a lab, via cosmic radiation or radioactive γ-sources,

respectively. Electromagnetic interactions with atoms generally take two forms, *exitation* and *ionization*. In the first case, the incident particle gives some or all of its kinetic energy to the atom, lifting one of the electrons to a higher bound state within in shell. This exited state can then decay via photon emission back to a lower state. The emitted lower energy photon can then be detected. For gaseous detectors, ionizing interactions are of special importance. If the energy given to an electron in the atom's shell is high enough, it will not be lifted to a bound state, but into the unbound continuum, i.e. the atom will be broken up into an ion and a free electron. Starting from these basic points, the discussion will now focus on charged, non-hadronic particles and photons separately. In addition, there are several other mechanisms of energy loss which will be discussed in their respective sections.

Charged Particles

Of special interest for gaseous detectors in the context of high energy physics are non-hadronic particles. As such, this thesis will not cover hadrons. The important charged particles are muons, which are able to escape the inner layers of a typical detector and can then be detected by the muon spectrometer on the outside. In comparison, electrons will be discussed, as their interaction is substantially different from the one of massive particles. In general, four different mechanism of energy loss in matter can be identified. Ionization describes the energy transfer of the particle to an electron in the shell of one of the atoms, giving it enough energy to be freed. Bremsstrahlung (from German, meaning decelerating radiation) describes the energy loss due to radation emitted by charged particles that change their direction or speed of travel. Given enough energy and matter to interact with, a particle can also create a pair of electrons and positrons. While very unlikely, the particle can also interact with the nucleus of the matter it is passing through, scattering elastically.

Ionization If an incident particle hits an atom of the matter it passes through, it can scatter inelastically with it. In this case, one of the electrons inside the shell of the atom will be exited. If this exitation is strong enough, the electron will be freed from the atom, creating an ion electron pair. The kinetic energy of the resulting electron can be calculated as

$$E_{\text{kin}}^{\text{max}} = \frac{2m_e p^2}{m_0^2 + m_e^2 + 2m_e E/c^2}, \tag{2.1}$$

with m_0 being the mass, E the kinetic energy, and p the momentum of the incident particle, and m_e the electron mass. If the kinetic energy of the incident particle is

small enough and the particle itself heavier than an electron, the equation can be simplified to

$$E_{\text{kin}}^{\max} \approx 2m_e c^2 \beta^2 \gamma^2, \tag{2.2}$$

with $\beta = {}^{v}/_{c}$ and $\gamma = {}^{1}/\sqrt{1-\beta^2}$. For highly relativistic muons, the equation becomes

$$E_{\text{kin}}^{\max} = \frac{E^2}{E + 11\text{GeV}}. \tag{2.3}$$

For an electron as incident particle, one can get

$$E_{\text{kin}}^{\max} = \frac{p^2}{m_e + E/c^2} = E - m_e c^2, \tag{2.4}$$

which is expected from classical head on collissions between two objects of the same mass. The above equation takes into account scattering on one nucleus, but the incident particle can scatter multiple times. As such, it makes sense to define the average loss of Energy in a given length of material[6–12]:

$$-\frac{dE}{dx} = 4\pi N_A r_e^2 m_e c^2 z^2 \frac{Z}{A} \frac{1}{\beta^2} \left(\ln \frac{2m_e c^2 \gamma^2 \beta^2}{I} - \beta^2 - \frac{\delta}{2} \right). \tag{2.5}$$

z is the charge of the incident particle in units of the elementary charge, Z,A the atomic number and number of nucleons of the material, r_e the classical radius of the electron, N_A the Avogadro constant, I the mean excitation energy, a material property of the absorber, which can be approximated as $I = 16Z^{0.9}\text{eV}$ for $Z > 1$, and δ a screening effect of other electrons in the nucleus, which can be neglected in gases under normal pressure. Using 2.1.1 and using κ for the factors in front yields the well-known *Bethe-Bloch formula*[9]:

$$-\frac{dE}{dx} = \kappa \frac{1}{\beta^2} \left(\ln \frac{E_{\text{kin}}^{\max}}{I} - \beta^2 - \frac{\delta}{2} \right). \tag{2.6}$$

As can be seen in figure 2.1, the energy loss decreases with $1/\beta^2$ until is reaches a plateau near $\beta\gamma \approx 4$. Particles with energies in this plateau region are called *minimally ionizing particles*. After $\gamma > 4$, the lograthmic expression in the exquation causes the loss to increase again. The formula given here does not take into account any other loss mechanism than ionization. The Bethe-Bloch equation is a measure for the average loss. If the absorber is small, the absorbed energy can vary wildly and can be approximated by the *Landau distribution*[14–16], which can itself be approximated by

$$L(\lambda) = \frac{1}{\sqrt{2\pi}} \exp\left(-\frac{1}{2} \left(\lambda + e^{-\lambda} \right) \right). \tag{2.7}$$

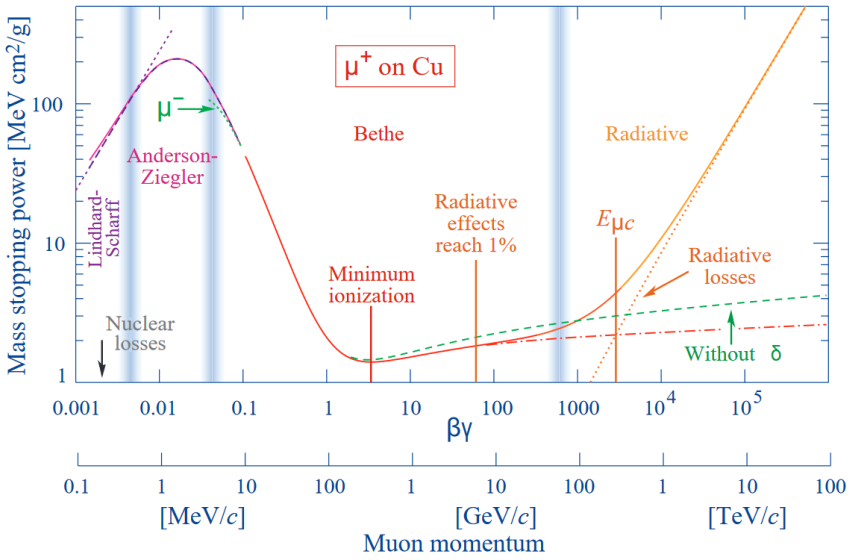

Figure 2.1.: Illustration of the energy loss depending on the energy for muons in copper, including the Bethe-Bloch formula in the medium energy range, from [13]

λ is the deviation from the most probable energy loss, defined as

$$\lambda = \frac{\Delta E - \Delta E^W}{\kappa \rho x}, \tag{2.8}$$

with ρ being the density and x being the length of the absorber. ΔE is the actual energy loss and ΔE^W is the most probable energy loss. This can be expressed by[13]

$$\Delta E^W = \kappa \rho x \left[\ln \left(\frac{2 m_e c^2 \gamma^2 \beta^2}{I} \right) + \ln \frac{\kappa \rho x}{I} + 0.2 - \beta^2 - \delta(\beta\gamma) \right]. \tag{2.9}$$

An example for an energy-loss distribution can be seen in fig. 2.2. When the incident particle is an electron, it and the shell electron are indistinguishible from each other. This means that the Bethe-Bloch formula needs to be modified. For electrons[17] it therefore takes the form of

$$-\frac{dE}{dx} = 4\pi N_A r_e^2 m_e c^2 \frac{Z}{A} \frac{1}{\beta^2} \left[\ln \frac{\gamma m_e c^2 \beta \sqrt{\gamma - 1}}{\sqrt{2} I} + \frac{1}{2}(1 - \beta^2) - \frac{2\gamma - 1}{2\gamma^2} \ln 2 + \frac{1}{16} \left(\frac{\gamma - 1}{\gamma} \right)^2 \right]. \tag{2.10}$$

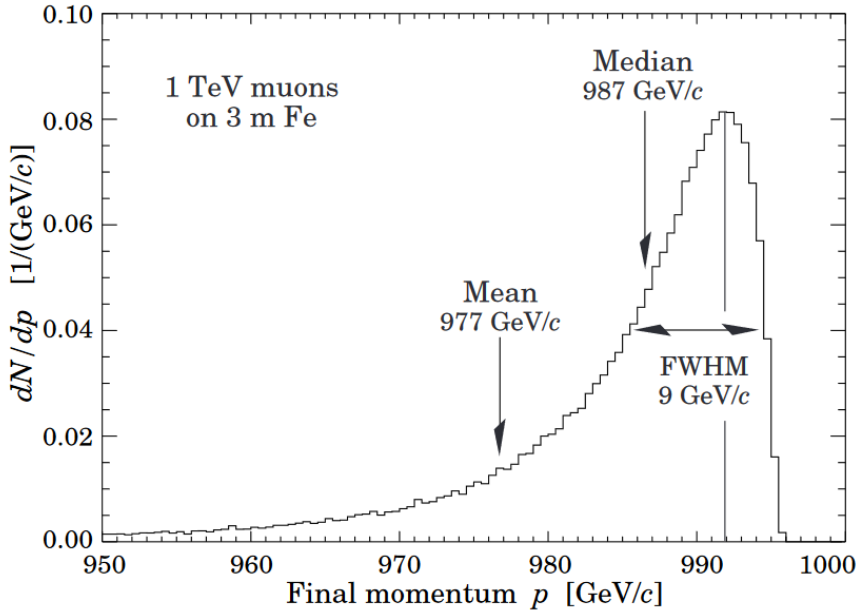

Figure 2.2.: Momentum distribution, or Energy minus Energy loss of 1 TeV muons after 3 m of iron, from[13]

Given a certain amount of energy deposited in the detector, one can find the amount of electrons created from that energy. This is a gain a statistical effect, but one can find that the width of the distribution is smaller than expected. The reason for that effect was first shown by Fano in 1947[18], who gave the *Fano factor* its name.

Bremsstrahlung When charges change their velocity, they radiate. In a medium, the different atoms and nuclei all have Coulomb fields in which particles can be accelerated. The emitted radiation then decelerates the incident particle, hence the name *Bremsstrahlung*[19]. This energy loss by the coulomb fields of the nuclei can be expressed by

$$-\frac{dE}{dx} \approx 4\alpha N_A \frac{Z^2}{A} z^2 \left(\frac{1}{4\pi\epsilon_0} \cdot \frac{e^2}{mc^2}\right)^2 E \ln \frac{183}{Z^{1/3}}. \tag{2.11}$$

α is the finestructure constant, z is the charge number, m is the mass and E is the energy of the incident particle. As one can see, the Bremsstrahlung is proportional to the energy of the incident particle becomes more important for lighter particles. Therefore, this is one of the most important contributions to the energy loss of electrons, while it plays a smaller role for muons or hadrons. Since this effect is so

important for electrons, one defines the *radiation length*, by using equation 2.11:

$$-\frac{dE}{dx} = \frac{E}{X_0} \tag{2.12}$$

From this follows

$$X_0 = \frac{A}{4\alpha N_A Z(Z+1) r_e^2 \ln(183 Z^{1/3})} \left\{\mathrm{g/cm^2}\right\}. \tag{2.13}$$

In this relation, the additional effects of the electrons in the shell of the atom are also taken into account, modifing the the Z^2 term into $Z(Z+1)$. This radiation length is a material property, but only valid for electrons as incident particles. In literature, the values usually given are for electron and the value for other particles can be estimated from there by scaling with m^2. By integration, one can estimate the energy of a singular particle in the absorber:

$$E = E_0 \; e^{x/X_0} \tag{2.14}$$

Cherenkov Radiation While a photon is travelling with a speed of c in a perfect vacuum, the speed of it becomes lower in a medium, $c' = c/n$, with n denoting the refractive index of the mediun. Depending on the medium's properties, light can slow down to a few tens of meters per second[20]. These speeds are of course exceptional, but even in any medium, the speed of the photon is smaller than c. Massive particles, however, are only limited by c, even in those media. This means that if a massive particle passes through a medium, it can be faster than the light speed in the medium. If the particle is charged, it will polarise the medium when crossing through it, causing what is called *Cherenkov Radiation* to be emitted if the particles speed v is larger than c/n[21]. While the polarisation also happens with $v < c/n$, it can accomodate the particles position quickly enough to cause a point symmetrical distribution which does not cause radiation. On larger speeds, the polarisation in the medium lags behind the particle itself, causing a cone of radiation to be emmited. The opening angle of this cone depends on the speed of the particle and the refractive index of the medium. From geometric arguments, one can obtain

$$\cos\theta_c = \frac{1}{n\beta} = \frac{c}{nv}, \tag{2.15}$$

which allows the definition of a threshold $\beta_c = 1/n$. Also, one can find the maximum angle of the radiation that can be emitted by any particle in the medium

$$\theta_c^{\max} = \arccos\frac{1}{n}. \tag{2.16}$$

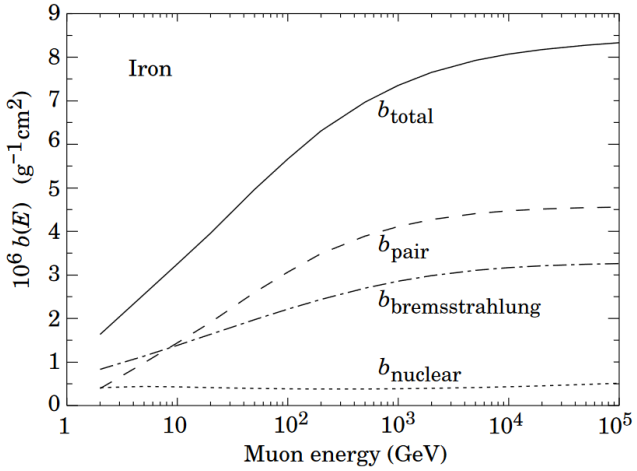

Figure 2.3.: Energy-loss b-factors for muons in iron, from [13]

As can be seen from the formula, the speed of any charged particle, even of unknown mass, can be found directly from the cherenkov radiation it emits in a medium of known properties.

Pair Production If the energy of the incident particle is large enough, more particles can be created by interactions with the Coulomb field created by the nucleus. The first accessible charged particle-antiparticle-pair is the electron/positron. The energy loss by this production is proportional to the energy of the incident particle:

$$-\left.\frac{dE}{dx}\right|_{pair} = b_{pair}(Z, A, E) \cdot E \tag{2.17}$$

Nuclear interactions The incident particle can also inelastically scatter with the nucleus. This process also leads to an energy loss that is proportional to the energy of the incident particle. The b-values for muons in iron are visualised in fig. 2.3

Interactions of Photons

The interaction of photons with matter is distinctly different from the interaction of charged particles. While a muon slows down further and further, a photon deposits the entirety of its energy in one interaction. This interaction has as certain probability to occur, expressed by the cross section σ, which is shown for lead in figure 2.4.

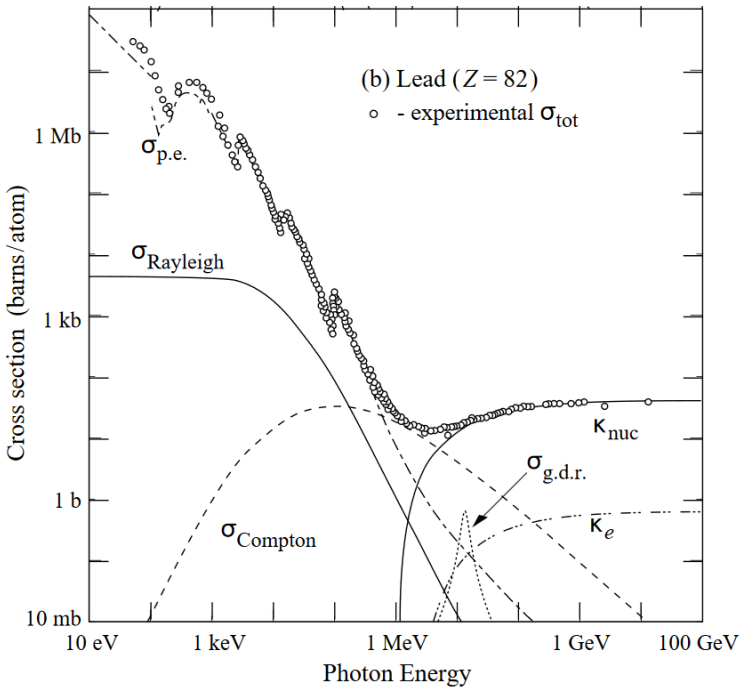

Figure 2.4.: Cross section of photons interacting with lead. P.e. is photoelectric effect, g.d.r. is *giant dipole resonance*, a breakup of the nucleus due to the interaction of with the photon. Rayleigh scattering does not lead to ionization and is therefore not of relevance to this work, from[13]

Different processes have different cross sections, with the total cross section being the sum of all partial ones:

$$\sigma = \sum_i \sigma_i \tag{2.18}$$

Given the intensity of the photon beam penetrating the material, I_0, one obtains an exponential attenuation for an area density $x = \rho l$ (with l a given length of the absorber),

$$I = I_0 e^{-\mu x}, \tag{2.19}$$

where μ, the *mass attenuation coefficient*, is given by

$$\mu = \frac{N_A}{A}\sigma, \tag{2.20}$$

with N_A being the Avogadro constant, and A being the atomic weight of the material. As was the case for the charged particles, the importance of the processes available to the photon, and therefore the mass attenuation, strongly depend on its energy. At low energies above the ionisation energy of the material but below 100 keV, the photoelectric effect dominates,

$$\gamma + \text{atom} \rightarrow \text{atom}^+ + e^-, \tag{2.21}$$

while the cross section in the range of medium photon energies of around 1 MeV is dominated by compton scattering of the photon on electrons in the atom,

$$\gamma + e^- \rightarrow \gamma + e^-. \tag{2.22}$$

For high photon energies, pair production takes the most dominant role,

$$\gamma + \text{nucleus} \rightarrow \text{nucleus} + e^- + e^+. \tag{2.23}$$

Photoelectric Effect Due to momentum conservation - free electrons can not absorb photons. In atoms, the nucleus is able to take some of the momentum, allowing one of the electrons to absorb the photon. Due to the requirement of having a third partner in the collision also facilitates a maximum likelyhood of around 80% for the electron in the K-shell to be the scattering partner of the photon. The total cross section away from absoprion edges and in the non-relativistic *Born approximation*[22] is given by

$$\sigma^K_{\text{photo}} = \left(\frac{32}{\epsilon^7}\right)^{1/2} \alpha^4 Z^5 \sigma^e_{\text{Th}}, \tag{2.24}$$

with $\epsilon = E_\gamma / m_e c^2$ being the reduced photon energy and $\sigma^e_{\mathrm{Th}} = \frac{8}{3}\pi r_e^2$ being the *Thomson cross section*, describing the elastic scattering of electrons and photons.

Compton Effect The compton effect is the elastic scattering of photons on atomic electrons. The electrons are assumed to be quasi-free, i.e. the binding energy of the electrons is neglected. The total cross-section[23] for this process can be expressed as

$$\sigma^e_c = 2\pi r_e^2 \left[\left(\frac{1+\varepsilon}{\varepsilon^2} \right) \left(\frac{2(1+\varepsilon)}{1+2\varepsilon} - \frac{1}{\varepsilon} \ln(1+2\varepsilon) \right) + \frac{1}{2\varepsilon} \ln(1+2\varepsilon) - \frac{1+3\varepsilon}{(1+2\varepsilon)^2} \right], \tag{2.25}$$

Where $\varepsilon = {}^{E_\gamma}/_{m_e c^2}$. This total cross-section is a per-electron cross-section. As such, the cross-section for an atom of atomic number Z is actually proportionally higher, i.e. $\sigma^Z_c = Z \cdot \sigma^e_c$. Also, for high energies, one can approximate this cross-section[24] as

$$\sigma^e_c \propto \frac{\ln \varepsilon}{\varepsilon}. \tag{2.26}$$

For the differential cross-section[25, 26], one can find

$$\frac{d\sigma^e_c}{d\Omega} = \frac{r_e^2}{2} \left(\frac{E'_\gamma}{E_\gamma} \right)^2 \left(\frac{E_\gamma}{E'_\gamma} - \frac{E'_\gamma}{E_\gamma} - \sin^2 \theta_\gamma \right), \tag{2.27}$$

where E_γ and E'_γ are the photon energies before and after the scattering, respectively and θ_γ is the scattering angle of the photon with respet to the incident direction. The photon energy ratio can then be expressed as

$$\frac{E'_\gamma}{E_\gamma} = \frac{1}{1+\varepsilon(1-\cos\theta_\gamma)}. \tag{2.28}$$

From this one can directly see that the maximum energy transfer occurs on *back scattering* ($\cos\theta_\gamma = -1$), and the formula becomes

$$\frac{E'_\gamma}{E_\gamma} = \frac{1}{1+2\varepsilon}. \tag{2.29}$$

While the compton scattering process might also occur with other particles than electrons. However, these usually do not play a major role in particle detection and are therefore not discussed further here. In addition, the *inverse compton effect*, the scattering of a high-energy electron on a low-energy photon with an

energy transfer from the electron to the photon, exists, which also plays no major role in particle detection.

Pair Production If the photon energy is high enough, a photon can convert into an electron-positron pair when inside the coloumb field of a nucleus. From four-momentum conservation, one can find that this threshold is given as

$$E_\gamma \geq 2m_e c^2 + 2\frac{m_e^2}{m_{\text{nucleus}}}c^2. \tag{2.30}$$

Since the mass of the nucleus is much higher than the electron mass, this can be simplified as

$$E_\gamma \geq 2m_e c^2. \tag{2.31}$$

For pair production in the field of an electron instead of a nucleus, this formula simplifies to

$$E_\gamma \geq 4m_e c^2. \tag{2.32}$$

Depending on the screening of the nucleus by the atomic shell, the cross-section[19] for this process will differ, taking the form

$$\sigma_{\text{pair}} = 4\alpha r_e^2 Z^2 \left(\frac{7}{9}\ln 2\varepsilon - \frac{109}{54}\right), \tag{2.33}$$

$$\text{with } 1 \ll \varepsilon < \frac{1}{\alpha Z^{1/3}}. \tag{2.34}$$

If ε becomes larger, the equation becomes

$$\sigma_{\text{pair}} = 4\alpha r_e^2 Z^2 \left(\frac{7}{9}\ln\frac{183}{Z^{1/3}} - \frac{1}{54}\right). \tag{2.35}$$

The photons from the ^{55}Fe source usually used in the calibration of gaseous detectors have an energy of 5.9 keV. Due to the large energy required for pair production, these photons are not able to produce electron-positron pairs inside the detector. As such, the measurements in chapter 4 will not contain any photons that underwent this process.

2.1.2. Recombination, Drift and Attachment

Inside a gas, atoms and molecules collide with each other. When a particle like an electron or a muon is inside this gas, it also collides with the atoms or molecules in that gas. For particles lacking a substructure causing any inner degrees of freedom,

the energy distribution is given by the Maxwell-Boltzman equation

$$F(\epsilon) = c \cdot \sqrt{\epsilon}\ e^{-\epsilon/kT}, \tag{2.36}$$

with k being the Boltzmann constant, T the temperature in Kelvin, c a constant and ϵ given as

$$\epsilon = \frac{3}{2}kT. \tag{2.37}$$

This distribution is valid for so called *thermal* particles. From a simple calculation, one can define the average length of the path between two collisions, the *mean free path*

$$\lambda = \frac{1}{N\sigma(\epsilon)}, \tag{2.38}$$

where N is the number density of gas particles and $\sigma(\epsilon)$ is the energy dependent collision cross section. While these ideas have been developed with thermal particles in mind, they still stay valid for charged particles in a (small) constant electric field. The drift velocity of a particle is then given as

$$\vec{v}_{\text{drift}} = \mu(E) \cdot \vec{E} \cdot \frac{p_0}{p} \tag{2.39}$$

with E being the electric field and p/p_o being the pressure normalized to unit pressure. $\mu(E)$ is the *charge-carrier mobility*, a material constant that depends on gas and particle. This equation holds for ions. Electrons are far more mobile than ions and therefore the mobility of electrons depends much more on the strength of the electric field. Townsend [27] found an equation for the drift velocity of the electron:

$$\vec{v}_{\text{drift}} = \frac{e}{m}\tau(\vec{E}, \epsilon)\vec{E} \tag{2.40}$$

where τ is the time between two collisions, which itself depends both on the energy of the electron and the electric field strength, which are themselves correlated. The drift properties of electrons highly depend on the gas mixture [28]. If even small concentrations of other gases are present, drift properties can change dramatically [29]. The main influence of the drift on the signal is coming from a widening of the peak due to the stochastic effect of the collisions. The longitudinal diffusion is given as:

$$\sigma_x = \sqrt{2Dt}, \tag{2.41}$$

where D is the diffusion coefficient of the gas and t is the drift time. For a detector, two more effects can cause issues. If the field inside the detector is too low, the created electron will just recombine with the ion it came from before they separate. In this case, the electron is completely lost.

The other effect comes from electronegative atoms or molecules, like O_2 in the gas. An electron can attach itself to one of these atoms or molecules when it collides with it. If this happens, the electron is lost and the signal will be attenuated accordingly. This attachment can be described using an energy dependent cross-section $\sigma(\epsilon)$. In a gas mixture, the attachment cross-section can be calculated by using a simple weighted average of gas types g with corresponding concentration c_g and cross-section σ_g:

$$\sigma_{\text{mix}}(\epsilon) = \sum_g c_g \sigma_g(\epsilon) \tag{2.42}$$

This equation holds as long as all concentrations sum up to $\sum_g c_g = 1$.

2.1.3. Gas Amplification

If the electric field is high enough to accelerate the electron to a kinetic energy above the ionisation threshold for the gas inbetween collisions, the electron can knock another electron out of the shell of an atom, as discussed in section 2.1.1. This creates two free electrons which then drift further in this strong field. These electrons can then again knock out electrons, repeating over and over, creating a chain reaction called an *avalanche*. The distribution of the number of electron reaching the anode can be described by the Polya distribution [30]:

$$P(N_e) = \frac{1}{\overline{N_e}} \frac{(1+\theta)^{1+\theta}}{\Gamma(1+\theta)} \left(\frac{N_e}{\overline{N_e}} \right)^{\theta} \exp\left(-1(1+\theta) \frac{N_e}{\overline{N_e}} \right) \tag{2.43}$$

An example of the distribution can be seen in figure 2.5. While the distribution was not originally conceived for this purpose and its applicabillity was uncertain for 40 years, in the early 2010s, the distributions of avalanche electrons have been shown to follow Polya statistics by H.Schindler[31, 32].

2.1.4. Example: The Geiger-Müller Counter

Even though the Geiger-Müller counter exists for more than 100 years already, it is still a very commonly used technology. The basic setup is simple and can be seen in figure 2.6.

A wire is placed in the center of a cylindrical tube that confines a gas volume. Between the inner wall of the tube and the wire, an electric field accelerating electrons toward the center wire is applied. If an ionizing particle enters the volume, it will deposit energy in the form of electron-ion pairs along its path (see section 2.1.1). The electric field will then separate the electron and the ion and cause them to move towards the wire and the wall, respectively (see section 2.1.2). Due to the geometry of the detector, the closer the electron comes to the wire, the

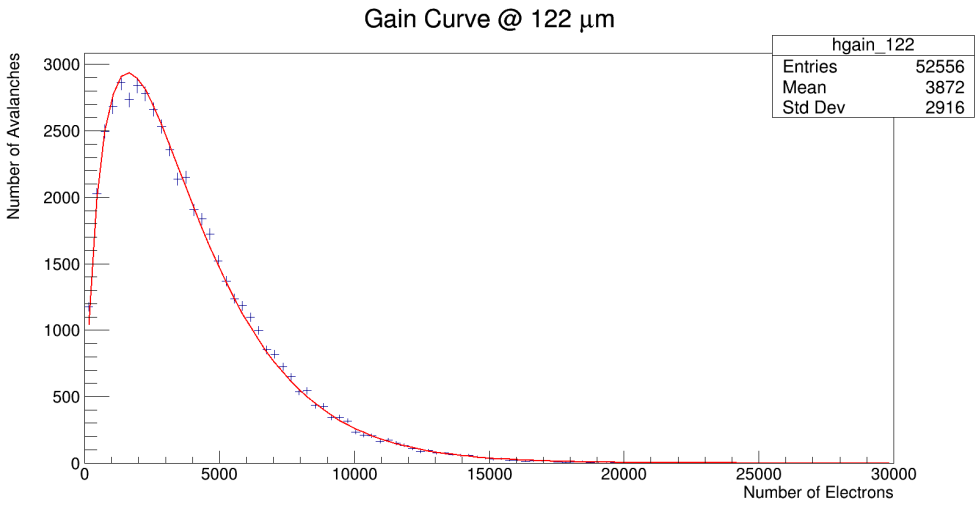

Figure 2.5.: Example of a Polya function fitted to simulation results for avalanche formation in a NSW Micromegas

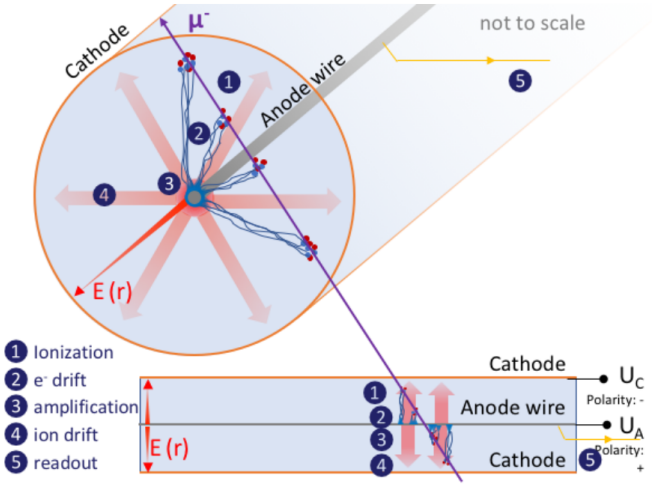

Figure 2.6.: Schematic view of a Geiger-Müller counter, from [33]

higher the electric field will become and the more energy the electron can acquire between collisions, until it becomes energetic enough to overcome the ionization energy threshold of the gas and start the amplification (see section 2.1.3). While the electrons are immediately getting neutralized by the wire, the ions have to drift from the amplification region all the way to the wall, contributing to the signal on the wire by induction. Several different effects also play a roll in several different applications of the gas amplification method and will be explained using the Geiger-Müller tube as example in the following paragraphs.

Penning Transfer Inside a gas, atoms and molecules collide constantly. Often, these atoms are considered to have no substructure. While this is true for kinetic energies inside the gases, if excited atoms or ions are involved, other transfer effects can happen. If one of the colliding atoms is excited, it can transfer the excitation energy to its collision partner, thereby exciting or, if the ionization energy of the partner is smaller than the excitation energy, even ionizing it. This transfer of excitation was first described by *F.M. Penning*, who gave the *Penning Effect* its name[34]. The ionization cross-section in this process is influenced by the number of accessible energy levels in the partner atom and the individual cross-section of the energy level. Until very recently, the penning transfer probability has not been theoretically calculated, as it includes many unknowns and has to be redone for each gas mixture[35]. As such, simulations, including the ones presented in this work, have to rely on experimental data to determine the correct factors to use. This has been done for many different gas mixtures, including argon - carbon dioxide[36]. A plot showing the penning transfer coefficients for argon and carbon dioxide mixtures can be seen in figure 2.7. To obtain the correct values to use in the microscopic simulation, simulations with different factors are performed and compared to measurements. Only very few ternary and no quarternary gas mixtures have been measured so far, none containing oxygen or water. For that reason, the simulations with oxygen and water shown later in this work do not contain penning transfer simulation and have to be scaled to the measured values. Since the simulation only causes a direct scaling of the results, the relative differences between measurements should nevertheless also be seen in simulation.

Secondary Avalanches and Quenching The ionization cross-section for argon is higher for electrons in lower shells than the outer. This means that usually an argon ion will be excited after it has been ionized either by the original ionizing radiation or the electrons in the avalanche. Once the argon deexcites, it will emit a photon. Due to the energy levels in the argon ion, the photon will have more energy than the first ionization energy of argon, allowing it to generate another electron-ion-pair. Since the photon is neither charged nor has a high cross-section

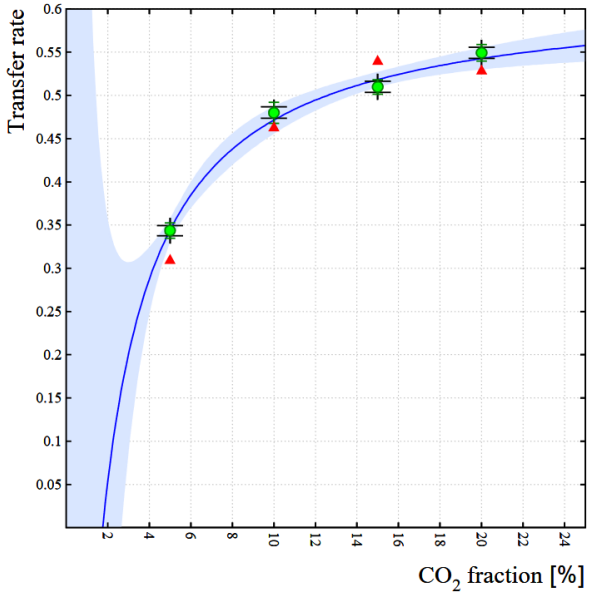

Figure 2.7.: Measurement of the Penning Transfer Coefficient for argon and carbon dioxide mixtures, from [36]

for interaction with gas, this secondary pair can be created in a different area of the detector, even closer to the cathode than the original point of interaction, thereby creating another cluster. This cluster will then extend the signal time due to the delay in creation and differences in drift time, as well as the spatial extend of the signal in the detector due to the position difference. In cases of high fields, the signal might be extended far enough to create even more photons, generating more pairs generating more photons, causing a chain reaction that leads to a discharge in the detector. To reduce the probabilty of this photon emission, the argon ion needs to be presented with other possibilities of deexcitation. This can be done by adding another gas, preferably one with more degrees of freedom, like carbon dioxide, methanol or ethanol, to the detector gas. If the excited ion collides with one of these molecules, it can transfer its excitation. The additional degrees of freedoms increase the cross-section for this transfer and create avenues of deexcitation for the molecular ions that result in photons that are not energetic enough to cause more ions in other parts of the detector. Since these gases reduce discharges in the detector, they are also called *quenching gases*.

Gain Regions The electric field in the detector determines the signal strength, or the amplification gain. Depending on the gain, the detector works quite differently. The following gain regions can be distinguished (please note: the given numbers are valid for Geiger-Müller tubes and can differ for other gaseous detectors):

- Recombination Region ($G < 1$): If the electric field is too low to reliably separate electrons and ions, only a fraction of electrons actually reach the wire.

- Ionization Chamber ($G = 1$): Once the field is large enough to separate the electron-ion pairs but does not provide for an amplification region, the signal consists of only the primary charges.

- Proportional Region ($G \approx 10^3 - 10^5$): Once a region with a field exceeding the amplification threshold exists, electrons can start an avalanche that grows exponentially with a stable gain and statistical fluctuation. Since the charge remains proportional to the initial number of primary electrons, it is therefore also proportional to the energy deposited in the detector by the particle. Proportional counters are operating in this voltage.

- Limited Proportionality Region ($G \approx 10^5 - 10^8$): At a certain point of amplification, the amount of ions from the avalanche becomes so large that the electric field gets changed by the space charges close to the wire. The integrated signal therefore is no longer fully proportional to the amount of primary electrons created by the particle. Resistive plate chambers and similar detectors operate in this region

- Saturation or Geiger Mode ($G \approx 10^8 - 10^9$): If the field strength becomes even larger, at some point the space charges created by the avalanche will be so high that the field will be distorted strong enough to stop the amplification at a certain amount of electrons, so called *self-quenching*. At this point, the signal strength is limited in size and saturates. Since the field between the generated electron-ion pairs in the amplification regions starts breaking down at this point, the pairs can recombine. This recombination generates photons that can freely travel the detector, and can generate new primary electron-ion pairs in any region of the detector, causing secondary avalanches in the detector. At some point, the generated anode current will cause the voltage in the detector to break down, stopping any further amplification until the voltage can be built up again. As the name suggests, the Geiger-Müller counter operates in this voltage region.

- Discharge Region ($G > 10^9$): If the secondary avalanches in the detector are not contained, the avalanche can grow into a streamer. This streamer can create a plasma conduit between wire and wall, causing a discharge. If this discharge is not limited by electronics, the heat generated can cause severe damage to the detector, up to the point of destruction. The limit at which discharge occurs is also called the Raether-Limit[37].

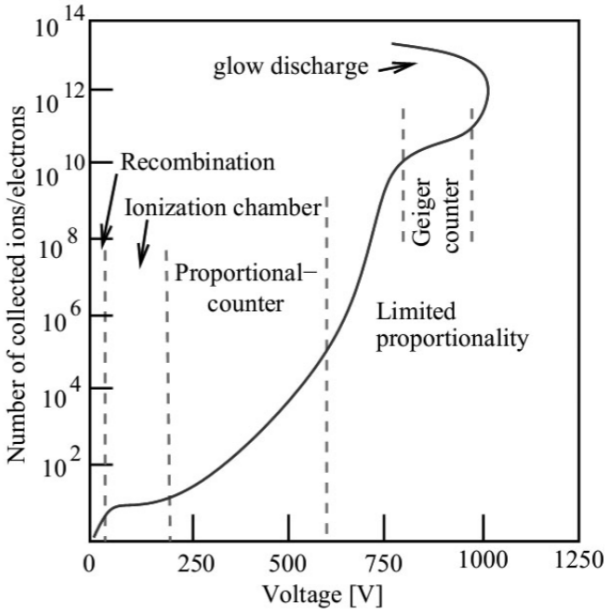

Figure 2.8.: Characteristic graph of a gaseous detector, from [4]

To find the right voltage for the gain region one wants the detector to operate in, a characteristic graph of the detector can be taken. An example of this graph can be seen in figure 2.8.

Variations of the Geiger-Müller Counter The variations of the Geiger-Müller tube are mainly differentiated by the gain region they are operated in. The Geiger-Müller counter itself is operated in the saturation region. As such, it can only count particles interacting with the volume. During the 1920s to the 1940s, the proportional counter was developed, which is capable of measuring the charge during the primary ionization[38–40]. Operated in the proportional region, it allows the user to extract the energy deposited in the detector by the particle.

If the drift time is known and the time resolution of the detectors is good enough to resolve different clusters, the track of the particle going through the detector can be reconstructed. Used in this mode, Monitored Drift Tubes (MDT) are stacked and used in the ATLAS muon system to track particles through the detector. In addition, tubes can be used for particle identification if the energy loss of the particles is known. This is done in the ATLAS inner detector, using Transition Radiation Trackers.

If the proportionality and identification are not required, but lower dead time is required, streamer tube detectors can be used. These were developed in the 1970s to 1980s [41, 42]. These utilize a resistive coating on the wire to limit

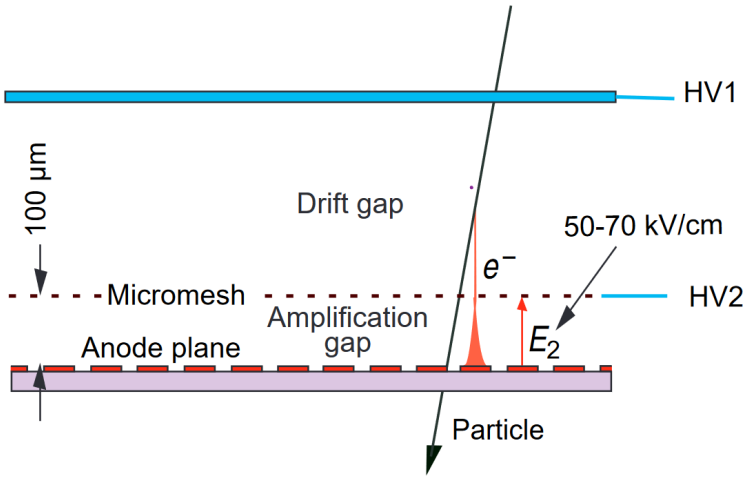

Figure 2.9.: Schematic of a Micromegas detector. A particle ionizes the gas, the resulting electron drifts towards and through the mesh, where it then gets amplified, from [13]

the discharge current in the high gain region they are operated in, allowing it to self-quench developing streamers.

Due to their simple structure, many high energy physics experiments still use these kind of detectors. However, the low rate-capability due to the dead time induced by the large voltage drop especially in high gain operation modes and the ion drift in the proprotionality region are some of the largest drawbacks of these detector types. To reduce the ion drift time, a new type of MDT is being deployed in the ATLAS-detector. These sMDT have a smaller diameter of 1.5 cm, reducing the ion flight time[43].

2.2. Micropattern Gaseous Detectors

Micropattern gaseous detectors are using the same basic principles as they are used in the Geiger-Müller counter, but allow for spatial readouts and faster response time. The field is under active developement with many new architectures emerging in the last few years. The two technologies discussed here, Micromegas and GEM detectors, are currently being implemented in large scale experiments at the LHC, with GEMs being used in CMS and Micromegas being used in ATLAS.

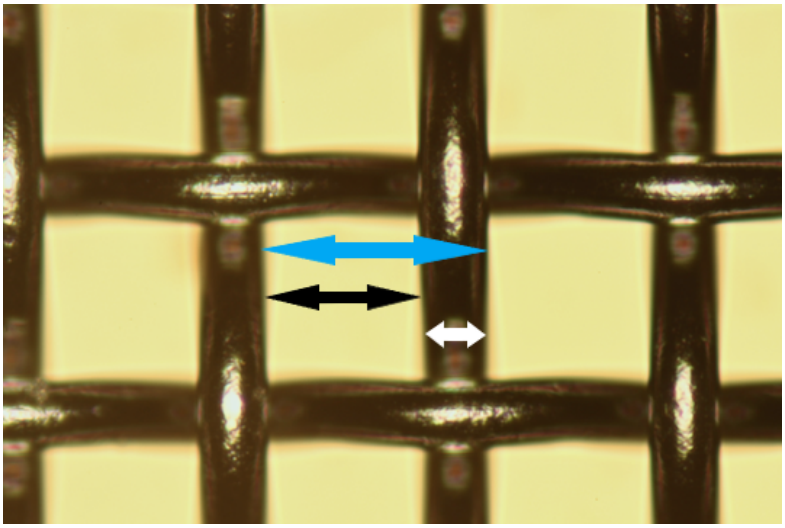

Figure 2.10.: Closeup photograph of a typical mesh. Marked are the hole width in black, the wire diameter in white and the pitch in blue.

2.2.1. Micromegas

The Micromegas detector was first designed in 1996 in Saclay[44]. The part the name of the Micromegas detector is derived of, is the micromesh that separates the detectors volume into a drift and an amplification region. As opposed to the Geiger-Müller counter, both fields are close to homogeneous, with the exception of the area around the mesh. In addition, most ions are generated in the high-field region of the detector. In a Geiger-Müller counter, these ions need to drift all the way to the outside pipe to get neuralised, while in a Micromegas the ions only have to drift to the mesh. This leads to a faster regeneration of the field inside the detector and thus to a lower dead time. A cross section of the Micromegas detector can be seen in figure 2.9.

Micromesh The Micromesh is a steel fabric woven like cloth on a loom. It is commercially available and can be classified by the steel wire diameter and the pitch of the woven structure, the space from one side of the wire to the same side of the next. A picture of a mesh in which these quantities are indicated can be seen in figure 2.10. Meshes are usually characterized by hole size-wire diameter, e.g. a 45-18 mesh has a pitch of 63 µm and a wire radius of 9 µm. As it is made out of steel, it can conduct electric charge and can therefore be used to create something similar to a parallel-plate capacitor, while at the same time being able to allow electrons to pass through the holes in the structure.

Transparency The electron transparency of the mesh is a measure of how well electrons can travel through the mesh, i.e. the ratio of electrons that are able to pass through the mesh. In a first naive description, asuming no electric field, the so called *optical tranparency* can be defined as

$$T_{\text{opt}} = \frac{A_{\text{open}}}{A_{\text{tot}}}, \tag{2.44}$$

were A_{open} denotes the open area of the structure, i.e. the holes, and A_{tot} is the total area of the mesh. This is true for electrons that travel in a straight line perpendicular to the mesh. However, if electric fields are involved and diffusion and electron scattering are negligible, slow electrons will travel along field lines. As such, the transparency in a Micromegas can be approximated in a field calculation as

$$T = \frac{N_{\text{pass}}}{N_{\text{tot}}}, \tag{2.45}$$

where N_{pass} is the number of field lines passing through the hole and N_{tot} is the total number of calculated field lines. While there has been no analytic description for a micromesh so far, for a grid of parallel wires, this problem can be solved analytically [45]:

$$\begin{aligned} T(E_D, E_A, \rho) = 1 - &\frac{1}{\pi E_D}\left(E_D + E_A\right)\sqrt{\rho^2 - \left(\frac{E_A - E_D}{E_A + E_D}\right)^2} \\ &- \frac{E_A - E_D}{\pi E_D}\cos\left(\frac{E_A - E_D}{E_A + E_D}\frac{1}{\rho}\right) \end{aligned} \tag{2.46}$$

In this equation, E_D is the drift field, E_A is the amplification field and $\rho = {}^{2\pi r}/_{p}$, with r being the wire radius and p being the pitch. This equation holds for the range of

$$\frac{1-\rho}{1+\rho} < \frac{E_A}{E_D} < \frac{1+\rho}{1-\rho}. \tag{2.47}$$

If the assumptions regarding diffusion and scattering do not hold, the true transparency will be lower than the calculated one, but at the same time the lines will still be focused into the holes, leading to a higher than optical transparency.

Anode Structure As the amplification gap is only around 100 µm, the tolerances with repect to the gap size has to be very low, on the order of µm. In such an environment local defects, like mesh wire damages or gap size varations, can change the gain in a small region to a point, where discharges develop. The discharges, also called *sparks* can drain the voltage between the electrode, causing a dead time

until the fields can be build back up. Even if the tolerances are low enough, local variations in gas mixture or even in avalanche formation can lead to gains in excess of the Raether limit[37, 46, 47], creating a streamer and causing a discharge. Since these unavoidable sparks can cause substantial damage to the detector and the detectors in experiments like the ATLAS detector need to perform for at least 20 years, a solution to mitigate these discharges has to be found.

The readout strips are meant to be of low resistivity to allow for a fast signal readout. To protect the anode from discharge creation, a protective layer of a highly resistive material can be used as anode on top of the readout strips[48]. Doing this, the voltage on the resisitve layer will drop locally before the avalanche gets large enough to develop into a discharge. This *resistive layer* can have different shapes, e.g. one continuous layer or in strips either parallel or perpendicular to the readout strips. If a striped resistive layer is chosen, special care has to be taken to get a homogenous voltage over the entire surface. Especially in large detectors, long strips can lead to a voltage drop the further away from the high voltage supply the point on the surface is, since the local charge needs too long to dissipate. To mitigate this effect, the strips can be interconnected at several points. For example in the NSW Micromegas, the strips are connected alternating between their neighbors every 10 mm. This also mitigates effects from disrupted or damaged strips.

This resistive layer causes the signal to no longer being directly deposited on the read out strip. The resistive strips couple capacitively with the copper strips below them, inducing a signal which can then be read out. In a setup in which resistive and copper strips run parallel, the coupling of the resistive strips is mainly focused around the strip directly below it, but some cross-talk cannot be avoided. If the strips are misaligned, the amount of copper strips on which a signal is induced increases, with the maximum reached at orthogonal strips. This decreases the spatial resolution of the detector, making a precise application of these resistive strips vital in the production of readout boards, especially in the large detectors for the NSW[33].

2.2.2. GEM

To reduce dead time, the Gas Electron Multiplier (GEM) detector also confines the amplification to a small area of the detector. As opposed to the Micromegas detector, which creates the amplification volume between the mesh and the anode, the amplification volume is confined by two electrodes that are placed on a thin foil made from an insulator material, usually Kapton. This copper-insulator-copper sandwich is then chemically perforated to produce holes with diameters around 25 µm to 125 µm and distance of around 50 µm to 200 µm. Each hole can then act as its own proportional counter if a potential difference is applied between the

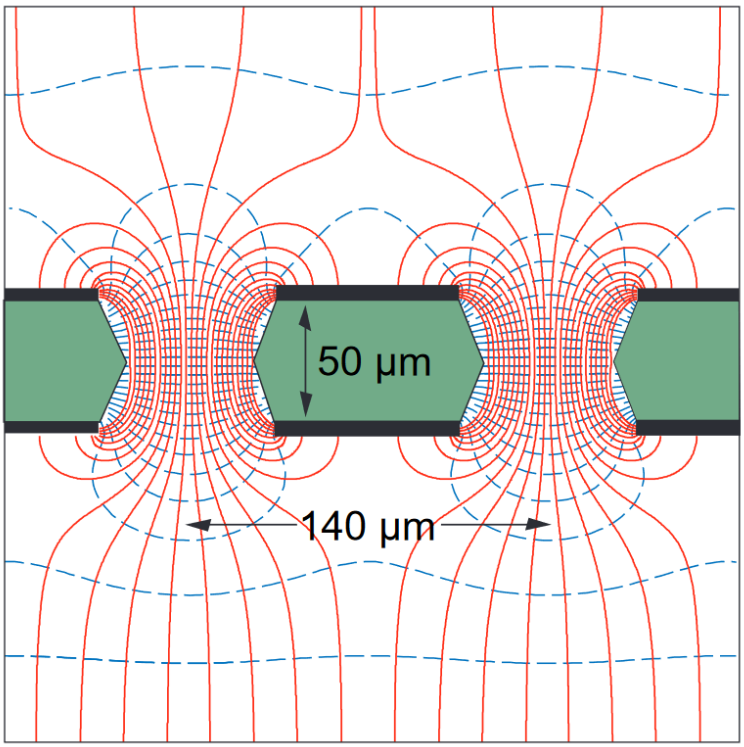

Figure 2.11.: Schematic of a GEM detector. A particle ionizes the gas, the resulting electron drifts towards and into one of the holes, where it then gets amplified. After this, the cloud drifts further, from [13]

two copper layers. Primary electrons generated above the foil drift into the holes, create an avalanche inside the hole, in which a field of around 50-70 kV/cm is created by the electrodes, and the resulting cloud then mostly drifts out into the region below. Due to the shape of the field, ions will not all be collected on the upper foil. This can generate space charges in the drift volume that can reduce the drift field and can increase the drift time.

If the gain in this foil is already enough for the considered application, these clouds of electrons can now drift towards the readout board. If more gain is needed, more foils can be stacked, allowing for higher gains than usual[49, 50]. For example, to obtain gains in the order of $G \approx 1 - 2 \times 10^4$, three GEM foils are stacked in the CMS GEM detectors[51]. A schematic view of the GEM structure can be seen in figure 2.11.

2.3. Effect of Contaminations on MPGDs

Contaminations can influence all the processes in the detector. Some contaminations can act as quenchers, some can influence the drift properties of the mixture, some can cause attachement and some can influence the avalanche creation process. Of special interest in the construction of detectors are the most likely gas contaminations that could enter the detector. Especially the highly electro-negative oxygen and the water vapour entering the detector from the outside environment gas can cause changes in its behaviour.

2.3.1. Contamination with Oxygen

With a concentration of around 21%, oxygen is the second most abundant gas inside the atmosphere after nitrogen[52], while it is the second most electro-negative element, after fluorine[53]. Thus, it is very likely to enter the detector and also very likely to change the drift properties of the detector with a very low content. In particular, the high electro-negativity of the oxygen can cause slow electrons in the drift region to attach to the oxygen when colliding with it. The energy-dependent cross-section for electron attachment to oxygen can be seen in figure 2.12. The Magboltz data seen in this graph is used by Garfield++ to simulate events and is compared in the plot to experimental results obtained by different groups and collected by the open-access database lxcat.net[54]. Simulations of the effect using Garfield++ can be seen in section 4.3.

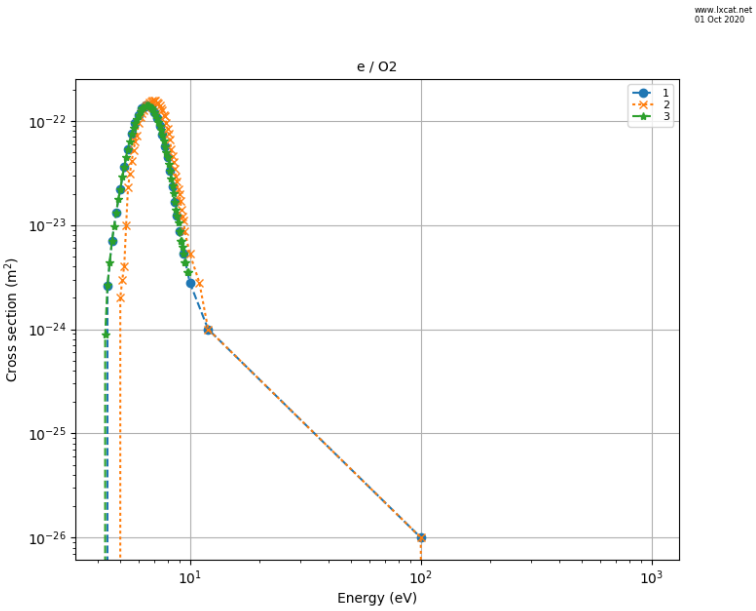

Figure 2.12.: Attachment cross sections of electrons in O_2. 1. is a calculation from Magboltz by S.F. Biagi, 2. is from the IST-Lisbon database, 3. is from the Itikawa database. Retrieved 1st October 2020, from lxcat.net[54]

2.3.2. Contamination with Water

In Micromegas, the effect of water in the detector has not been studied in great detail. While the breakdown voltage of pure water vapor has been measured 1000 V at 10 Torr cm (the typical value for the Micromegas gas gap) in dedicated experiments[55], the influence on the stability of the detector has only been studied very recently[56]. As water is molecular, it may act as a quenching gas inside the detector, similar to carbon dioxide. Due to its polarity, it might however also increase the effect of sparks once they are created. Also, water can be absorped by material inside the detector, causing those materials to change their properties slightly. While the last two changes cannot be easily investigated with the tools available, the first one can be simulated using Garfield++. The simulations performed can be found in section 4.3.

Part II.

Studies on the Effect of Contaminations of the Detector Gas in Micromegas Detectors

3. The Würzburg Gaseous Detector Research Facility

The Würzburg ATLAS group moved into its new building in 2011. The cosmic ray stand was created in these new facilities to allow for measurements with SM2 modules of the ATLAS NSW. This chapter is dedicated to this measurement room and will describe the additions that have been made to it during this work, including new readout setups, a new gas system and more options for high voltage supply.

3.1. The Cosmic Ray Stand

The lab was set up by Stefan Weber in the early 2010s in the then new rooms of the group. A detailed description of the process can be found in [57]. The stand itself was built to be able to house a NSW SM2 module. The rack is placed on a reinforced part of the room and made of an aluminium frame, in which four shelves can be placed in adjustable heights. The shelves have a usable area of 210 cm by 150 cm, while the entire rack has a height of 225 cm. Above the lowest shelf-point, an 8 cm thick absorber made of steel is placed with its upper edge being around 60 cm above ground. Mounted above the structure is a monitored drift tube similar to the ones used in the atlas detector. It can be used to cross check binary gas mixtures on the content. To ensure as little contamination as possible for the studies presented in this work, it has been shorted using a piece of steel pipe, as the system would otherwise contain plastic piping, which would add unwanted contaminations to the detector gas. A picture of the cosmic ray stand can be seen in figure 3.1.

3.2. Electronics

To be as flexible as possible and allow the use of as many detectors as possible, several different systems for readout have been set up in the lab. The power to the detectors is supplied using a CAEN high-voltage supply system, which will be described next, including changes made during the upgrade. The different

Figure 3.1.: Photograph of the cosmic ray facility. The frame with the scintillators and the pressure chamber can be seen in the center. Behind it is the orange electronics rack. On the left side are the mixing panel and the contamination measurement devices.

readouts, with the exception of the NIM+TDC readout, have been added during the upgrade to allow for more choice when using gaseous detectors. They will be described later in this section.

3.2.1. Power Supply System

The power supply system consists of a mainframe into which different high voltage supply cards can be plugged, depending on usecase. All of the cards used are providing voltage through Safe High Voltage (SHV) connectors. Before the upgrade, these cards were mainly used for scintillators, but these cards did not have a sufficient current resolution for the Micromegas detectors. Therefore, an additional card had to be purchased and installed during the upgrade. The mainframe is a CAEN SY2527[58]. The system provides a common floating ground, which means that the ground can float away from the ground provided to the power supply externally by up to 5 V. It contained cards of two different types. The two boards of type A1535SN (24 channels) and A1535DN (12 channels) are only capable of providing voltage of one polarity, switchable by using a jumper contact, while the A1535SM can provide both polarities (12 channels each) at the same time[59]. The current resolution of 0.5 µA for these boards would mean that a normal Micromegas detector would already be broken if any current would be measured. The newly added board of type A7236DN[60] has a much better resolution of 5 nA, allowing the safe use of Micromegas detectors. It only provides voltage of positive polarity compared to the common ground, and as such, the Anode is always grounded for the Micromegas detectors used in the lab.

3.2.2. Readout Systems

Every detector setup used in the measurement room has its own dedicated readout system. This chapter explains the principle of all used systems, starting with the scintillator triggers, going to the resistive Micromegas and finishing with the bulk Micromegas readout. All detector technologies are described in section 3.4.

NIM Electronics and TDC

The Nuclear Instrumentation Module (NIM) standard was first defined by the U.S. Atomic Energy Commission in its report TID-20893 in 1964[61] and was revised several times until 1969 and then updated in DOE/ER-0457T[62]. It sets out a standard for nuclear instruments, including the shape of the unit, its power supply connections and usage. The units are placed into NIM-racks, which allow for compact setups of electronic instruments in laboratories. In addition to the units, the NIM-standard also defines a standard for logic pulses exchanged between units.

The NIM crate in the lab contains two constant fraction discriminators of type N843 by CAEN[63], which create NIM-pulses from the analog signals given by the detectors, and two logic units of type 757 by Phillips Scientific[64] that serve to link signals in different detectors towards each other logically. This allows the definition of trigger signals requiring that particles are detected in several detectors in coincidence or allow detectors to veto signals seen in other detectors. The NIM-pulses are also accepted by the Time to Digital converter (TDC) of type MTDC-32 by mesytec[65], which can record the time differences between a given trigger signal and other signals. The TDC saves several time steps of data, so that the time window that is read out can also take pulses into account that reached the TDC before the trigger signal. The data is then encoded digitally and send to a readout computer. The data contains each pulse in the time window and the time each pulse arrived at the detector. A piece of software is used to encode these data packages into csv files, which allows for analysis using tools like ROOT.

The Scalable Readout System

As can be seen from the name, the Scalable Readout System (SRS)[66] was designed to be a scalable readout system for MPGD that can be used in small labs, but also scaled up considerably. It consists of a variable number of Front-End Concentrator (FEC), in a SRS service crate, which transmit the data digitally to a computer using ethernet connections and the UDP-protocoll. The crate also contains central services concentrated in the Scalable Readout Unit (SRU), like clock functionality. In the lab, the SRS is combined with APV25 ASIC hybrid boards[67], which are connected to one FEC via HDMI-cables. The HDMI-cables are used not according to the HDMI-specification, but the structure of the cable is well suited to transport the analog signals generated by the APV25(while the APV25digitizes the signal for each channel, the digital values are then again transmitted in an analogue fashion). Two APV25 boards can share one HDMI connection in a master/slave setup, with both signals send distinctly on different lines of the HDMI-cable. In addition, 8 HDMI-cables can be connected to a FEC, allowing the parallel read out of up to 2048 channels per FEC. The SRS readout scheme can be seen in figure 3.2.

Each APV25 has 128 channels, which are digitized independently using a 25 ns charge to voltage converter. To allow for a delayed trigger signal, the values are then saved in a ring buffer with a capacity for 160 entries, i.e. a buffer that always overwrites the oldest value in favor of the new one. Once the chip recieves a readout command, which via the FEC can either come from an external trigger or from the Scalable Readout Unit clock, it will send the contents of the ring buffer to the FEC in the SRS-crate. The time window around the trigger signal time can be defined in the SRS configurations.

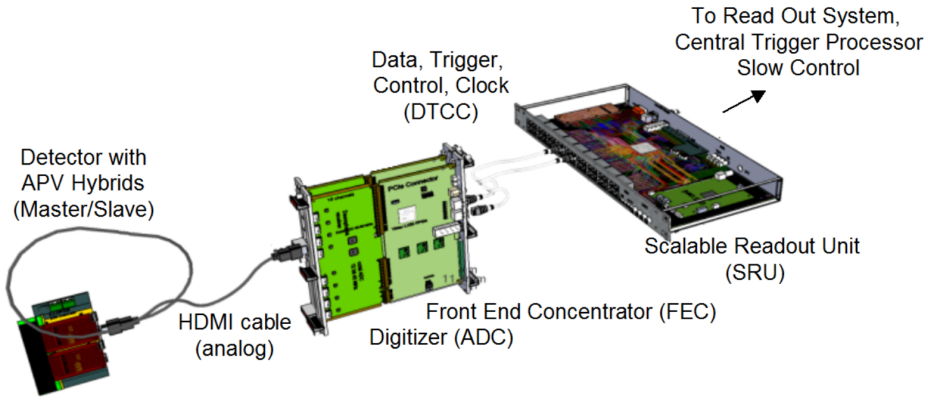

Figure 3.2.: Schematic of the SRS readout system, from [68]

The signal is built around a clock cycle in a phase locked loop approach. In one cycle of the clock, one time bin of the digitizers for each strip is transmitted using analog step functions whose height is proportional to the digitizer value. Since this signal is again analog, the FEC needs to digitize the signal once more. Depending on the length of the cables used, the output of the APV25 and the digitizer of the FEC are shifted and pick up a phase, making the digitizer pick up parts of the signal for two different strips. In the worst scenario, this could mean that the signal of two transmitted strips are averaged. This phase, called *pll-phase*, can be adjusted for in the SRS config. To mitigate the effect of the phase, the digitizer values for each strip are not transmitted one after the other, but are actually transmitted in the order 0, 32, 64, 96, 128, 1, 33, etc. If the APV25 and the FEC are out of phase, this will reduce the peak height at the true position and will cause a shadow peak +32 strips away from the true peak. This means that by taking test data, one can adjust the phase by minimizing this shadow peak.

To reduce the strain on the ethernet connection, the FEC and SRS allow for noise supression. First, around 1000 frames of data are taken without any source. These are averaged, assuming a normal distribution of the noise, creating a *pedestal*, or a 0 value for each channel. From the σ of the pedestal, one can estimate the height a signal needs to be so that it is not deemed noise. For example, if the threshold is 5σ, any channel that is below this threshold will be discarded as noise, leaving only channels which show at least a value of pedestal+5σ. This considerably reduces the size of an event frame, avoiding package losses in the send and forget UDP transmission that was chosen. The readout computer is running the mmDAQ program, which provides both online analysis tools and saves the events in a .root file, allowing for more in-depth evaluation of the data using scripts.

In addition to the features used in the lab, the SRU provides all features that are necessary if used in larger experiments, like the Slow Control Adapter (SCA), which can be used to receive configurations and to send system info to the central system, or ultra fast connections to the readout systems or the central trigger processor.

Multi Channel Analyser Setup

The multi channel analyser setup is used to read out the ion signal on the mesh of a Micromegas detector. The system can be used with the mesh signal of both bulk and resistive Micromegas. Used in the lab is the CAEN A422A preamplifier[69], which is connected to the high voltage power supply for the mesh and feeds it through to the detector. The rise time of the preamplifier is 50ns. Once charge is collected on the mesh, the preamplifier converts the drop in voltage between mesh and anode and generates an inverted unipolar signal. This signal is then sent to the sprectroscopic amplifier N968[70], which conforms to the NIM electronics standard and is therefore placed into the crate with the other NIM electronics modules. It both amplifies and shapes the signal with variable amplification factors and time constants for shaping with a gauss function. The amplified signal is then send to the MCA800D Multi Channel Analyzer[71], which is connected to a Windows computer running the software provided by Amptek, the manufacturer. The spectrum can be exported as comma separated file which can be used to perform further analysis using ROOT. Most of the data presented in chapter 4 was taken using this method.

3.3. The Gas System

The first iteration of the gas system was built in 2014. It allowed mixing of Argon and a quencher gas that could be chosen freely in any concentration desired. With the upgraded performed as part of the work presented here, an option for another gas was added to the system and a bubbler was integrated to allow varying the moisture inside the detector gas. The different pressures in the system can be set either compared to the outside pressure (gauge, or g for short), or absolute, i.e. against vacuum (absolute, or a for short). The pressures in this section are labled accordingly.

3.3.1. The Gas System before the Upgrade

The first stage of the gas system was set up in 2014 by Stefan Czerwenka and is described in his master thesis[72]. The system was designed to allow for free

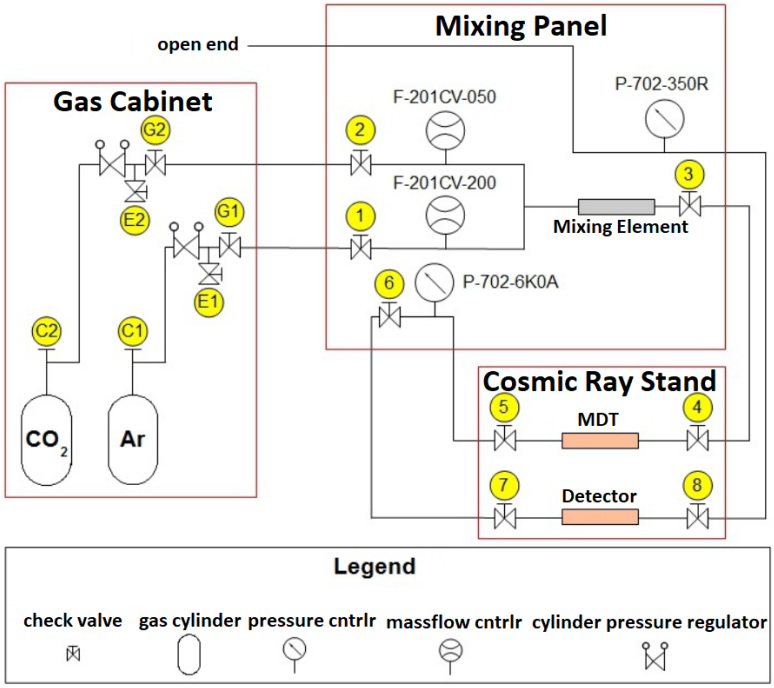

Figure 3.3.: Schematic of the gas system before the upgrade, translated from [72]

choice of one noble and quenching gas each in any ratio desired to be used in the monitored drift tube described in section 3.1 and in any other detectors that are to be investigated. A schematic of the system can be seen in figure 3.3.

From a gas cabinet containing the gas cylinders, the gas flows to the mixing panel at a pressure of around 5 bar(a). Mass flow controllers (MFC) by the company Bronkhorst mix the gases in the ratio desired and a small passive mixing element, a screw-like structure inside the gas pipe, guarantees a homogeneous mixture. From there, the gas flows into the drift tube and back to the panel, where a pressure controller, also provided by Bronkhorst, sets the pressure inside the drift tube at a maximum of 5 bar(a). From there, it flows further into the detectors and back, ending in another pressure controller at a maximum of 100 mbar(g), which vents the gas into the laboratory. The maximum flow is at around 250 ml/min. The flow controller measure the gas flow using the force excerted by the gas on a bent piece of pipe. This force depends on the gas used. As both MFC have been calibrated with argon, the one used for CO_2 has to be recalibrated on the fly. This is done by using a calibration file that has to be loaded before the controlling system is activated.

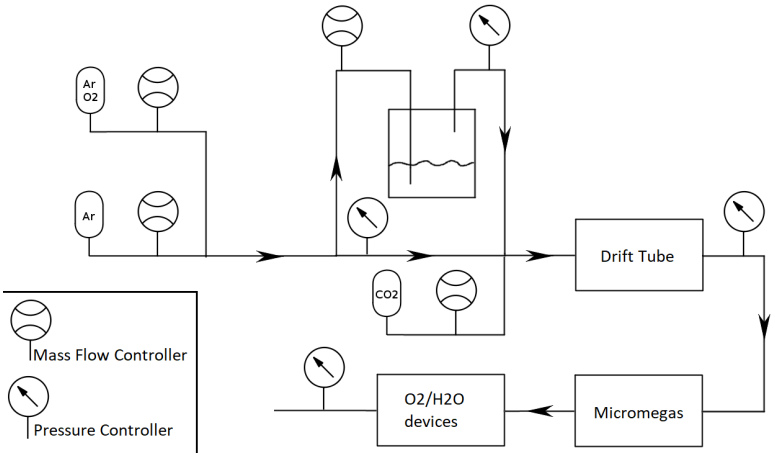

Figure 3.4.: Schematic overview of the gas system after the upgrade

3.3.2. Upgrade of the System

The aim of the upgrade was to be able to vary the contents of oxygen and water in the detector gas between 10 ppm and 1%. Adding oxygen to the detector gas can be achieved by adding another cylinder to the system. A well known method of adding moisture to the detector is using a bubbler to let the gas flow through water, which saturates the water content in the gas. By varying how much of the gas passes through the water, the water content in the gas can be set to the desired value. The setup of the system can be seen in figure 3.4. Adding oxygen was achieved by using a cylinder of argon with 2% added oxygen. This choice was made for safety considerations, considering that pure oxygen is supporting combustion and would therefore have required special care. The argon/oxygen mixture is mixed with the pure argon in the desired ratio. Afterwards, a portion of the gas is send through the bubbler to pick up moisture. After the gas is humidified, the carbon dioxide is added. It is added after the bubbler to avoid the creation of carbonic acid in the water, which would remove the carbon dioxide from the gas and change the ratio of argon and carbon dioxide away from the desired value. After each mixing step, the gas is pressed through a mixing element to ensure homogeneity. After the gas has been mixed to the desired contents, it is led through metal pipes to the MDT. This has been shorted during the experiments, since the MDT itself contains plastic piping. A picture of the mixing panel can be seen in figure 3.5.

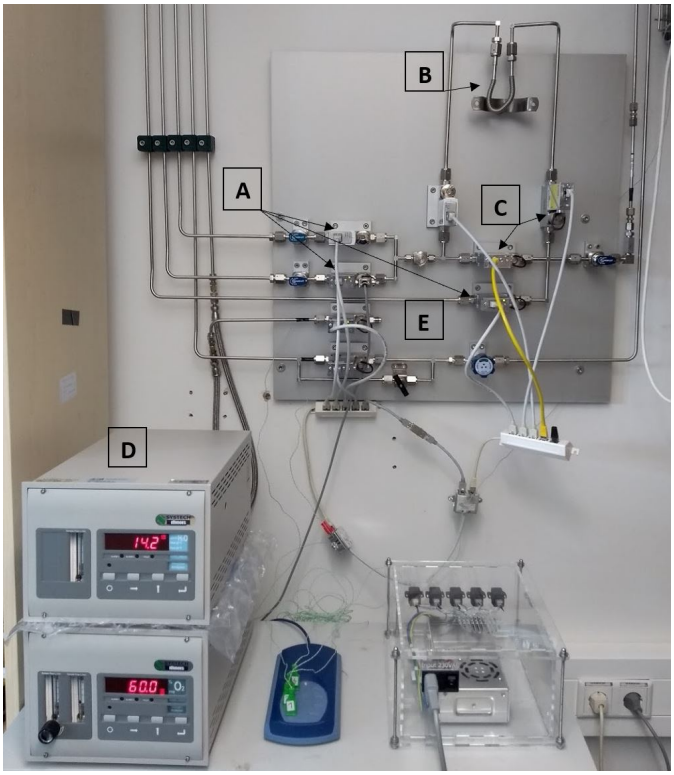

Figure 3.5.: Picture of the mixing panel. A labels the massflow controllers for argon, argon+oxygen and carbon dioxide, B shows the location of the Bubbler, C are the pressure controllers for the bubbler. After the gas passed through the detector, the amount of contaminations is measured in D, before the gas then exits after the pressure controller for the Micromegas at E, from [73]

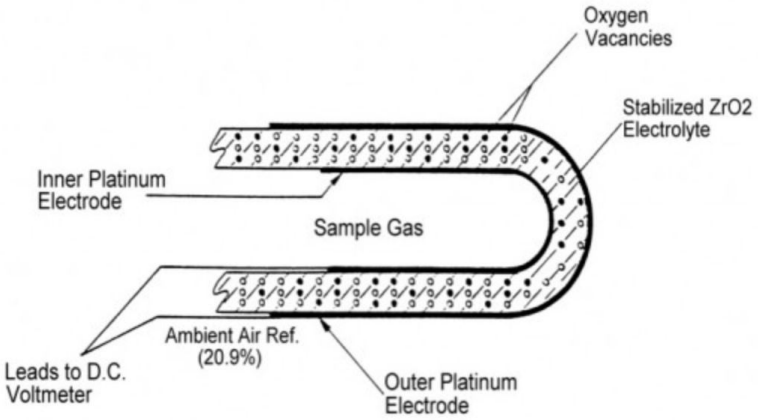

Figure 3.6.: Schematic overview of the probe in the ZR800 (components are labeled), from [74]

Oxygen Content Measurement (ZR800)

The oxygen measurement system used in the lab is the Zirconium Oxygen Analyser ZR800 by Systech Illinois[74]. The probe consists of a zirconium oxide ceramic that surrounds the sample gas and is inside the outside air, as can be seen in figure 3.6. It is placed inside an oven and heated and kept at 670°C, at which point the ceramic structure becomes transmittant to oxygen ions. On every side of the ceramic, platinum electrodes allow the oxygen in the sample gas or the ambient gas to ionise and travel through the ceramic, creating a current. While the exact mechanics of this transport are quite involved, the important feature of the ceramic is the resulting net current, which can be measured. It depends only on ratios of the partial pressures of oxygen on both sides of the ceramic structure. Since the atmospheric air we breath has a very stable oxygen concentration of around 20.9%, the device can calculate the oxygen content of the sample gas using the Nernst formula and output the value in ppm:

$$E(mV) = \frac{RT}{4F} \log \frac{p_{\mathrm{O2,ref}}}{p_{\mathrm{O2,sample}}} \tag{3.1}$$

Where R is the gas constant, T is the absolute temperature of the sensor, F is the Faraday constant and p denoting the partial oxygen pressures in the outside (reference) gas and the sample.

Water Content Measurement (MM400)

The hydrogen measurement is performed using the MM400 humidty analyzer by Systech Illinois. The core of the device consists of a gold coated partially oxidised

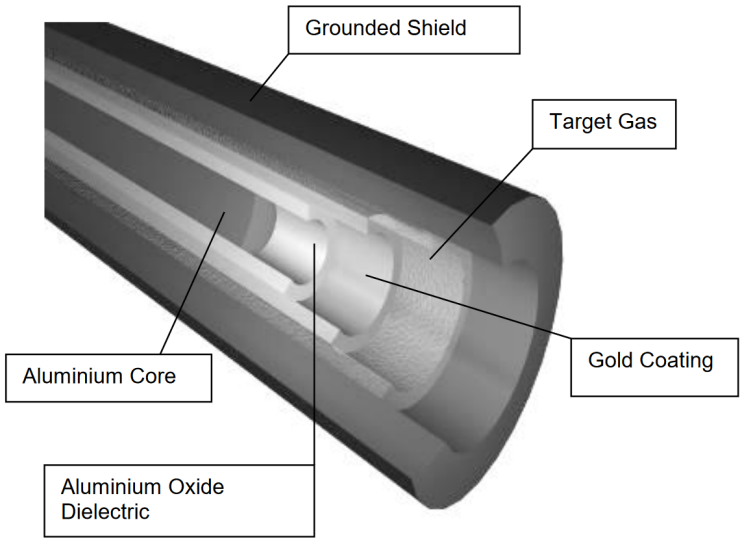

Figure 3.7.: Schematic overview of the probe in the MM400 (components are labeled), from [75]

aluminium rod. This creates a capacitor with the aluminium oxide acting as dielectric. The setup can be seen in figure 3.7. The sample gas flows around the rod which allows the aluminum oxide to take up water through the permeable gold coating, creating an equilibrium depending on the water content of the gas. This water acts as a second dielectric and therefore changes the capacitance of the rod setup, creating a direct dependence of the capacitance on the water content of the gas. To be more precise, the added capacitance by the water is in good approximation proportional to the dew point of the sample gas. This dew point measurement can then be converted into the concentration in ppm. This conversion depends on the pressure of the sample gas.

Pressure Chamber

In addition to the work done to accomodate the additional gases added to the detector, Robin Boshuis added a pressure chamber to the system during his master thesis work [76]. The box has inside dimensions of $410 \times 410 \times 145$ mm, which allows a complete resistive Micromegas detector to fit inside the chamber. It has been designed to cover a pressure range of 500 mbar(a) to 1500 mbar(a). To be able to hold the pressure, the vessel had to have a wall thickness of 8 mm, the floor and the lid had to be 12 mm, and the lid had to be fastened with 16 screwes around a 18 mm thick rim around the edge of the chamber. To seal the chamber, a rubber o-ring is set into the upper edge of the chamber walls. Three KF50 [77] norm flanges have been welded onto the sides, allowing for feed through of high

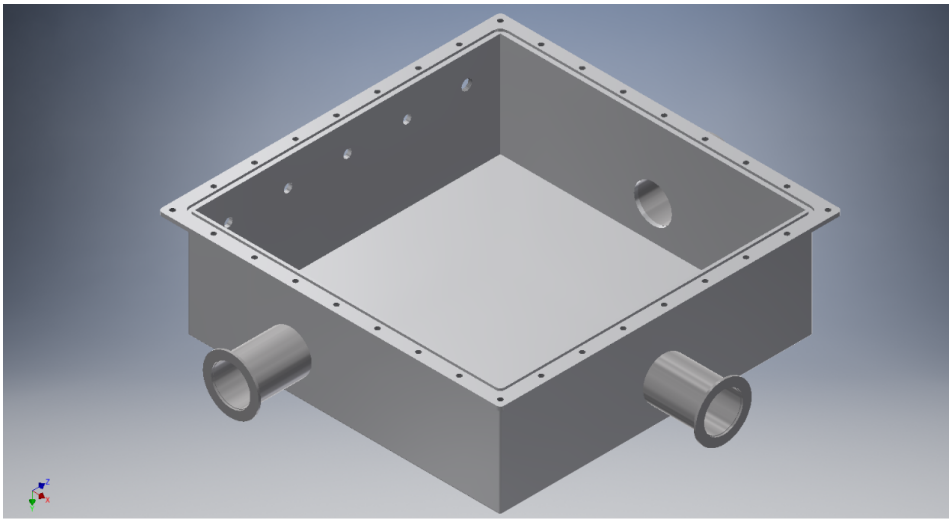

Figure 3.8.: CAD model of the pressure chamber as it was proposed to the manufacturing company, from [76]

voltage and signals. Blank flanges can be exchanged freely while the chamber is not pressurized to allow for any combinations of cabling, depending on the detector that is to be used with the chamber. Four feedthroughs for gas pipes are set into one of the four walls. A CAD-model of the detector can be seen in figure 3.8.

If the detector is already inside a small gas tight chamber, the pressure inside the box and the pressure inside the detector chamber can be controlled separately, with the pressure in the Box being regulated by a Bronkhorst P-702CV absolute pressure controller[78], while the pressure inside the detector is regulated by a P-506 relative pressure controller[78] and set to just above the pressure in the chamber. To avoid any accidents, a 1 bar(g) safety valve is fitted into a fifth hole in the side of the detector.

3.3.3. Regulating Contaminations

While the system is setup to control the flows of the different gasses directly, especially for gas humidity, the flow through the bubbler changes with temperature and pressure. As such, the gas flows must be regulated constantly using software. The software used in the lab is written in LabView. A first version was developed when the first gas system was built, but it suffered from crashes and minor bugs. For the new system, which is much more complex, the software had to be rewritten starting from the basic version.

A picture of the front panel can be seen in 3.9. The bottom left part of the panel contains a schematic view of the mixing panel, in which each controller is represented by two values, the set value at the top and the current value at

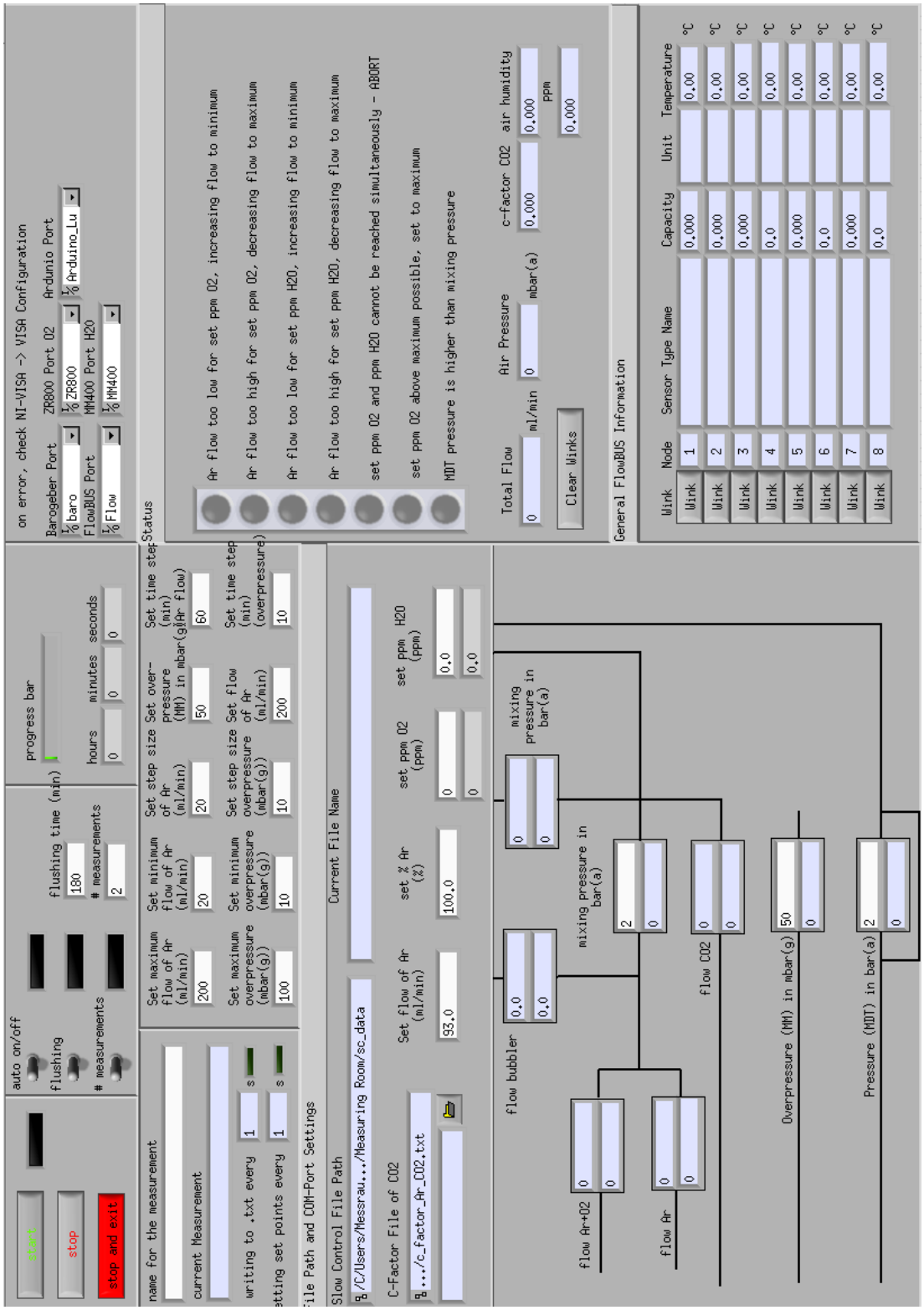

Figure 3.9.: Front panel of the Labview program used to control the gas system. All values can be set in the white fields, while grey fields show measurements and derived values. Warning light indicate errors.

the bottom. All set values with white backgrounds can be set directly, like the pressures, while the other set values are calculated from the values given above the schematic view. These include from left to right the desired total flow of argon, the ratio of argon in the final mixture without taking contaminants into account, the added oxygen in ppm and the added water in ppm. From these values, the program automatically calculates the settings of all flow controllers, adjusting the set total flow should one of the controllers exceed its limits. If the limits are exceeded or other warnings occur, the warning lights in the top right of the panel will light up. Below the warning panels are some derived measured values and other environmental measurements, like outside pressure and humidity. In the bottom right, the status and properties of all controllers can be seen. A click on the wink button will make a light on the respective controller light up. The top left contains settings for measurements, including an automatic variation of flows and pressure, the file name and other settings for logging and the buttons to start and stop the program.

3.4. Detectors

The lab is equipped with several different detectors. To create a hodoscope and to trigger other detectors, scintilators are used. The detector research is focused on Micromegas detectors. Other detector technologies with the same readouts as described in section 3.2.2 can be used as well. Different types of Micromegas detectors are available in the lab. The basic working principles of Micromegas detectors are explained in section 2.2.1. All these detectors will be described in further details in the following sections.

3.4.1. Scintilators

The sintillator system was already part of the lab before the upgrade began. The scintillators are made of BC-408 plastic scintillator material supplied by Saint-Gobain. All detectors are 1200 mm long and 25 mm thick and use the H7415 photomultiplier assembly by Hamamatsu to convert the scintillation photons into electric signals. In total, 30 detectors have been built, 14 of which have a width of 100 mm, 14 one of 200 mm and 2 have a width of 700 mm. The scintillators have been chosen to ensure a trigger hodoscope for one of the NSW SM2 can be built with them, while the largest ones lack position resolution but allow a classification of incoming triggered muons by their energy if used below the steel shield, which acts as energy filter. The photomultiplier tubes are supply via SHV connections using the high voltage supply, with a working point at around 1100 V and have

BNC connections that produce signals which can be read out using a combination of NIM electronics and TDC (see section 3.2.2).

3.4.2. Bulk Micromegas

Two bulk Micromegas have been provided to Würzburg by CEA, Saclay, France. They do not contain resistive protections for the anode, which contains ten broad copper strips with gaps of ≈0.1 mm, which are then shorted and read out together. The active area of the detectors is 9 × 9 cm. Both use the usual 45-18 mesh, one at a gap size of 128 µm and the other at 256 µm. To ensure a uniform gap size, the mesh is not only pushed against the pillars on the boards, but the pillars have been created while the mesh was already present, encasing the mesh inside the pillar structures, which where designed to be slightly larger than the gap size. The detectors do not feature a drift cathode or a gas volume, which had to be made for the detectors. For the drift, a fiberglass plate was prepared with four nylon screws and a piece of 70-30 mesh was glued onto a metal frame of dimensions 15 × 15 cm. The pressure chamber described in section 3.3.2 can serve as gas volume for the detector. To conserve gas and mitigate downtimes due to switching, smaller vessels with lower pressure requirements are being prepared. A picture of one of the detectors with and without the supporting structures can be seen in figure 3.10.

3.4.3. Resistive Micromegas

Resistive Micromegas can be procured as a kit from the CERN Micropattern Technologies group which is led by Rui de Oliveira[79]. The detectors have a readout board of dimensions 325 × 300 mm with an active area of 100 × 100 mm and can be ordered with different anode structures. The readout consists of resistive strips and either copper strips allowing for position sensitivity in one or two dimensions. Both a 1D and a 2D version of the detectors were bought for the lab. The 1D version has resistive strips that are antiparallel to the readout strips. Both have a width of 200 µm and a pitch of 250 µm. For the 2D version, the Y-layer is sandwiched between resistive layer and X-layer, with the Y-layer strips having a much lower width of 80 µm, to allow for capacitive coupling between the outer layers. The active area of the readout board is covered by a mesh that is glued onto the board using kapton foil to provide a distance of 128 µm. Using a lithographic process, cylindrical pyralux pillars of 500 µm diameter are created every 5 mm in the active area, fixating the mesh inside them and providing an even gap size across the detector. On the edges of the mesh, four holes for screws are provided. Nylon screws can be glued into the holes, providing a support for a second piece of mesh that has been stretched onto a frame, which is used as the cathode for the

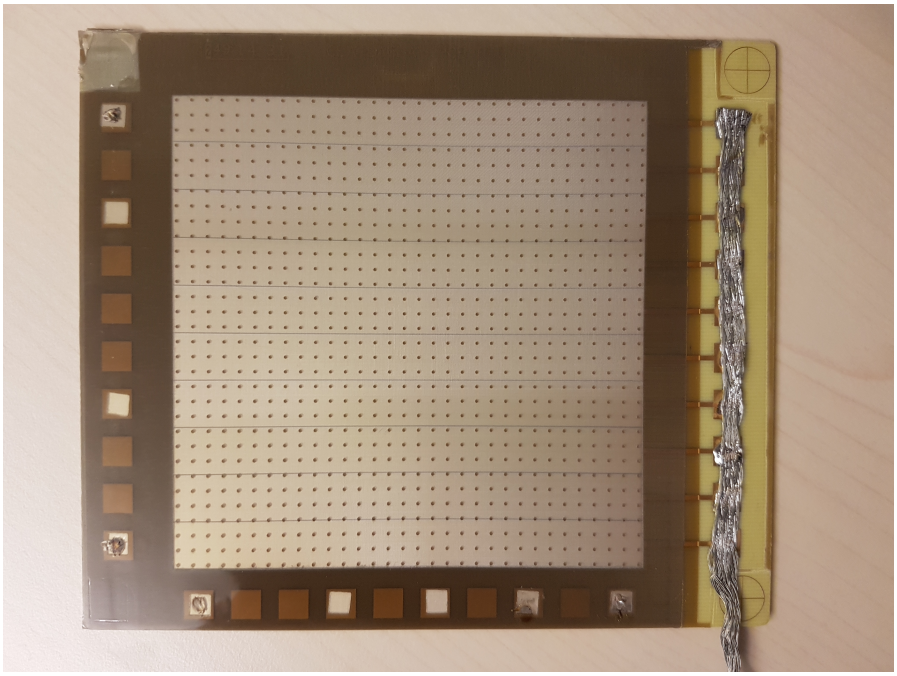

(a)

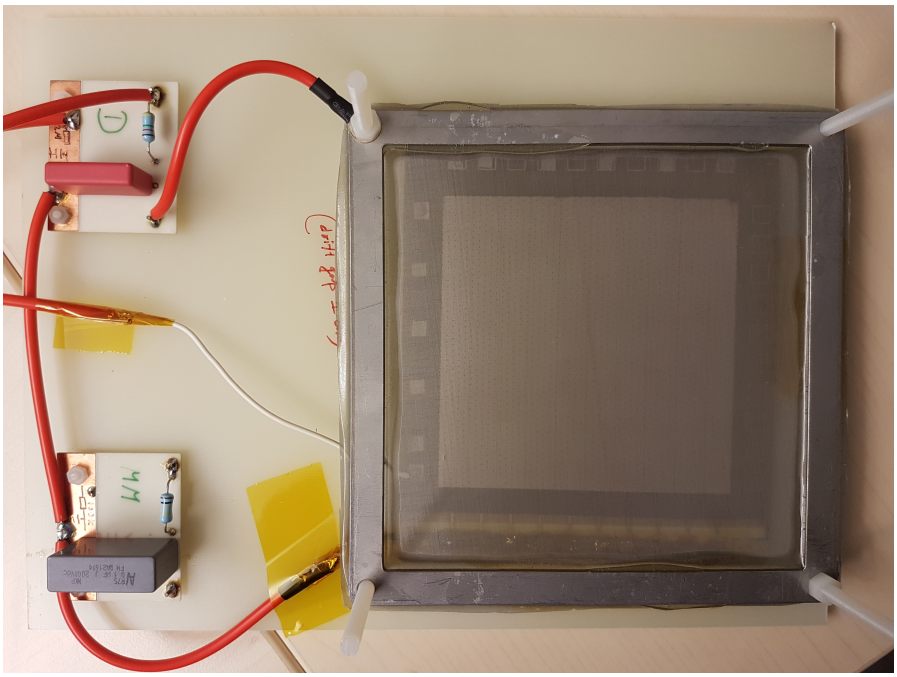

(b)

Figure 3.10.: (a) Photograph of the bulk detector, the anode strips are soldered together, (b) photograph of the bulk detector with fiberglas support, drift frame and eletronic connections and filter circuits.

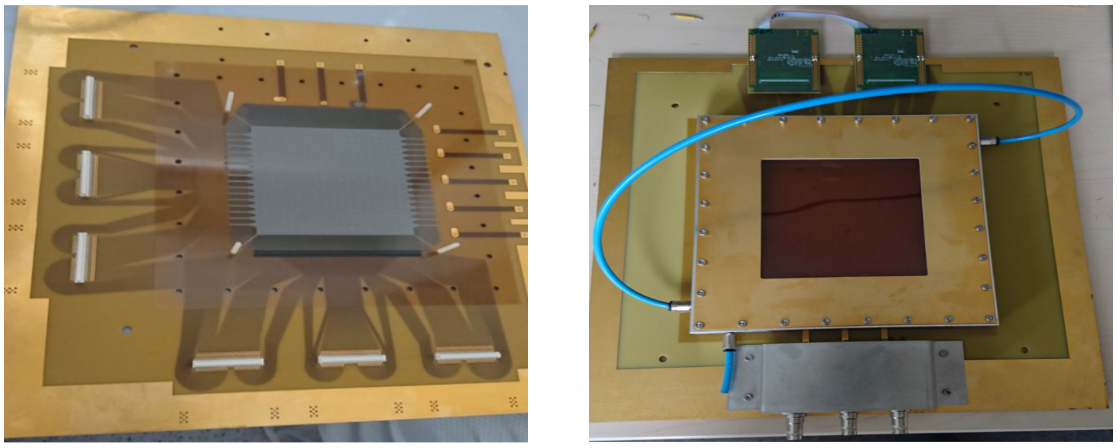

(a) (b)

Figure 3.11.: (a) Photograph of the 2D resistive detector, clearly visible are the 6 panasonic connectors and the strips leading into the active area, (b) photograph of the 1D resistive detector with the gas volume frame, the APV25s are connected at the top edge and the SHV connectors can be seen at the bottom edge, from [80]

drift field. Before the mesh is put on the screws, washer are used to create a gap of 5 mm, thereby creating an active detector volume of $100 \times 100 \times 5$ mm. The mesh is then gently fixed onto the screws with nuts and a small cable is used to connect the drift voltage input to the drift mesh. to generate the gas volume, a square aluminium frame is screwed onto the board with 28 screws. The frame is grooved on both sides, so that a o-ring can be set into each of the grooves, providing a seal for the gas volume. On top of the frame, a Kapton foil is placed and a PCB frame with a 10×10 cm window above the active area is placed on top of that Kapton foil. These are again fixed with 28 screws, creating a $157 \times 157 \times 20$ mm gas volume. On the outside of the board, the strips are connected to 128 channel Panasonic connectors, onto which the APV25 hybrid boards can be connected (see section 3.2.2). On a 1D detector, two of these connections exist, while a 2D detector has three for each layer, a total of six. In addition, three SHV connectors are placed on one side of the readout board, for drift, mesh and anode voltage respectively. A picture of the detector can be seen in figure 3.11.

The procured detectors were constructed and tested by Thomas Schell in his bachelor thesis[80]. The test has been performed using the SRS readout system and muons. Charateristics of both detectors have been taken with different drift and amplification voltages. While the 1D-detector behaved as expected, the 2D detector showed a lower gain in the center than in the outer ring of the detector. This might have happened due to a detachment of the mesh from the pillars in

conjunction with deformations of the detector. A reinforcing plate was produced by the workshop to force the detector into a planar setup.

4. The Effect of Contaminations on Micromegas Performance

The theoretical background of the influence of contaminations has been discussed in chapter 2.3. This chapter will first include investigations into sources of contaminations, like the gas tightness of the detector and plastic piping. The discussion will then show simulations of full detectors at different levels of contaminations using Garfield++. After that, measurements of the effect of these contaminations will be discussed.

4.1. Gas Tightness of the Micromegas

By the way they are constructed, micropattern detectors are never fully gas tight. Designed for low pressure, gaskets are used to seal the seam between frame and front and back plate. While they are mostly tight, small leaks can still cause contamination of the detector gas. Gases with high partial pressures in the ambient air, like nitrogen and oxygen, can enter the detector through backflow. In addition, low pressure gaskets are usually made of rubber material. This material can absorp and thereby tranport water through the seal into the detector[81].

4.2. Traditional Plastic Piping in Gas Systems

The piping used in many experiments is made of plastic because of its flexibility, material budget, and cost. As opposed to metal, in which the atoms are close together, plastic consists of long polymer chains. These chains do not fit neatly next to each other, leaving holes through which gas can enter or leave the pipe. The channels allow oxygen and water vapor from the air to enter the detector gas. In a simple model, one can assume that the pipe wall is similar to a membrane, which allows atoms to pass with a certain probability T per time intervall. For a stationary gas inside the pipe, this would lead to a differential equation of the form

$$\frac{dc}{dt} = T(c_{\text{out}} - c), \tag{4.1}$$

where c is the concentration of the contaminant inside the pipe, and c_{out} the one outside. If the velocity of the gas is large enough and laminar flow conditions are met, the gas in the pipe will follow Hagen-Poiseuille laws. However, if the diffusion of the oxygen inside the gas in the pipe is fast enough, the non-uniformity of flow may be neglected. Under this assumption, for a uniformly flowing gas inside pipe at equilibrium, the pipe can be seen as a row of boxes of infinitesimal length that are passed by the gas one after the other. The gas exchanges atoms with the outside until it leaves the pipe at time

$$t_{\max} = \frac{\sigma}{f} l, \tag{4.2}$$

where σ denotes the cross-sectional area of the pipe, f is the flow, and l the length. With the solution of the differential equation in 4.1,

$$c(t) \propto c_{\text{out}} \left(1 - e^{-Tt}\right), \tag{4.3}$$

and the relation in 4.2, one can obtain the concentration inside the gas after passing through the pipe depending on the length of the pipe as

$$c(l) \propto c_{\text{out}} \left(1 - \exp\left(-T\frac{\sigma}{f} l\right)\right). \tag{4.4}$$

If the pipe is short enough so that $\sigma l \ll f$, this can be simplified to

$$c \approx c_{\text{out}} \cdot T\frac{\sigma}{f} l. \tag{4.5}$$

As one can see, the contamination picked up by the gas in this model depends linearly on the velocity of the gas inside the pipe, or inversly on the flow. This dependency can be checked experimentally to verify the model. As will be shown later, depending on the pipe material, oxygen does infact exhibit a behaviour as explained by this model, while water displays a $\sqrt{1/f}$ dependency. This difference can be explained by assuming a different mechanism for transfer. Water can be absorped by plastic, making the process more like drying by blowing than an actual transfer between outside and inside through a membrane. Drying is a process which can be described by Fick's first law[82],

$$F = -D\frac{\partial c}{\partial x}. \tag{4.6}$$

F is the transfer rate per unit area, c the concentration of the water vapor and x is the distance inside the material along the permeation direction and D being the permeation coefficient of the material. In this case, the medium is assumed to

Material	Lengths	Inner Diameter
PFU	10 m, 9 m, 7 m, 2 m, 1 m	4 mm
PFA	6 m	4 mm
PTFE	10 m, 9 m, 7 m, 2 m, 1 m	5 mm, 4.5 mm, 4 mm, 3.7 mm

Table 4.1.: All variations of pipes measured in during the investigation.

exhibit isotropic permeability. One can show that this law leads to a differential equation of the form

$$\frac{\partial c}{\partial t} = D\frac{\partial^2 c}{\partial x^2}. \tag{4.7}$$

This equation has been solved for different scenarios, for example in [81] for the ratio of masses, which are proportional to the concentrations, assuming a thin film of material. Assuming again uniform flow through the pipe, one can approximate from this solution, that

$$\frac{c}{c_{\text{out}}} \propto \left(\frac{l}{f}\right)^{\frac{1}{2}}. \tag{4.8}$$

In addition to the flow dependence, this also explains why oxygen and water exhibit different behaviours off equilibrium. While the first assumption does not include the pipe as carrier of the permeant, the second one assumes that the pipe walls contain it. If the pipe does not contain any permeant, the new gas pushed into the pipe will already see the new steady state, while in the case of water, the pipe has to dry (or absorp water) slowly over time, until the new equilibrium is reached. The oxygen contamination curves taken after setting a new flow will therefore exhibit a fast (of the order of $\sigma l/f$) linear behaviour, since the packets measured will exhibit an average contamination with the times spent at the old flow and the new one as weights. For the water curves, however, the change in water contents of the pipe walls can be seen.

4.2.1. Method of Investigation

To study the mechanisms described in section 4.2, pipes made of different materials, and with different geometries were procured, as can be seen in table 4.1. Three different materials were used: Polytetrafluoroethylene (PTFE), Perfluoroalkoxy Alkane (PFA), an Polyurethane (PU). All pipes have an outer diameter of 6mm, with most having 4mm inner diameter. For PTFE, additional pipes with inner diameters of 5mm, 4.5mm and 3mm have been investigated. With the exception of PFA, 10m of each pipe have been bought, allowing an investigation into the influence of length of the pipes on the makeup of the detector gas.

The pipes are added to the gas system described in 3, replacing the Micromegas detector in the regular setup. Flow and pressure are then automatically varied by the system, while the measurements of the oxygen and the water sensor are logged every second. The flow is varied from 200 ml/min to 20 ml/min in steps of 20 ml/min and then back from 20 ml/min to 200 ml/min. After the flow measurements are completed, the pressure is varied from 100 mbar(g) to 10 mbar(g) in steps of 10 mbar. Each time a new flow or pressure is set, the concentrations of contaminants of the gas inside the system needs to get back into equilibrium. If this return to equilibrium is quick, the value of the new equilibrium can simply be read off. If this process is slow, the determination is slightly more involved. The contamination can be plotted against the time and the new value of the equilibrium can be extracted by a fit. In this investigation, the oxygen contamination has been of the first type, while the water contamination has been of the latter. Examples of fast and slow changes can be seen in figure 4.1 and 4.2, respectively. The fit function used is

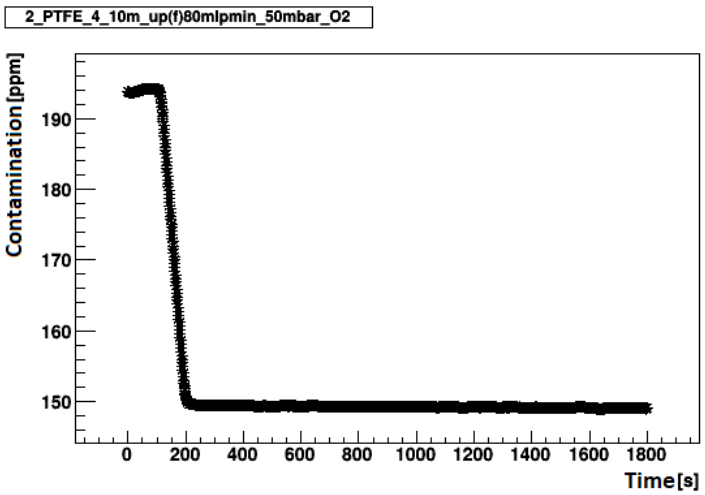

Figure 4.1.: Concentration change of O_2 inside a PTFE pipe of length 10 m and an inner diameter of 4 mm at a flow of 80 ml/min, from [73]

$$c(t) = y_{\text{asym}} - Ae^{-bt}. \tag{4.9}$$

In this equation, the equilibrium value is represented by y_{asym}, A is an arbitrary factor, which depends on the difference between the equilibrium value of the measurement before and the one that is being measured, and b being a parameter determining how quickly the equilibrium sets in in a given pipe. Once the equilibrium value for each flow or pressure has been extracted at a given material, length, and geometry of pipe, they can be added into a graph. The pressure measurements exhibit a linear behaviour and can be discussed as is, while the flow dependence

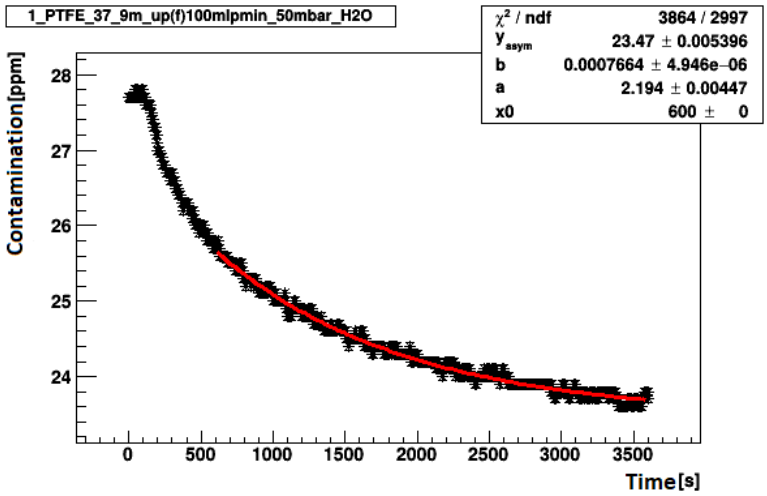

Figure 4.2.: Concentration change of H_2O inside a PTFE pipe of length 9 m and an inner diameter of 3.7 mm at a flow of 100 ml/min, from [73]

is more complicated. An example graph for a flow-variation can be seen in figure 4.3.

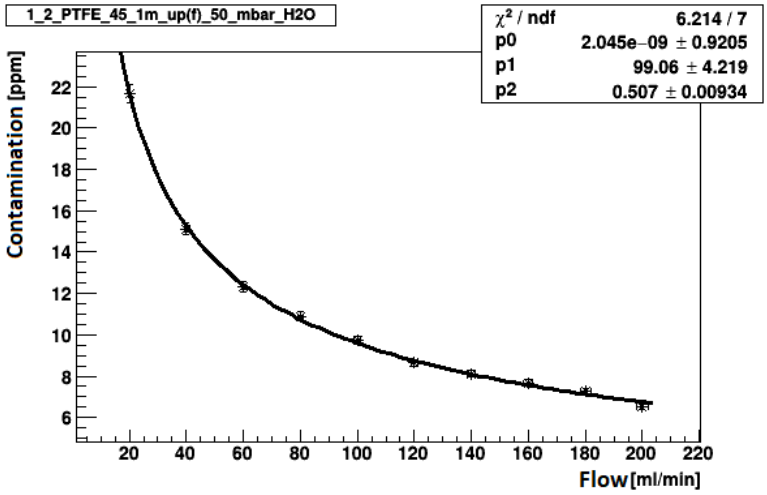

Figure 4.3.: Flow Dependency in 9 m of PTFE with diameter of 3.7 mm, from [73]

From this graph, flow independent measures for the permeability of the pipe under investigation can be extracted, again using a fit. Assuming the contamination picked up depends on the time the gas spends inside the pipe, it should inversely depend on the flow, i.e. the velocity of the gas. The fit function used is

$$c(f) = p_0 + p_1 \cdot f^{-p_2}. \tag{4.10}$$

Where p_0 denotes a flow independent contribution to the contamination, p_1 is the flow-independent measure of the permeability of the given pipe, and p_2 is a measure for the dependence of the contaminations on the flow, giving a hint on the mechanism of transfer causing the permeability. The p_1 can then be easily compared between the different materials, geometries, and lengths.

4.2.2. Measurements

The measurements taken are shown in table 4.2 and have been described in the bachelor thesis by Florian Wirth[73]. Several outside influences on the results have been identified. During the first measurements, the pressure measurements were taken at a flow of 100 ml/min. Therefore, the flow changed at the beginning of the pressure measurements, leading to an overlap of pressure and flow measurement. As the change in concentration due to flow changes is much larger than the change due to pressure, the determination of the concentration change due to pressure was made unnecesserarily harder. To evade this problem, all pressure measurements taken from that point onwards have been made at the flow which had been set last, 200 ml/min.

In order to identify the time needed per measurement, several test measurements have been made. Especially in PU pipes, the water content only slowly reaches the equilibrium, making longer measurements necessary. An example can be seen in figure 4.4. For shorter pipes, the change in concentration between measurements is smaller. Therefore, an additional increase in measurement times is necessary.

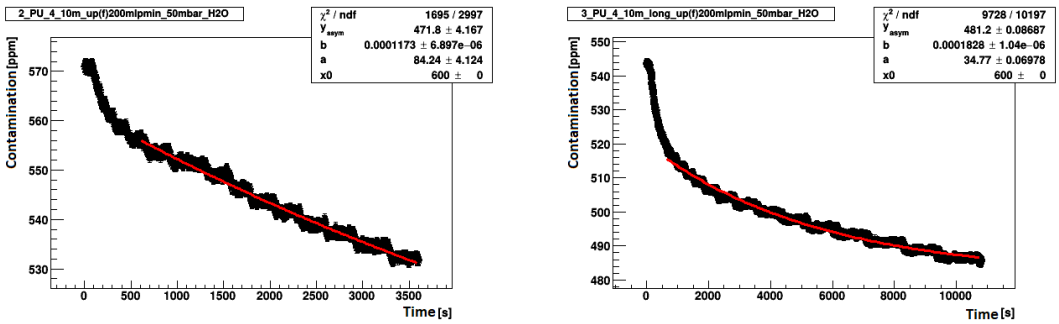

Figure 4.4.: Comparison between measurements of different length for the same pipe. (a) has been measured for 60 min, (b) for 180 min, from [73]

An additional feature appeared at certain times of day in several measurements. When the sun shines into the lab in the late afternoon, the contamination curves taken exhibited sudden changes, as can be seen in figure 4.5. These changes could

Material	Inner Diameter	Length	# of Runs	t_f [min]	t_p [min]
pressure measurement at 100 ml/min					
PTFE	4.5 mm	10.22 m	2	30+30	10
PTFE	3.7 mm	10.37 m	2	30+15	10
PTFE	4.0 mm	10.24 m	2	15+30	10
PTFE	5.0 mm	10.11 m	1	30	10
from here 200 ml/min during pressure measurements					
PTFE	5.0 mm	10.11 m	1	60	10
PU	4.0 mm	9.98 m	3	60+60+180	10
PTFE	4.5 mm	9.22 m	2	60+60	10
PTFE	3.7 mm	9.37 m	2	60+60	10
PTFE	4.0 mm	9.24 m	2	60+60	10
PU	4.0 mm	8.98 m	2	180+180	30
measured twice					
PTFE	5.0 mm	9.11 m	1	60	10
PTFE	4.5 mm	1.00 m	1	60	10
PTFE	4.5 mm	1.00 m	1	120	10
PTFE	3.7 mm	1.00 m	1	120	10
PTFE	4.5 mm	7.22 m	1	60	10
measured only once					
PTFE	4.5 mm	2.00 m	1	180	10

Table 4.2.: All measurements with properties.

be explained by an expansion of the pipe material due to the heating by direct sunlight. While the pipe is extending, its volume changes, reducing the flow of the gas inside the pipe. This would then change the amount of contaminations picked up, leading to a change towards higher contaminations. Once the sun has moved away from the pipe, the expansion stops, and the value returns back to the expected equilibrium value. If care is taken to avoid the area the sun hits with the pipes, the effect does not occur.

From these measurements, the flow-independent measurements are extracted as explained in 4.2.1. In the following section, the measurements will be analyzed and the material and geometric properties of the pipes will be determined.

4.2.3. Results

For every combination of length, material, pipe geometry and contamination, one flow-independent factor has been obtained. The way this is done depends on the contamination and was explained in chapter 4.2.1. For the three different ma-

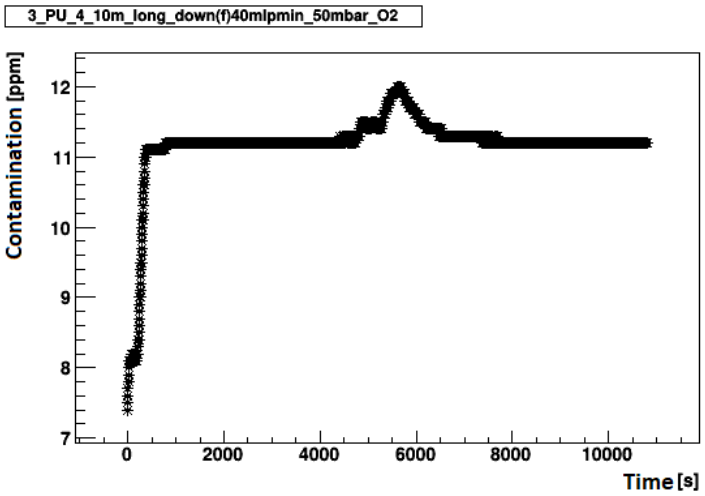

Figure 4.5.: Measurement of O_2 during which a bump in the measured concentration occured, likely caused by heating through direct sunlight, from [73]

Material	p_1 for O_2	p_2 for O_2	p_1 for H_2O	p_2 for H_2O
PU	450 ± 25	1.001 ± 0.012	8000 ± 240	0.40 ± 0.04
PFA	3660 ± 190	0.867 ± 0.012	770 ± 110	0.65 ± 0.05
PTFE	6400 ± 350	0.870 ± 0.012	340 ± 15	0.87 ± 0.06

Table 4.3.: Results for the different materials at 9 m. PFA is measured at 6 m and scaled up. The values for p_1 are in ppm $(\mathrm{ml/min})^{p_2}$

terials, the measured flow-independent contaminations can be seen in table 4.3. The measurement for PFA has been performed at a length of 6 m and scaled up to 9 m. As can be seen, the different materials behave very diffently. While PU allows little oxygen to enter the detector gas, it allows rather large amounts of water. For PTFE, the relation is the other way around. PFA exhibits a smaller difference between oxygen and water, while being in the middle in terms of total contamination in both. For all pipes, the flow-independent contribution is compatible with 0. The nature of the transfer is seen in p_2. For PU, oxygen seems to behave as has been expected from the membrane, with no oxygen being permeated in the pipe material. The materials containing fluorite seem to instead have a mixture of both processes at the same time. For water, none of the pipes is close to purely membrane like behaviour, with PU exhibiting an even lower than square root behaviour, while the fluorite materials again exhibit a mixture of the two behaviours.

Results for the concentration of water and oxygen depending on the length of the pipe can be seen in figure 4.6. As one can see, the results show a close to linear

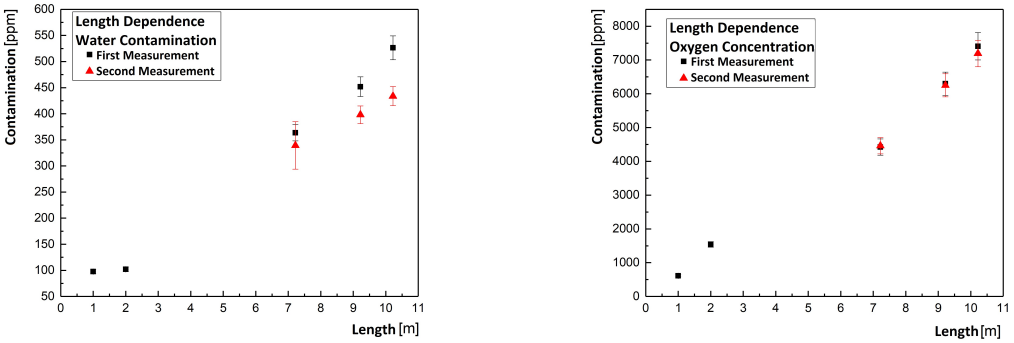

(a) (b)

Figure 4.6.: Concentration change of (a) H_2O and (b) O_2 depending on the length of the pipe, from [73]

behaviour, with good reproducability with respect to oxygen. For water, the square root behaviour cannot be seen. Also, the results vary in-between measurements due to the change in ambient humidity. Due to the complicated nature of the transfer, the effect could not be eliminated from the measurements. The influence of the inner diameter on the concentrations of oxygen and water can be seen in figure 4.7 for a PTFE pipe of 9 m length.

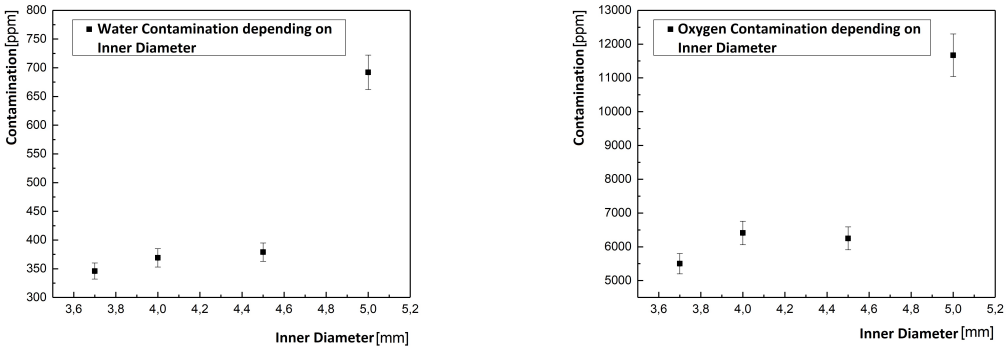

(a) (b)

Figure 4.7.: Concentration change of (a) H_2O and (b) O_2 depending on the inner diameter of the 9 m long PTFE pipe, from [73]

The dependence does not appear straightforward, with the contamination seemingly stagnating between 4 mm and 4.5 mm. The reason for this stagnation could

not be determined, as other inner diameters were not available for purchase and therefore the interesting region could not be probed at other values. Overall, the influence on the gas quality exhibited by the gas pipe could be shown and quantified, giving valuable information for large-scale experiments with hundreds of meters or even kilometers of piping involved total.

4.3. Simulation on the Effects of Contaminations

To gauge the effects of contaminations on the detector before planning the required ranges for the gas system, a monte carlo simulation using Garfield++ was performed. In this simulation, a Micromegas detector has been simulated with a full micro-mesh structure, with different concentrations of oxygen and water. For each data point, 10000 photons were simulated, with full microscopic tracking of the resulting electrons. First, a quick introduction into Garfield++ and to the simulation that is performed will be given. Then, the results are presented.

4.3.1. Garfield++ and the Simulation

Garfield++ is developed and maintained by Rob Veenhof and Heinrich Schindler[83]. The software provides a simulation framework for gaseous particle detectors. Given an electric (and magnetic) field configuration, it can simulate the entire interactions from the creation of primary ionisation via the drift of those primaries, to the amplification cascade, either using monte carlo methods or in a fully microscopic fashion, if desired. The gas properties are calculated using Magboltz, which was developed by Stephen Biagi [84], providing ionisation cross-sections for all combinations of particle energies and energy levels. Once the electron gets freed, it will loose excess kinetic energy by ionising more argon atoms until it reaches thermal kinetic energy. This process is simulated using HEED[85], written by I. Smirnov. Microscopic tracking includes following each created electron, primary and secondary, in time steps through the detector, taking into account the fields in the detector and the gas mixture. In each time step, the probability of an electron colliding with an atom or molecule for every outcome is calculated and one outcome chosen randomly using these probabilities.

The simulation that will be discussed in the following section uses a field map that was produced using ANSYS 16, a commercially available finite element solver for electricmagnetic fields, to generate a full field map of a Micromegas detector. This field map is then fed into Garfield++ and several muons or photons are tracked through the detector. These interact with the detector gas to produce electrons, which are then individually tracked through the detector to generate a signal on a single copper anode. Several values are written out for every electron in the

avalanche: The position of the endpoint of the electron, the time at which it hit this endpoint was reached and its status, or reason for termination of tracking (usually attachment or leaving the gas volume). For each primary electron, the size of the avalanche is recorded and for each cluster of electrons created in one interaction of muons or photons with the gas, the number of primary electrons is recorded. For each event, the total signal strength, or the sum of all electrons in all clusters, and for muons also the number of clusters in the event are recorded. To be able to calculate the mesh transparency, the number of primary electrons that get attached in the drift volume and the number of primary electrons absorbed by the mesh are recorded. The electron transparency is calculated using different definitions. One only applies the ratio between primaries absorbed by the mesh and total primaries reaching the mesh (the true transparency), while the other definitions also include the attachment of electrons to the detector gas before the primary can reach the micro-mesh in the enumerator. The latter is the transparency that is more accessible in experiments, as one cannot differentiate between attached primaries and absorbed primaries. Both versions are saved for comparison. The output in the shape of a *.root* file can then be analyzed further using scripts.

In addition to the raw electron signal, the induced electron signal on the anode and readout electronics can be simulated, giving a signal similar to the signal seen in the real detector. This is also added to the output files as histograms for each event. From the height of these signals, one can perform the same analysis as with the raw signals, with a scaling difference coming from the gain of the chosen amplifier. The simulations presented here were produced using an electric field map of a minimal cell of a Micromegas detector. A picture of the calculated potential can be seen in figure 4.8. This cell is then repeated infinitely in x- and y-direction while being mirrored, creating an infinite planar Micromegas detector. The mesh used in the simulation has a pitch of 45 µm and wire thickness of 18 µm. The amplification gap is set to 128 µm and the detector itself is 5 mm large in z-direction. The gas was set to a ratio of 93:7 Ar:CO_2, with differing concentrations of O_2 and H_2O being applied. These additions ranged from 0 ppm up to 10000 ppm. For all combinations, the micro-mesh is set to a voltage of -580 V and the cathode is at -750 V.

4.3.2. Simulation Results

From the simulation results, the avalanche size for each primary electron, the number of electrons on the anode for each photon, the signal induced on the anode and the signal after electronics simulation are extracted. The avalanche size is fitted with a polya function (see section 2.1.3). All other distributions are fitted with a gaussian. One example of these fits can be seen in figure 4.9.

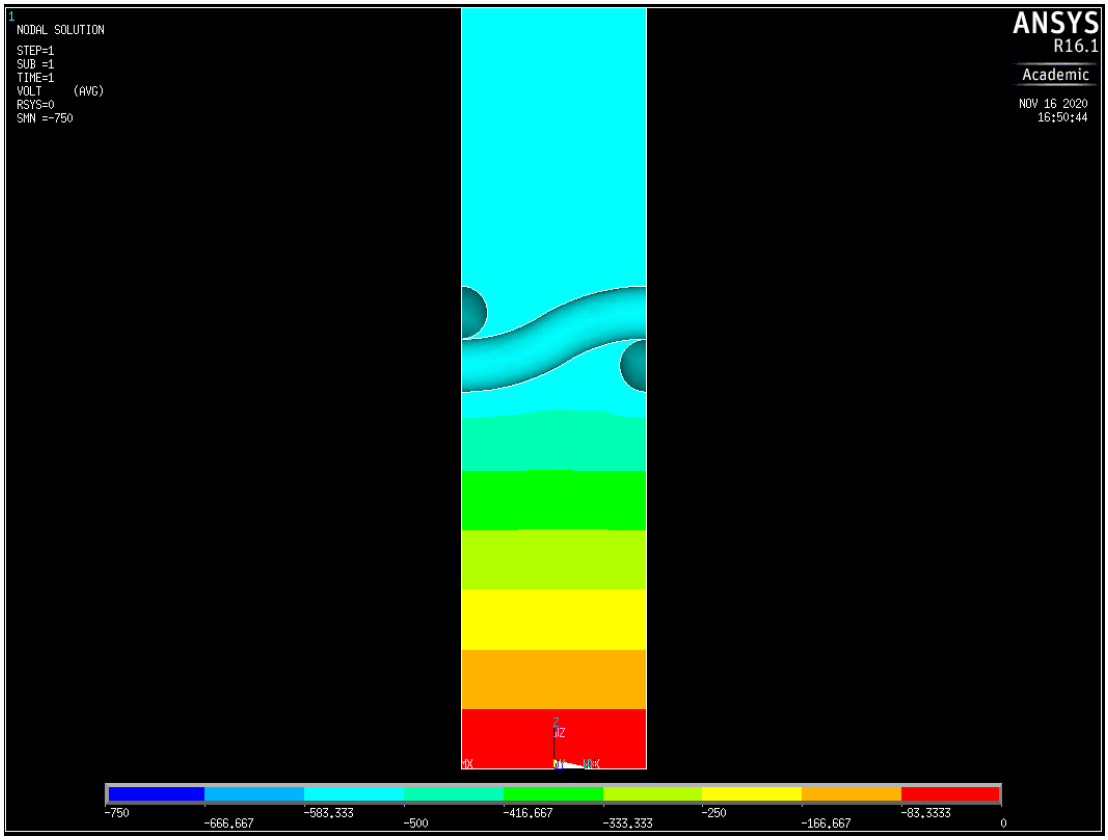

Figure 4.8.: Field map used in the simulation of the Micromegas detector in the lab. The view is zoomed onto the amplification gap to make the mesh structure visible.

Especially for high concentrations of O_2, the resulting spectra diverge from a simple gaussian. The reason for this is geometry. Since primaries are created close to equally along the z-axis in the detector volume, some primaries will have a shorter path in the drift volume as others, thereby decreasing the probability of attachement. This can be seen in figure 4.10.

The probability to survive drops exponentially with the distance the electron travelled in the drift field. Therefore, if the photoionization takes place very close to the mesh, it will cause a signal very much like the signal without oxygen contamination, while the photoionizations very close to the cathode will generate very small signals. This comparison can be seen in figure 4.11.

Here, interactions in two 400 µm large slices of the detector, one directly above the mesh and one directly below the anode, are compared for no oxygen and 10000 ppm of oxygen. One can clearly see that in both cases the slices right above the mesh show the regular signal without any influence by the oxygen, while the

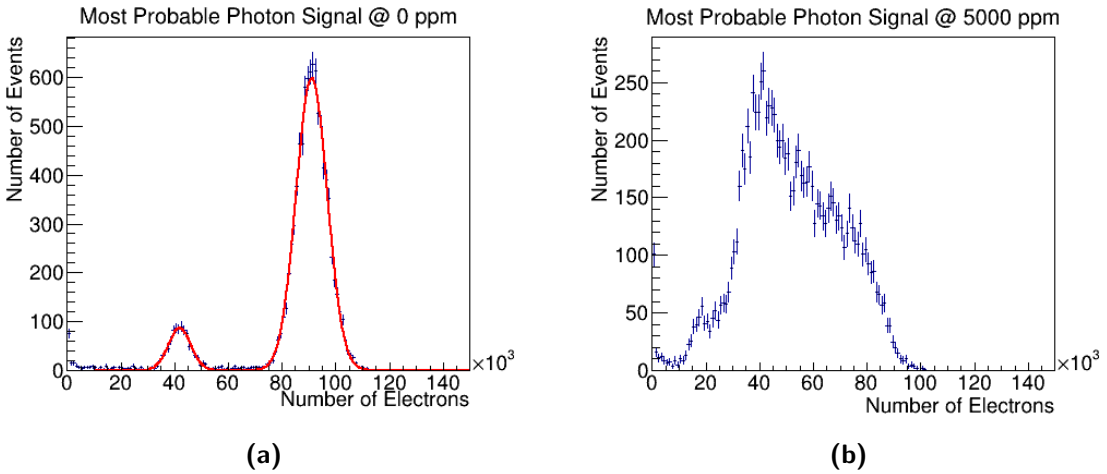

Figure 4.9.: Spectrum of the signal in electron numbers for (a) 0 ppm O_2 (with fit) and (b) 5000 ppm O_2 (without fit).

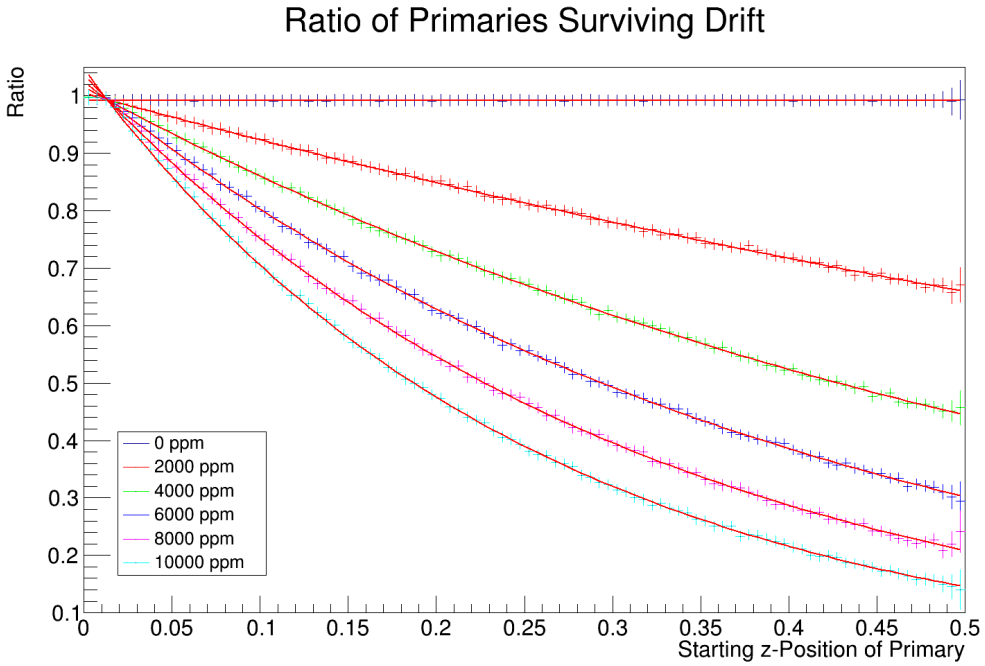

Figure 4.10.: Ratio of attached primaries depending on the distance from the anode the primaries were created at different oxygen concentrations. Distances are given measured in cm from the anode. The mesh is at 128 µm, the cathode at 5 mm.

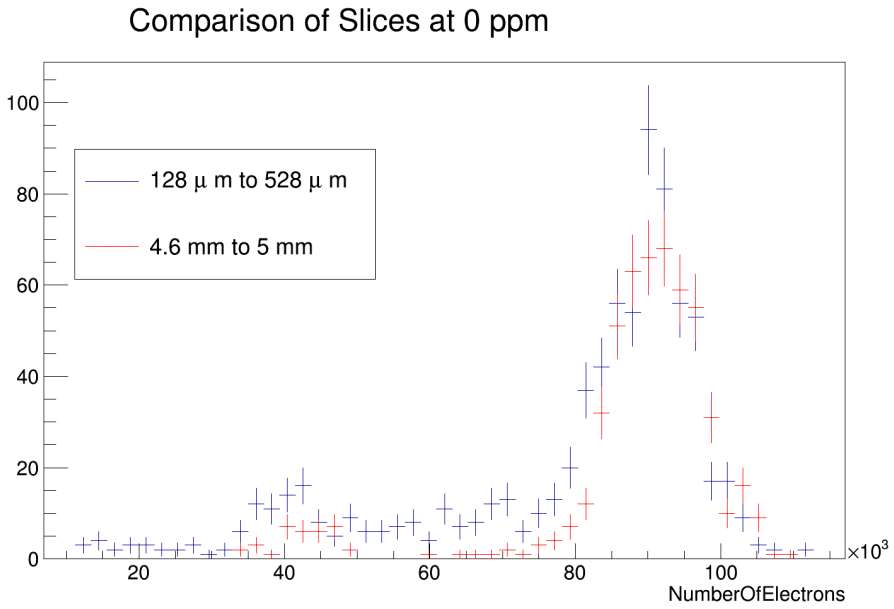

(a)

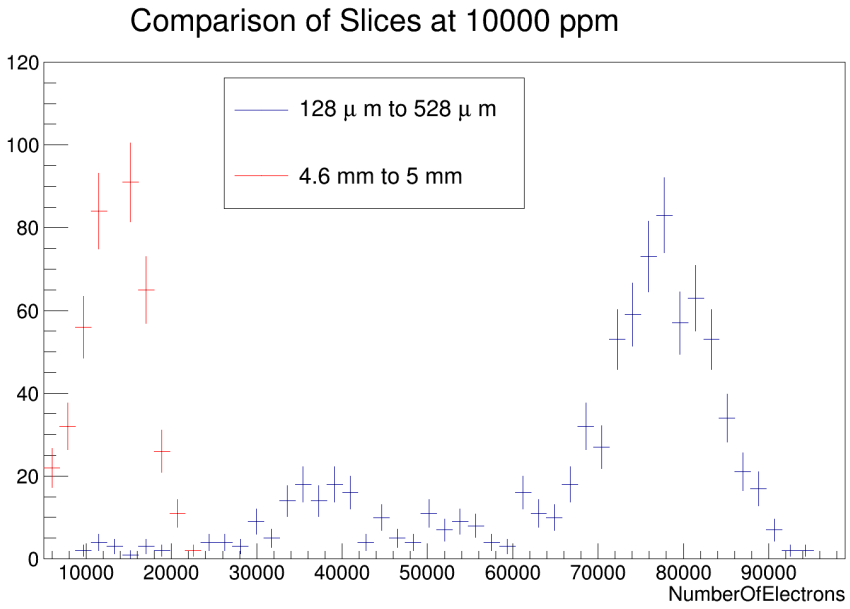

(b)

Figure 4.11.: Comparison of two different z-slices in the detector, measured from the anode, (a) at 0 ppm oxygen, (b) at 10000 ppm oxygen.

slice at the anode shows a clear sign of attenuation at high oxygen concentration. This will cause the spectra at high oxygen concentration to no longer be shaped like

a gaussian, but more like the sum of many different gaussians stacked on top of each other with increasing mean and width. Since the loss of primaries is exponential, this also means that the size of the drift volume is very important. Detectors with smaller drift volumes will be influenced less by oxygen contaminations than ones with larger volumes (in z-direction).

Especially for very high concentrations, this makes fitting a meaningful gaussian complicated. To mitigate this effect, from 3000 ppm onwards, the maximum value of the histogram is taken instead of a gauss. For each value, the means or maxima can be plotted to gain an understanding of the expected effects of oxygen on the detector. The resulting gain for primaries that reach the amplification gap and signal strength (in photon numbers) can be seen in figure 4.12. The gain linearly decreases only by about 5% over the 10000 ppm, while the signal is reduced linearly by almost 90%. This implies that the main reason for the loss of signal lies in mechanisms that take place before the amplification begins.

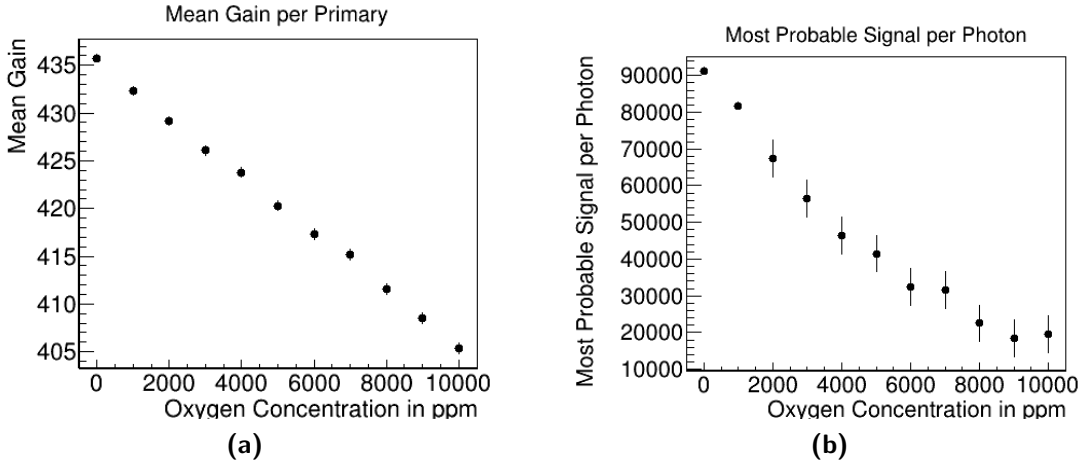

Figure 4.12.: (a) gain of the detector and (b) signal strength for a photon at different concentrations of oxygen.

4.4. Measurements of the Gas Gain in Micromegas Performance

The measurements presented in this chapter have been made using the MCA-method explained in section 3.2.2 and the resistive Micromegas detectors described in section 3.4.3, with an amplification gap of 128 µm and a nominal drift gap size of 5 mm. The signal was taken from the mesh, shaped, amplified and digitised. The resulting energy spectrum was recorded and then fitted with a gauss function

using a two step process. First, a gauss was fitted using a fixed width window around the bin with the most entries in the histogram. The results of that fit were put as starting values into another gauss fit, using a window around the maximum of the first fit within the range of $[\mu - 1.5\sigma, \mu + 1.5\sigma]$. An example of the second fit can be seen in figure 4.13.

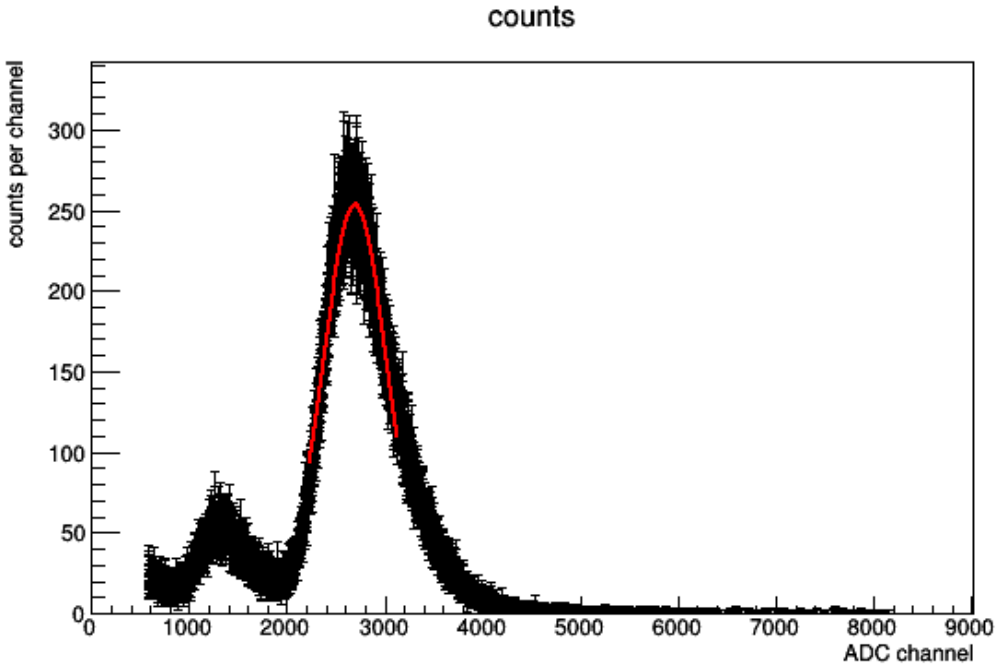

Figure 4.13.: Example of a fitted peak in the data taken with the MCA at an amplification voltage 570 V and cathode voltage of 750 V (360 V/cm).

4.4.1. Calibration of the Readout Electronics and Contamination Measurement Devices

Before measurements can begin, the readout electronics can be calibrated. To perform the calibration of the readout electronics, a function generator and a charge injector can be used to generate a known charge signal on the preamplifier. The charge injector converts a voltage pulse coming from a pulse generator into a corresponging charge. The amplitude of the signal will be proportional to the charge injected. The circuit diagram, including the properties of every element, can be seen in figure 4.14. It consist of a 50 Ω resistance between ground and the input signal, with the output coupled to the input by a 1 pF capacitor.

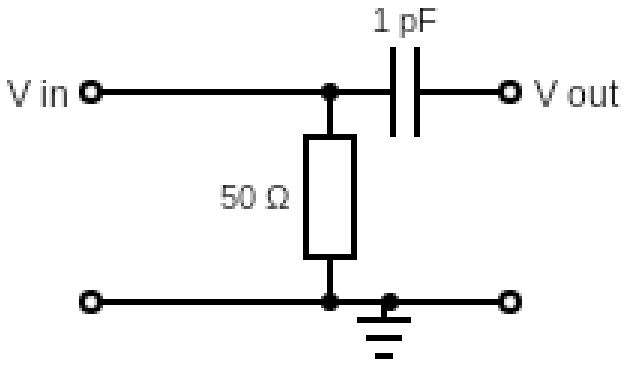

Figure 4.14.: Schematic of the charge injection circuit used to calibrate the MCA.

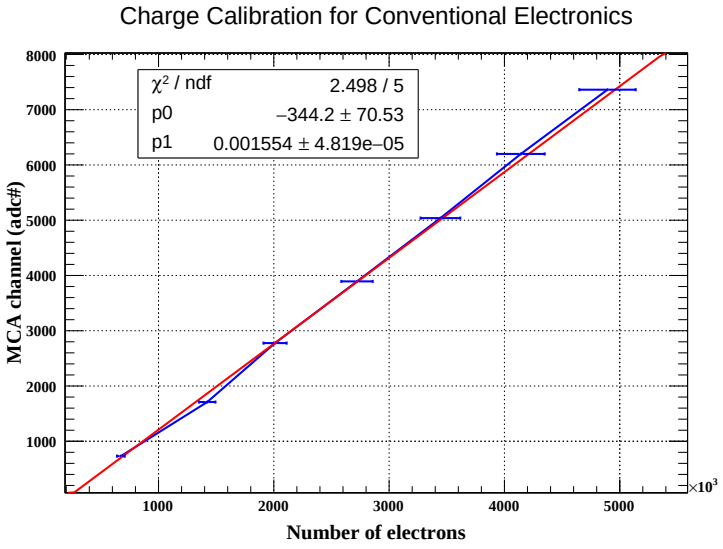

Figure 4.15.: Calibration curve of the MCA, including a linear fit.

For the calibration seen in figure 4.15, data was taken using a Keysight 33210A[86] on lend from the university electronics workshop. The flat-top pulse had a rise time of 25 ns and a width of 4.0 µs and was injected at a frequency of 2 kHz. The amplifier was set at an amplification of 55 times and a shaping time of 6 µs. The charge is injected at several voltage pulse amplitudes and the corresponding charge injected into the MCA is then plotted against the resulting channel number.

The calibration data was fitted with a linear function, the result of which can be seen in the plot. This calibration to the gain assumes that all approximately 210 primaries are available for amplification. As this is not the case for measurements

with oxygen, measurements in the subsequent chapters have been presented without calibration, as only ratios between the measurements are of interest and the gain of the detector cannot be calculated without precise knowledge of the average number of primaries reaching the amplification gap.

4.4.2. Measurements in a close to pure Ar:CO_2 mixture

Due to the necessary plastic piping and detector leaks, the detector gas will never be fully pure. However, impurities can be reduced as much as possible. In this case, oxygen concentrations are dropped to 60 ppm at 100 ml_n/min (including the piece of pipe after the detector), while the water concentrations inside the gas are in the same range, but depend on the outside humidity. No additional oxygen or water contaminations are added for this section.

In a first step, the working point for the detector has to be defined. This is done by choosing a reasonable drift voltage and increasing the amplification voltage until the signal is large enough. Once an amplification voltage has been chosen, the drift voltage can be scanned over to find the maximum. While the first spectra were taken, a new feature materialised.

The measurements were performed using a freshly bought source of ^{55}Fe, which with its nominal activity of 185 MBq caused a substantial amount of electrons created in the amplification gap at the same time. If the charges linger on the electrodes because the power supply is not able to remove them quickly enough, the amplification field will be reduced. This will reduce the gain of the detector, reducing the amount of charge produced and slowing down the voltage change until an equilibrium is reached. The effect of this charge up on the mean signal over time can be seen in figure 4.16.

The data was fitted with an exponential function. The time constant was fitted as (348 ± 6) s. The charge up is dependent on the charge created in the detector, which means that effects that are expected to change the signal strength would show a different charge up behaviour.

Before the measurements continued, a try was made to mitigate this effect. The filter circuit was removed and another measurement was taken. The reduction was still visible, albeit with a much faster decay rate. The next strategy to reduce this effect was a reduction of the rate of the source by collimation. A 5 mm plate of steel was taken with a hole of 1mm drilled into it. The source was placed on top of the hole, reducing the rate seen by the detector. This rate decrease mitigated the charge up, as can be seen in figure 4.17.

The settings of the amplifier had to be changed when the filter was removed, one reason being the increased noise, one being the changed signal shape. Therefore, the signal strengths cannot be compared between the measurements with and without filter. First, a scan of the amplification voltage can be performed at a

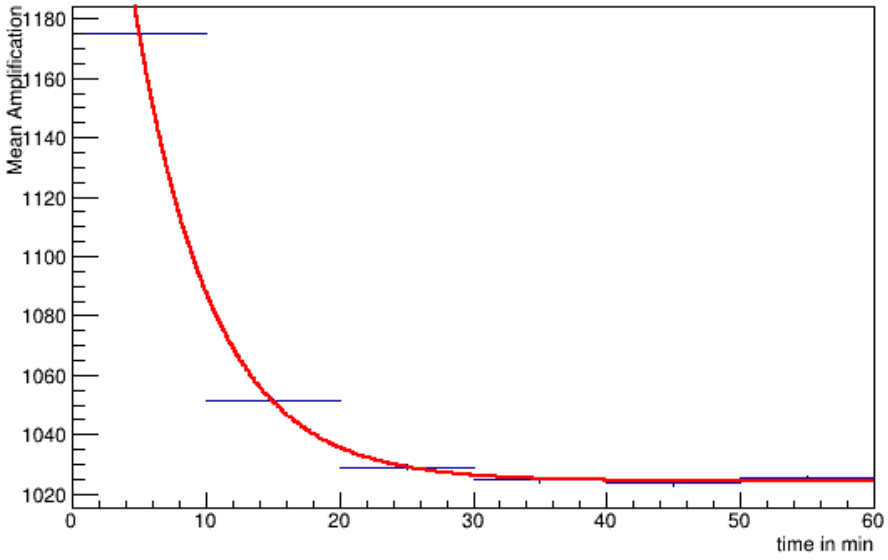

Figure 4.16.: The most probable signal over 60 minutes of measurements. The horizontal bars indicate the time intervall the individual measurement was taken in.

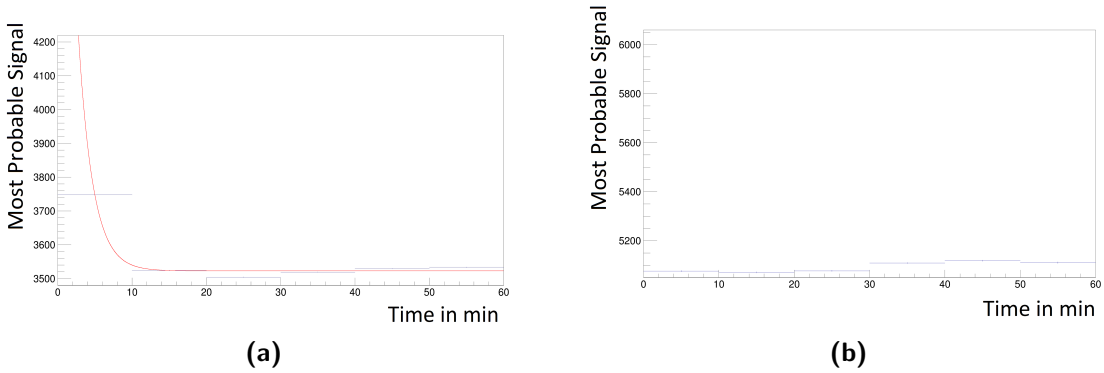

Figure 4.17.: Measurement of the charge up (a) without filter at full rate and (b) with collimator in place. The y-axis range has been chosen to be relatively the same as in figure 4.16. The charge up is much faster without filter and dissapears when the rate is low.

first guess drift field of 600 V/cm. The mean signal measurement can be seen in figure 4.18.

As it can be seen, the gain scales exponentially with the amplification voltage. The detector becomes unstable at 580 V, thus 570 V has been chosen as the

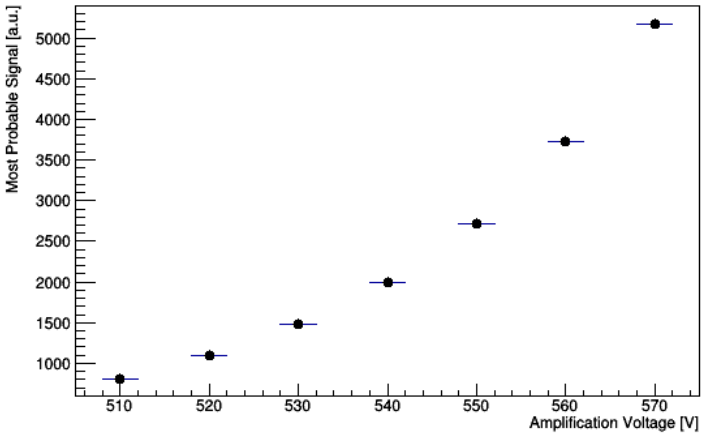

Figure 4.18.: The most probable signal for different amplification voltages. The drift field was set to 600 V/cm.

working voltage. Next, the optimal drift field was selected by performing a scan. The result can be seen in figure 4.19.

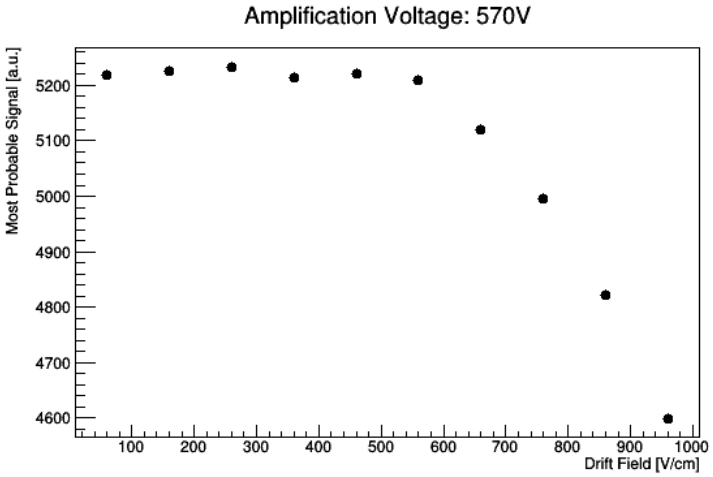

Figure 4.19.: The photo peak position for different drift fields at an amplification voltage of 570 V.

Usually, the photo peak position is exhibiting a plateau. In a low drift field, electrons drift slowly, making them susceptible to attachment. With a setup containing only very low amounts of contaminants, the probability is still close to none, thus the scan does not show a left flank, even at very small drift fields. For very high drift fields, the transparency reduces significantly as more and more

primary electrons get absorbed by the mesh, causing a drop in signal. This is independent of the chosen gas and therefore can be seen clearly, regardless of the oxygen or water contaminations in the detector.

In addition to the signal strength, the energy resolution of the detector can be investigated. This can be done by using the width of the fitted gauss curve in addition to the mean, using the definition

$$\frac{\Delta E}{E} = \frac{2\sqrt{2\ln 2}\sigma}{\mu}, \tag{4.11}$$

with σ and μ being the values extracted from the fit. The resolutions at different amplification voltages can be seen in figure 4.20. The resolution exhibits a minimum at 550 V. Therefore, measurements were not only performed at the maximum amplification voltage of 570 V, but also for 550 V.

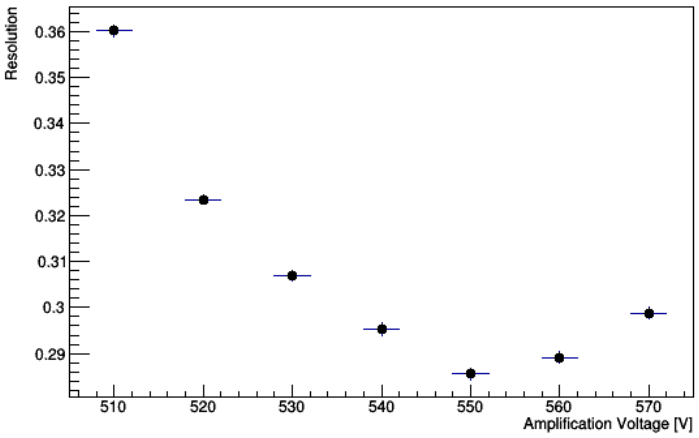

Figure 4.20.: The resolution for different amplification voltages at a drift field of 600 V/cm.

After the detector working point had been found, the measurements including oxygen were performed.

4.4.3. The Effects of Contaminations

After the working point has been determined, the contaminations can be added. Due to the fact that oxygen contaminations are easier to handle, the measurements are first performed with oxygen contaminations in a controlled manner using the gas system described in section 3.3.2. The oxygen contaminations are oriented on the finds of section 4.2.3, scaled up to large experiments with hundreds of

V_A in V	V_D in V/cm	concentration of O_2 in ppm
510, 520,..., 570	600	0, 1000,..., 10000
550	60, 160,..., 960	0, 1000, 4000, 10000
570	60, 160,..., 960	0, 1000, 4000, 10000, 17000
570	60, 360, 660	0, 1000,..., 10000

Table 4.4.: Measurements performed for the investigation into the effect of oxygen contaminations

meters of piping. During the first measurements with oxygen, large differences have been observed. During the day, the sun would appear in the window. Since the measurement room is not climate controlled, this had a large influence on the measured spectra during the day. To mitigate this, all measurements shown were performed during the night. Even then, some effects still persisted. These will be discussed in section 4.4.4.

The Effects of Oxygen

The measurements for the added oxygen contaminations are performed in the same way as the ones without, which have been presented in section 4.4.2. several measurements have been performed, which are listed in table 4.4. While changing the voltages applied to the detector only takes seconds, changing the contaminations in the gas takes 1-2 hours, depending on the flow rate of the gas, since the gas in the detector volume needs to be replaced slowly until the new concentration is reached. Therefore, where possible, voltages were scanned first at one contamination, after which the oxygen inflow was changed. Each measurement was taken for 10 min. During one night, only a few changes in oxygen could be made. Therefore, measurements were taken in the course of several nights. After a preliminary investigation of the first results, the absolute pressure in the detector was seen as vital, with large ambient pressure changes occuring during the days the data was taken in. To mitigate this, the measurements were performed at a pressure of 1000 mbar(a), set manually by calculating the needed overpressure. For the last measurements, where the drift fields of 60, 360 and 660 V/cm were measured at 570 V amplification voltage and differing oxygen concentrations, the system was set up to hold the pressure of 1000 mbar automatically, without the need for manual adjustments.

The result for amplification scans can be seen in figure 4.21.

As one can see, for the chosen drift field of 600 V/cm the effect of oxygen is not clearly visible, as there is no clear ordering of the values by contamination. In this case, environmental influences that have not been mitigated seem to have a greater effect on the measurements than oxygen. These effects seem to change on

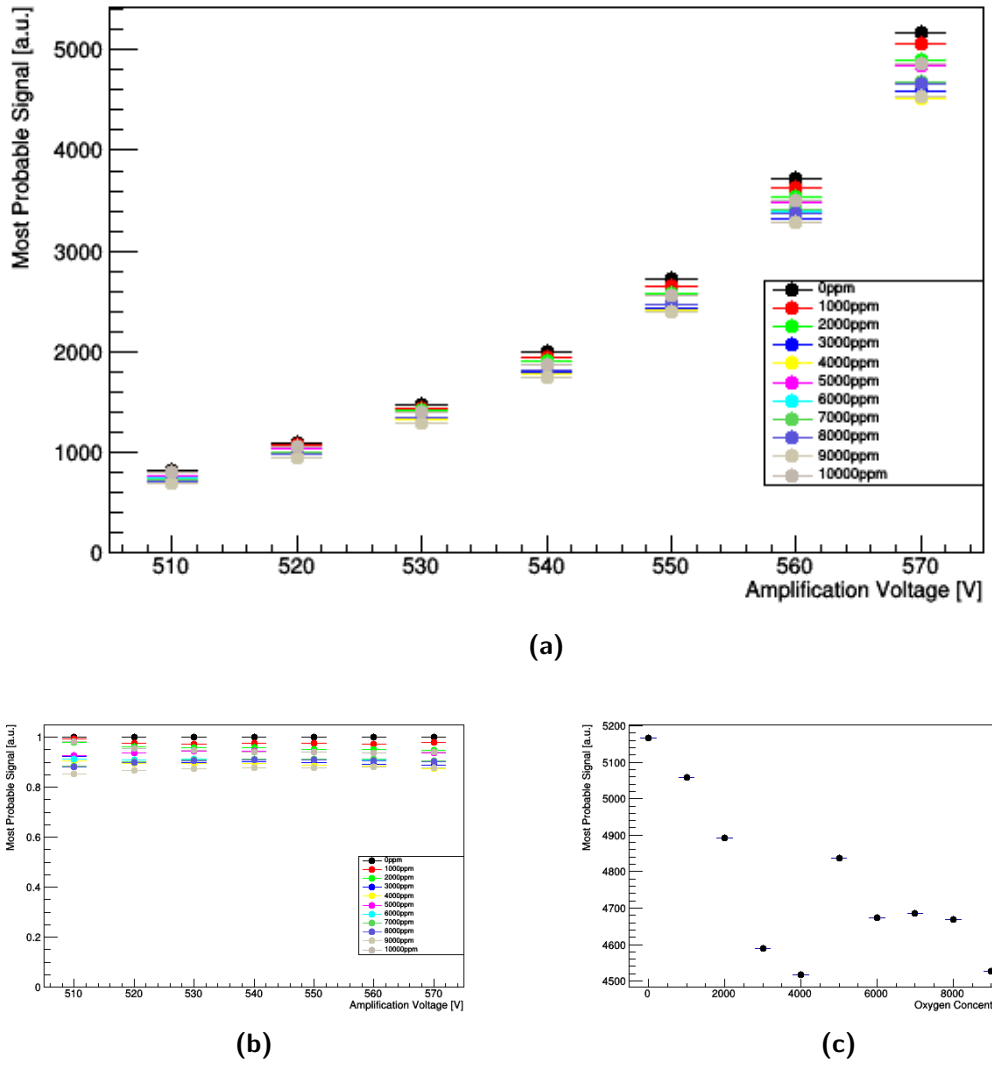

Figure 4.21.: (a) The photo peak position for different amplification voltages at a drift field of 600 V/cm at different concentrations of oxygen. (b) The same normalized to the value at 0 ppm oxygen. (c) The values at 570 V for different oxygen concentrations.

a time frame that is longer than the time it takes to take one drift plateau, as it could not be seen in the measurements there, see figure 4.22.

As one can see, the curves taken at one oxygen concentration seem to be stable, but the differences between the curves, which had to be taken on different days, are again in an order that would not be expected. A clear difference between the different contaminations is the drop of the left edge of the drift plateau, which

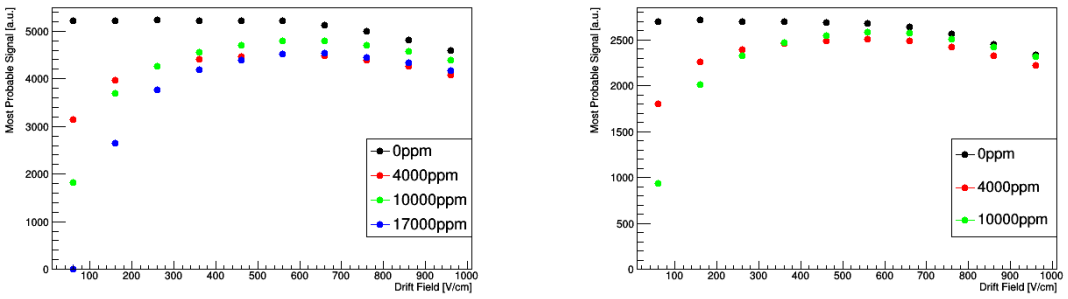

Figure 4.22.: Measurement of the drift plateau at (a) 570 V and (b) 550 V at different oxygen concentrations.

increases with increasing oxygen levels. The shape of the spectra for low drift fields, an example of which can be seen in figure 4.23, shows the same behaviour as seen in the simulation (see section 4.3), making fitting a meaningful gaussian there hard. This effect is only apparent for very low drift field at 60 V/cm and leads to an overestimation of the signal strength.

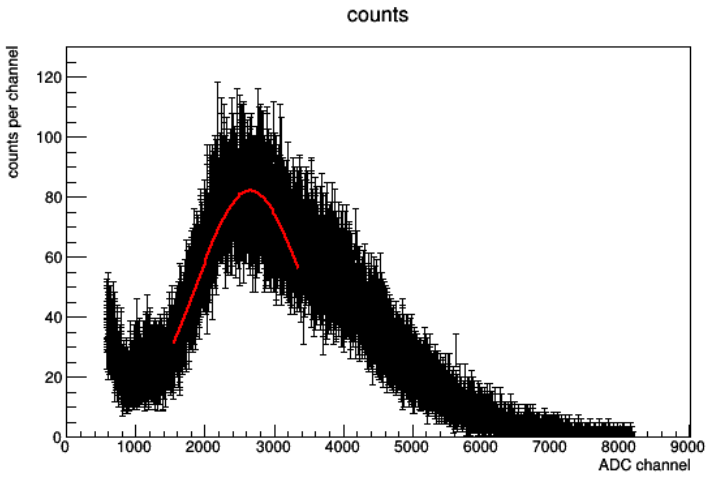

Figure 4.23.: Example of a fit at 570 V and a very low drift field of 60 V/cm at 10000 ppm of oxygen. The fitted peak is clearly shifted toward higher values.

To negate any long term effects, one can take one of the drift fields as fixed value and compare all other gains at the same oxygen level relative to this gain. This has been done in figure 4.24, taking the right edge of the plateau, at 660 V/cm as

fixed point. Taking 960 V/cm instead would have given very similar plots, as the mesh transparency would not depend on the oxygen concentration.

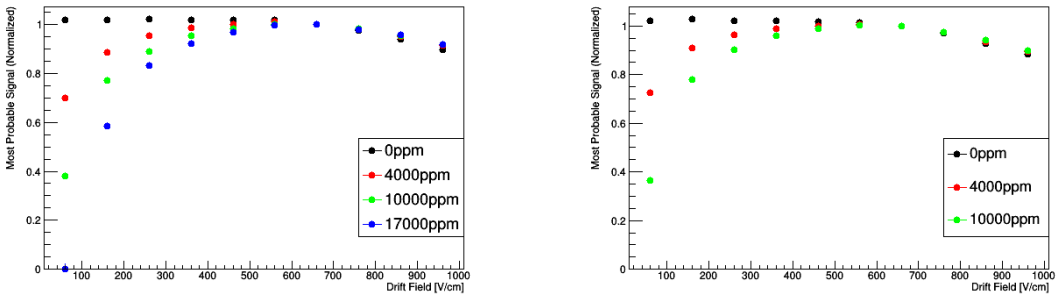

Figure 4.24.: Measurement of the drift plateau at (a) 570 V and (b) 550 V at different oxygen concentrations relative to the gain at 660 V/cm.

For both 570 V and 550 V, the emergence of the left edge of the plateau with increasing oxygen can clearly be seen. For very low drift fields, the detector loses around 70% or more of the signal strength, which is still an underestimation as can be seen from the fit. It seems to be largely independent of the amplification voltage, which confirms that the main mechanism for the loss arises before the amplification even takes place. Compared to the simulations in section 4.3, however, one sees that the effect expected from the simulation is not seen at the same drift field of 330 V/cm, but for lower fields. The most apparent reason is the geometry of the detector. The detector geometry in simulation and reality do not necesserily have to agree perfectly. If the drift gap in the real detector is smaller, this would shift the entire curve to the left.

To better understand the signal decay depending on the oxygen concentration, three points on this curve, 60 V/cm, 360 V/cm and 660 V/cm have been taken out to be measured again during one night at oxygen concentrations between 0 to 10000 ppm in steps of 1000 ppm. The measurements took place in one night, starting just after sundown at 10000 ppm and continuing to 0 ppm. This took longer than the night, which means the last two points had to be taken after sunrise. The results can be seen in figure 4.25.

All curves seem to exhibit the same behaviour for the different oxygen concentrations. The points were taken chronologically from the right, with conditions staying relatively similar for most of the night, before starting to fall just before sunrise (the coldest time of the night) and a subsequent stark rise after sunrise. The possible reasons for this will be investigated in section 4.4.4. To negate this effect, all measurements were normalized to the measurement at 660 V/cm at their

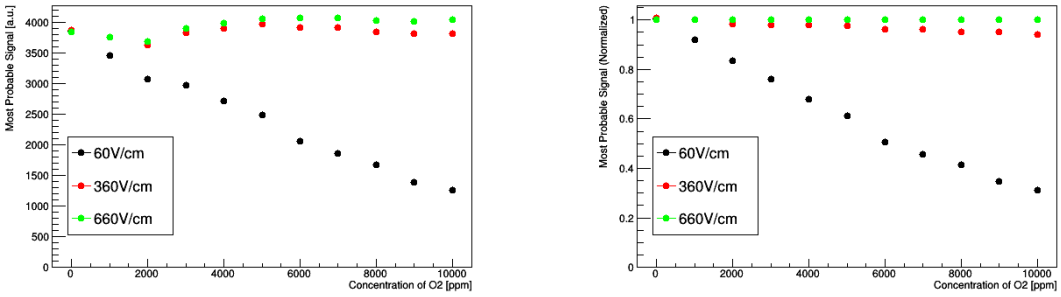

Figure 4.25.: Measurement of the oxygen dependence of the mean signal at 60 V/cm, 360 V/cm and 660 V/cm, (a) absolute and (b) normalized to the value at 660 V/cm.

respective oxygen levelsf, as they were taken in a narrow time window with only relatively minor changes in the environmental parameters. after doing this, the effect of oxygen on the mean signal is the same as was seen during the plateau measurements before. The signal also seems to be decaying linearly depending on the oxygen concentration, as was predicted by simulation.

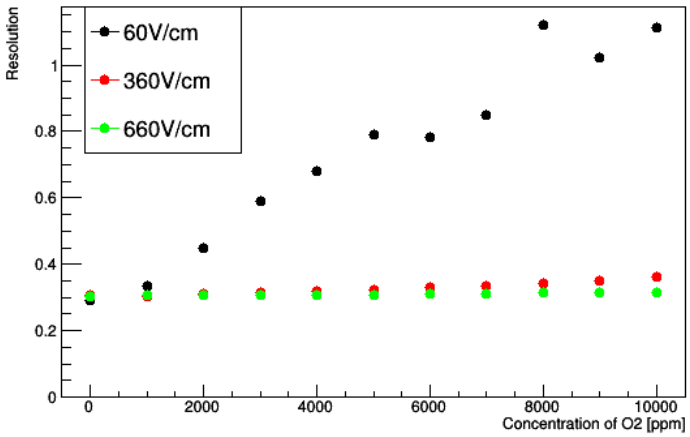

Figure 4.26.: Energy resolution of the detector at different drift fields as function of the oxygen concentration. The fit becomes unstable for 60 V/cm at above 5000 ppm as the spectrum becomes less gaussian, but the general trend can be observed.

The resolution, which is by its definition independent of any scaling, can also be investigated, seen in figure 4.26. The energy resolution of the detector decays

quickly for higher oxygen concentrations at low drift fields, as the stacking effect discussed in section 4.3 takes hold. This effect is not fully represented by the gaussian fit used to obtain the values and is therefore underestimated for very high concentrations. As one can see, at 5000 ppm the energy resolution is already above 1 for 60 V/cm. Both 360 V/cm and 660 V/cm are less affected, with the resolution only changing to 40% for 360 V/cm from 35% and no visible change for 660 V/cm.

4.4.4. Investigation into effects on the measurement stability

The first step of the investigation included understanding the role of the high-pass filters on the mesh voltage. The first effect was the emergence of permanent background could be seen at low amplitudes in the MCA, which could be removed by changing the shaping time of the amplifier above the frequency band of the noise. When using the source without any rate reduction, the high rate of photons caused the signals to stack on top of each other, causing a widening of the peak and a reduction of the effective amplification field. The charge up effect described earlier could be fully mitigated by reducing the rate of the source and removing the filter.

Some other effects still remained, however. The amplification of the detector depends on the density of the gas in the detector, which depends on pressure and temperature. While the pressure of the detector can be set in the gas system, the temperature of the gas inside the detector is not well known in the current system. Several of the components of the gas system, mainly the massflow controller, contain temperature probes. In addition, the gas system automatically logs temperature probes available, like the air temperature in the room. None of these changed significantly during the nights, however.

In the current system, there is no possibility to measure the temperature inside the detector. The only possibility to measure the gas temperature after the detector is to measure the temperature of the pipe using a temperature probe. This is done in front of the pressure controllers for the MDT and the Micromegas detector. The pipes do show a upwards change in temperature of around 0.6 K right around the dip in signal strength. Since the measurement is in front of the detector inlet, the temperature change inside the detector might be shifted significantly, especially since the gas needs to be exchanged before the new temperature is reached. As there is currently a new pressure vessel being designed, this shortcoming might be mitigated by adding a temperatue probe to the vessel, measuring the gas temperature directly, with no delays. This could help to ensure a stable gas density inside the detector and eliminate one source of variation in the signal strength.

5. Conclusions and Outlook for the Measurements of the Effect of Contaminations on Detector Performance

For this work, an augmented gas system has been designed and comissioned for the measuring room of the Würzburg experimental particle physics group. The system was setup to inroduce contaminations of oxygen and water in the range of ppm to 1% into the detector gas to study the effect of both on the detector performance. In addition to the comissioning of the gas system, new detectors and readout systems were setup in the scope of this work. This included two new resistive Micromegas detectors and two bulk Micromegas detectors. The systems are read out with SRS-based readout systems for the resistive Micromegas and MCA-based readout for both detectors.

To understand the effect of plastic piping as cause of contaminations and to test the gas systems, a study into different materials of piping and the influence of flow and pressure on the transport mechanism of both water and oxygen contaminations have been studied. The linear dependency of the contaminations on the length of the pipe and the inverse proportionality on the flow for oxygen could be confirmed. The results showed strong contrasts between different materials, showing that transport mechanisms for water and oxygen differ and the material of the piping should be chosen with the importance of the contaminations for stable detectors performance in mind. Some material in the study showed a good rejection of one contamination over the other, while one material showed a more universal rejection of both water and oxygen transfer, albeit to a lower degree.

Simulations into the mechanisms causing a loss of detector signal strength have been performed. It has been shown that one expects to find a loss of primary electrons at low drift fields. This loss depends exponentially on the distance the primary has to travel in the detector, meaning detectors that are constructed to have smaller drift distances are less susceptible to signal losses due to attachment of primaries to oxygen than ones with larger drift lengths. It has also been shown that the same effect of distance dependent loss will cause the usually gaussian

energy spectrum to broaden and distort the more oxygen is added, caused by different loss probabilities for primaries with different drift lengths.

The simulations have been followed up by measurements with the new gas system. For low drift fields, the energy spectrum shows the same broadening of the peak as seen in the simulation. While a pure Ar:CO_2 environment does only require very low drift fields to function, a gas containing high amounts of oxygen will have reduced potential as detector gas for low to medium drift fields. The loss in gain is around 70% at a drift field of 60 V/cm for 1% of oxygen, while they are around 40% for a drift field of 360 V/cm. The relative loss is only dependend on the drift field. This has been confirmed by measuring the drift plateaus at both 570 V and 550 V amplification voltage. In addition, the losses at both 60 V/cm and 360 V/cm show a linear behaviour with respect to the amount of oxygen introduced in the detector gas.

The Würzburg cosmic ray facility is also capable of measuring the effect of water as conaminant in the gas on the detector performance. Once the new box is comissioned, this investigation can be undertaken, as adding water contaminations relies on a stable temperature in the gas system.

Part III.

Production of Micromegas Detectors for the New Small Wheel of the ATLAS Detector

6. The ATLAS Detector

In the aftermaths of World War II, the European Nuclear Research Council (CERN-now called European Organization for Nuclear Research) was founded to create scientific cooperation between former enemies and focus European research efforts in nuclear and particle physics. Part of the program of CERN has been high energy physics at accelerators. The first accelerator built at CERN was the Synchrocyclotron (SC), with a maximum particle energy of 600 MeV. It closed down after 33 years in service. Most of the other accelerators at CERN serve as pre-accelerators for new, higher energy accelerators. The Proton Syncrotron (PS) was built in 1959 and produced proton beams of 28 GeV energy. Nowadays, the PS feeds particles to the Super Proton Synchrotron (SPS), built in 1976, which then accelerates the beams to 450 GeV. The newest accelerator, the Large Hadron Collider (LHC), has been built inside the tunnel that housed the Large Electron Positron (LEP) accelerator. The LEP, which has been used to find the experimental verification of the existence of the Z-boson, accelerated electrons and positrons up to a center of mass energy of 209 GeV and was shut down to make place for the LHC in 2000. A schematic view of the LHC accelerator chain can be seen in figure 6.1.

The LHC is used for a broad spectrum of physics programs, from the search for new particles over dark matter to supersymmetry and more, in proton proton collisions of up to 14 TeV design energy. After its first start up in 2008, the energy of the accelerator was first set to 8 TeV, which was enough already to lead to the discovery of the Higgs-boson. In 2012 the energy was increased to 13 TeV. Four main experiments are located on the LHC. ATLAS and CMS are both designed as multi-purpose systems with a focus on a broad physics program. The LHCb detector is especially focused on the investigation of B-mesons and their decay chains. Besides protons, the LHC can also accelerate heavy ions, which create quark-gluon plasma on collision. ALICE, the fourth detector, is dedicated to research in the field of these plasmas.

To increase the luminosity of the detector and thereby the amount of interesting proton-proton collisions that can be recorded during its lifetime, the LHCis also part of an extensive upgrade program. The most important step of upgrades is the upgrade to the high-luminosity LHC, which will increase the collision rates in the detector generating 250 fb^{-1} of data per year, compared to the 66 fb^{-1} taken by the ATLAS detector in 2018.

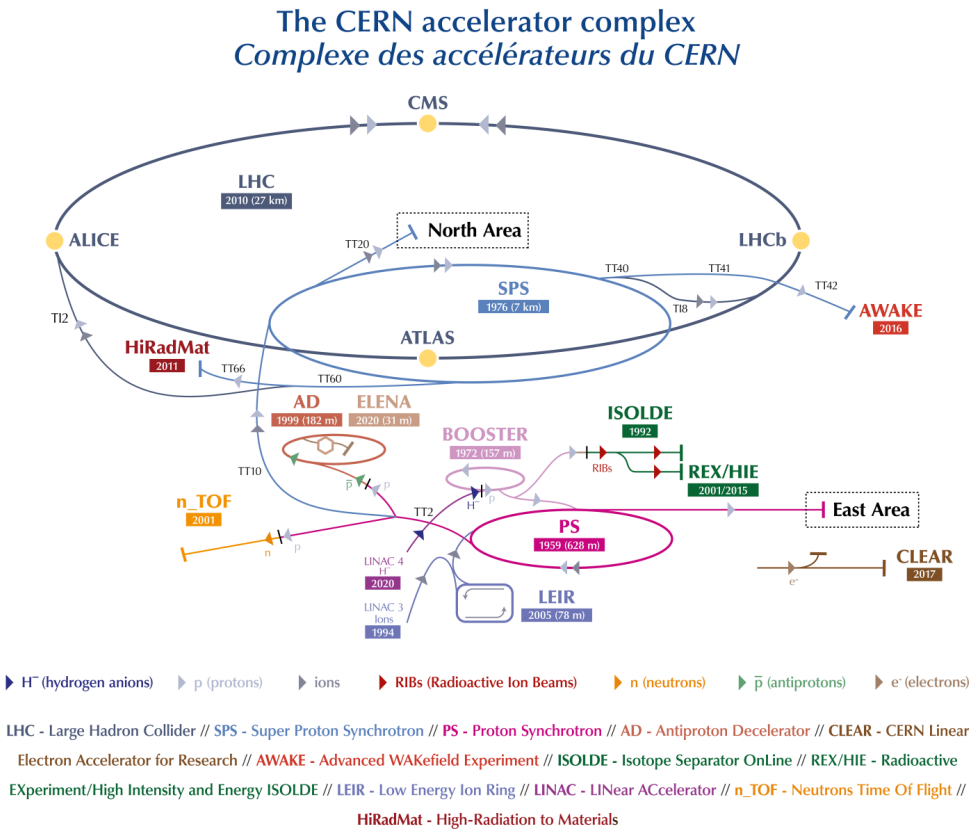

Figure 6.1.: Schematic view of the accelerators currently active at CERN, from [87]

The A Toroidal Lhc AparatuS (ATLAS) detector was designed as a multi-purpose detector system for the LHC. The system is designed to cover as large of a solid angle range as possible, being cylinder symmetrical around the beam pipe and forward-backward symmetric. As multi-purpose system, it has to be able to accurately measure different types of particles to allow for analyses of very different physics processes. The subsystem solely dedicated to muons is of special interest in this work. First, the current muon system, the Muon Spectrometer, will be explained, followed by a description of its upgrade to the small wheel, the so called *New Small Wheel* (NSW). To provide an orientation in the detector system, the universal coordinate system for the detector is given here.

The ATLAS Coordinate System The ATLAS coordinate system is a right-handed system placed in the geometric center of the detector. The positive x-axis points towards the center of the LHC-ring and the positive y-axis is pointing up-

wards. To ensure a right handed coordinate system, the z-axis therefore has to point anti-clockwise along the beam pipe when seen from above. Due to the fact that the detector is cylindrical, it makes sense to also define the corresponding cylindrical coordinate system. The coordinates in the x-y-plane, also called *transverse plane*, can therefore be expressed in terms of r-φ-coordinates, leaving the z-axis the same. The azimuthal angle φ is measured against the positive x-axis. In physics analyses, a spherical coodinate system around the recorded interaction point is used. It uses the same r-φ-plane as the cylindrical system, but replaces the z-axis with the polar angle θ, which is measured against the positive z-axis. Since the center of mass system in parton-parton-collisions can exhibit substantial amounts of momentum along thebeam (z-axis) direction, θ is not suitable to describe the system due to its lack of Lorentz-invariance. Hence, θ is replaced by the so called *pseudorapidity* η:

$$\eta = -\ln\left(\tan\left(\frac{\theta}{2}\right)\right) \tag{6.1}$$

In the case of massless (or close to massless) particles, this is equivalent to the relativistic particle's rapidity y

$$y = \frac{1}{2}\ln\left(\frac{E + p_z}{E - p_z}\right), \tag{6.2}$$

where $E = \sqrt{|\vec{p}|^2 + M^2}$ denotes the energy of a particle of mass M travelling with momentum $\vec{p}$. p_z is the corresponding z-component. Differences of the pseudorapidity are Lorentz-invariant, allowing for a description of the system that does not depend on the chosen coordinate system.

6.1. The ATLAS muon system

Muons are used in many different physics analyses. From measurements of the mass and properties of the W-boson and properties of the Z-boson, over the discovery of the Higgs-boson and the subsequent measurements to investigations the of possible dark matter candidates, unknown particles or supersymmetry. One of the two main channels investigated during the discovery of the Higgs-boson was the four lepton $H \to ZZ \to 4\ell$ channel[88]. The Feynman graph and a graph of the four lepton mass spectrum showing the Higgs-peak is shown in figure 6.2. To be able to make such discoveries and to subsequently determine the properties of the particle, the resulting leptons, including muons, have to be measured as precisely as possible and in as high a kinematic range as possible. Due to the higher flux

of particles in the inner detector resulting from the high-luminosity LHC upgrade, which makes reconstruction of hadronic particles much harder, the analyses based on leptonic final states will become more important in the future. To succesfully continue the physics program, the precise determination of muon momenta even in the high η region is therefore vital. Especially in the new environment after the high luminosity upgrade, the current detector would not be able to trigger the readout with muons in this region, a problem that would be very much of disadvantage in future analyses. As such, the upgrade program of the muon system is coupled to the upgrade of the LHC and the changing conditions in the detector coming with it. This section serves as explanation of the current system and will in the end focus on the upgrade to the inner muon end-cap station, the New Small Wheel.

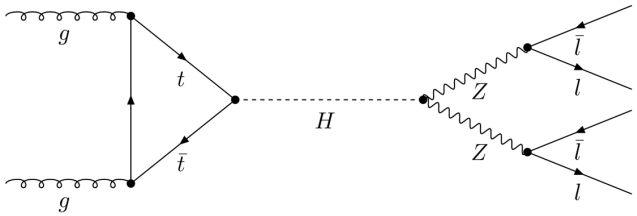

(a)

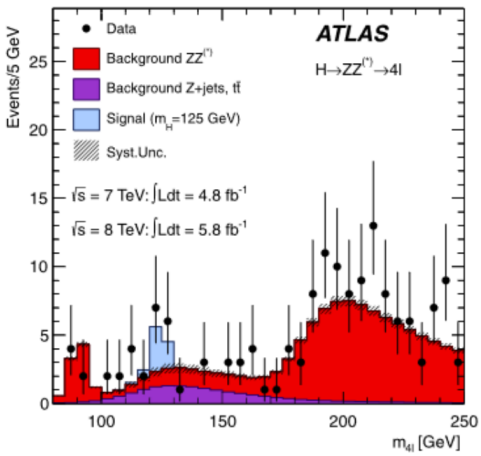

(b)

Figure 6.2.: (a) Feynman graph of the Higgs to four lepton channel, (b) graph of the four lepton mass showing the first sign of the Higgs-peak, from [88]

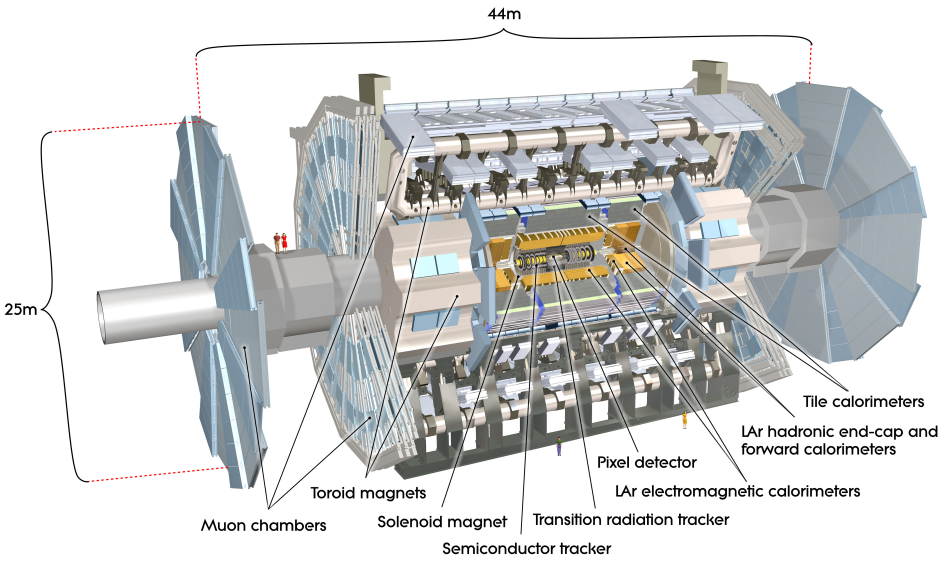

Figure 6.3.: Schematic view of the ATLAS detector. Subsystems are labelled, provided by [90]

Since muons do not lose much energy per distance when interacting with matter, they can pass through all layers of the detector, while other particles get stopped part way through (see chapter 2). Therefore, the muon system constitutes the outermost layers of the ATLAS detector. As the muon system needs to cover much more volume than the other subsystems, it makes sense to use detector technologies that can cover large volumes at comparatively low costs and material budgets. In the ATLAS detector, the muon system therefore uses gaseous detector technologies. A schematic view of the entire detector can be seen in figure 6.3. As mentioned before, the detector is cylindrical. Like a barrel, the detector can be split into three regions. The wall of the barrel, called *barrel region*, and the two *end-caps*, like lids on the barrel. These regions are split in 3 layers, called inner, middle and outer layer. The detectors used in each region will be explained in the following sections. A fully detailed description can be found in [89].

6.1.1. Barrel Region

The magnetic field troughout the barrel region is provided by a toroid containing eight coils arranged in a concentric circle around the beam pipe. The muon detector is therefore naturally divided into 16 sectors, half between the coils (large sectors) and the other half in the area containing the coils (small sectors). The sectors cover around 29° and 20° for large and small sectors, respectively, and

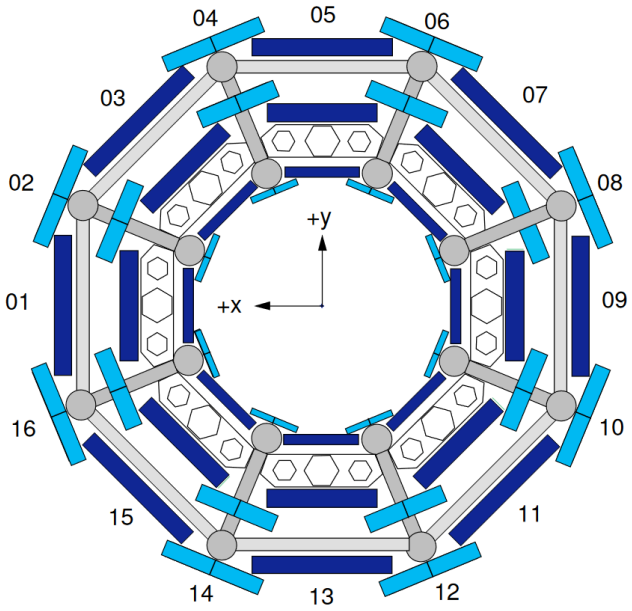

Figure 6.4.: Schematic view of the ATLAS barrel muon system in the transverse plane, including the sector labels. The large sectors are darker, the small sectors are light blue, with the dark grey toroid magnets in the center, from [91]

overlap with their neighbors by around 2°. A cross-section of the muon system indicating the sectors and their labelling can be seen in figure 6.4. The toroid magnets generate a magnetic field in the negative φ direction.

The barrel chambers form concentric cylinders aroud the beam pipe. The radii of the three cylinders are 5, 7.5 and 10 m. They have a length of around 13.0/18.2/24.6 m and 14.4/20.6/25.4 m for the large and small sectors, respectively. Due to the distance from the interaction point, the barrel muon systems only cover a range of $|\eta| < 1$. To allow for cabeling into the central detector, a small hole had to be left at $|\eta| = 0$. Radially, The inner cylinder contains two detector modules of four layers each and the middle and outer cylinders contain two detector modules of three layers each. Each station contains a Monitored Drift Tube (MDT)[92] chamber for accurate tracking in the transverse plane, with the tubes aligned along the beam pipe. Triggering is enabled by three stations of Resistive Plate Chambers (RPC)[93]. They are put on the side of the middle MDT-station facing the interaction point and the one facing away from it each and one more on one side of the outer MDT-station.

Monitored Drift Tubes The MDT-chambers contain a spacer frame on which multiple rows of drift tubes are glued. The drift tubes form four layers for the

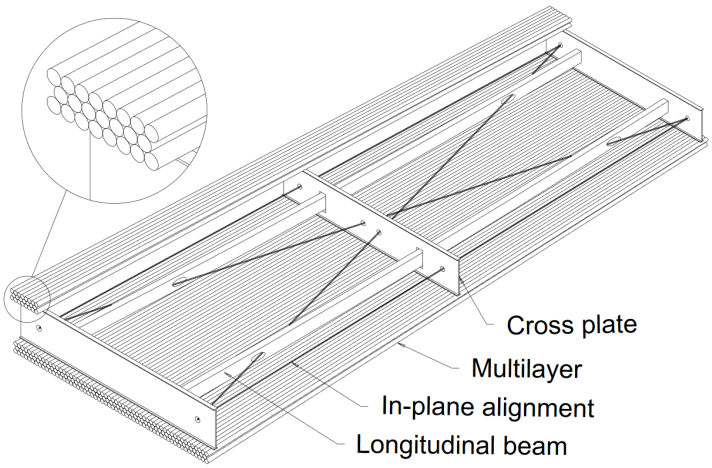

Figure 6.5.: Schematic view of an ATLAS MDT, some of the tubes are cut away so the underlying support structure can be seen, from [89]

inner and three layers for the middle and outer stations on each side of the spacer structure. Each tube has an outer diameter of 30 mm with 50 µm diameter wires in the center. A total of 37200 tube have been built, with a total volume of 800m^3. The electronics, containing a signal preamplifier and a time to digital converter are mounted directly on one end of the tubes. A schematic view of an MDT module can be seen in figure 6.5.

Resistive Plate Chambers Resistive Plate Chambers(RPC) are a very simple detector type: two bakelite plates are separated by spacers of 2 mm thickness. On the surfaces of these plates that are facing away from the gas gap between them, a graphite layer is painted, which is connected to a high voltage source. On top of this graphite paint, an insulating layer is glued and readout strips are added on this layer. The strips on opposite sides are orthogonal to each other. Two of these detectors layers are placed onto one main support structure. The main support structure is 50 mm thick. The entire structure is 99 mm thick. The main support structure is 130 mm shorter than the RPCs, allowing the modules to overlap in the z-direction by flipping the side on which the main support is located. Depending on the position, a module can be between 62 cm and 103 cm wide and between 3.3 m to 5.2 m long. A schematic cross section of the RPC can be seen in figure 6.6.

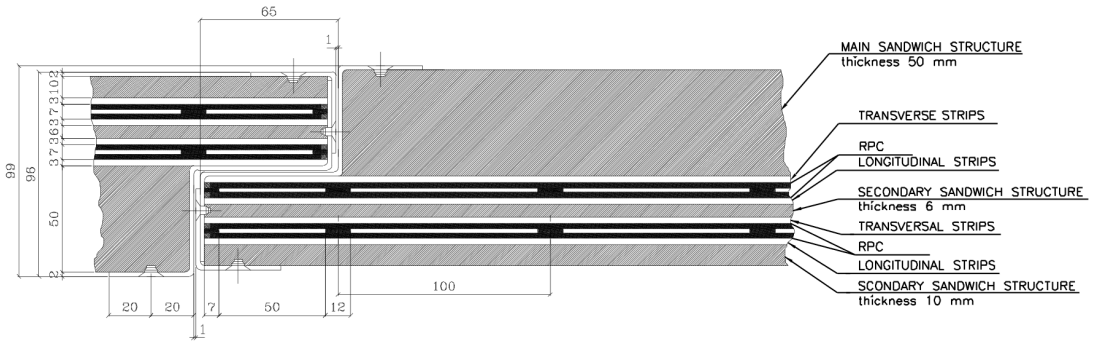

Figure 6.6.: Schematic cross section of the ATLAS RPC, with an illustration of the overlap created by flipping the panels, from [89]

6.1.2. End-Caps

The End-Caps are designed to cover a range of $1 < |\eta| < 2.7$ and follow the sector definition of the barrel region. Eight of the 16 sectors, the small sectors, cover the azimuthal area around the barrel toroids, while the other eight cover the area inbetween. Contrary to the barrel region, the end-caps contain four stations at 7.5, 10, 14 and 21-23 m from the interaction point along the beam axis, labeled Inner (I), Extra (E), Middle (M) and Outer (O) stations, respectively. Each of the stations is divided into two radial regions, a forward (F) in the center and an end-cap (E) in the outer circle. An overview of the stations in the end-cap region can be seen in figure 6.7.

For triggering of collision events, Thin Gap Chambers (TGC) are used. They are exclusively placed in the middle station. One triple gap TGC-layer is placed in front of the MDT-layer and one double gap TGC-layer is placed behind. With the exception of the inner most station, which will be discussed separately, all other stations exclusively use MDT-chambers for tracking. The chambers are aligned radially in the x-y-plane. The tubes in these trapezoidal chambers are aligned to be parallel to the parallel sides of the trapezoid. The chambers are constructed in such a way that the active area of chambers in different sectors overlap with each other, avoiding holes in the determination of a charged particle track. An example of the overlap for the EM (End-Cap Middle) and FM (Forward Middle) stations can be seen in figure 6.8.

Thin Gap Chambers The TGCs are similar to a multiwire proportional chamber, but the gap is smaller than the pitch between the wires. The TGCs used in the end-caps are using a pitch of 1.8 mm and a gap size of 2.8 mm at 50 µm wire diameter. The graphite cathodes are deposited on G-10 plates, a pressed fibreglass

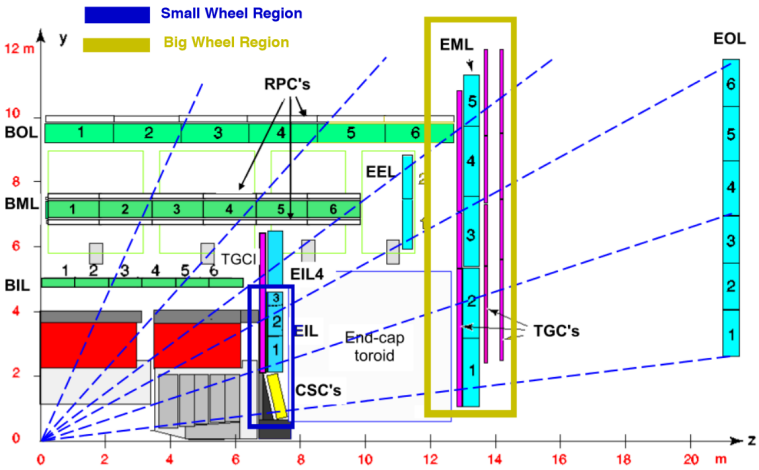

Figure 6.7.: Schematic side view of the ATLAS muon system in the y-z-plane, the origin of the coordinate frame is located in the interaction point. The red and gray parts at $x < 6$ m and $y < 4$ m are part of the calorimeter, from [91]

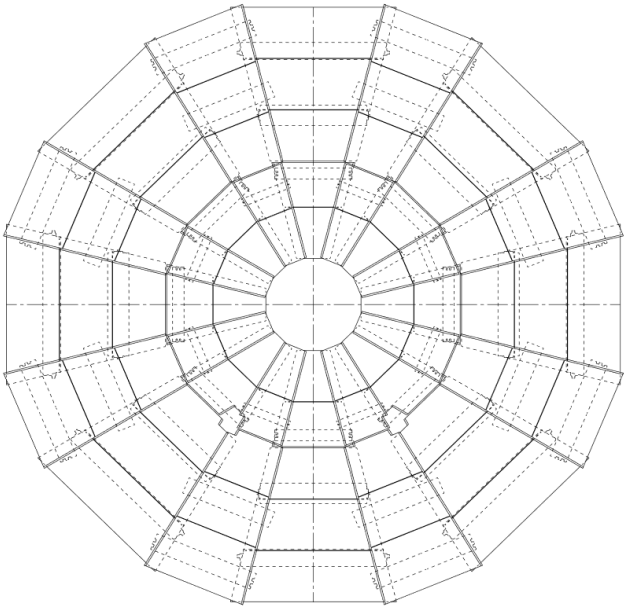

Figure 6.8.: Schematic view of the ATLAS wheel stations, indicating the overlap of the detector modules to ensure full coverage, the z-axis is perpendicular to the schematic and located in the center, from [89]

board, with copper readout strips of width between 14.6 and 49.1 mm, providing azimuthal resolution, which are reinforced with 5 mm thick paper honeycomb structures on the outside. The G-10 plates of the inner cathodes are glued on either side of a 10mm paper honeycomb structure. These layers are then stacked to form the detector with either two or three layers. In the central layer of a three-layered TGC, the copper does not have strips. Depending on the range of pseudorapidity, four to 20 wires are combined into one readout channel and fed to the readout boards at the border of the detector to form a trigger signal. The same readout can then be used for the strips. Due to the comparatively small distances, the signal is fast, allowing the chambers to be used for triggering.

6.1.3. The Small Wheel

The inner station (I), called *Small wheel*, is sandwiched between the calorimeter and the end-cap toroid magnet, see figure 6.7. As with the other end-cap stations, the Small Wheel is segmented into 16 sectors. Due to its proximity to the interaction point and the high pseudorapidity range it operates in, a special absorber shield is placed in front of the wheel to suppress the flux of hadronic particles that are missed by the calorimeters and magnet due to their excessively high η. Even with the absorber shield, the Small Wheel has to fullfill special conditions on dead time and radiation hardness. For the highest ranges of η, these conditions are not fullfilled by regular MDT-chambers. As such, the chambers closest to the interaction point, in the FI stations, are using a different detector technology, the Cathode Strip Chamber (CSC), since it has a higher rate capability of 1000 Hz/cm^2, compared to 150 Hz/cm^2 for MDTs.

Cathode Strip Chambers The Cathode Strip Chambers are proportional wire chambers with a cathode strip readout in which the distance between the cathode and the wire plane is equal to the pitch of the wires. In this case, the wire pitch is 2.54 mm and the distance between the cathode boards is 5.08 mm, while the wire diameter is 30 µm. The wires in this setup are oriented in the radial direction, while the strips are orthogonal, in azimuthal direction. Only every third of the strips with 1.5 mm width and a pitch of 1.75 mm is connected to readout, taking up the signal of neighbouring strip via induction. This leads to an effective readout pitch of the order of 5 mm. There are 32 Cathode Strip Chambers with four layers of independent detectors each, aranged into stacks of two per sector. They cover an area of around 65 m^2 with at total of more than 10000 wires and almost 80000 strips employed.

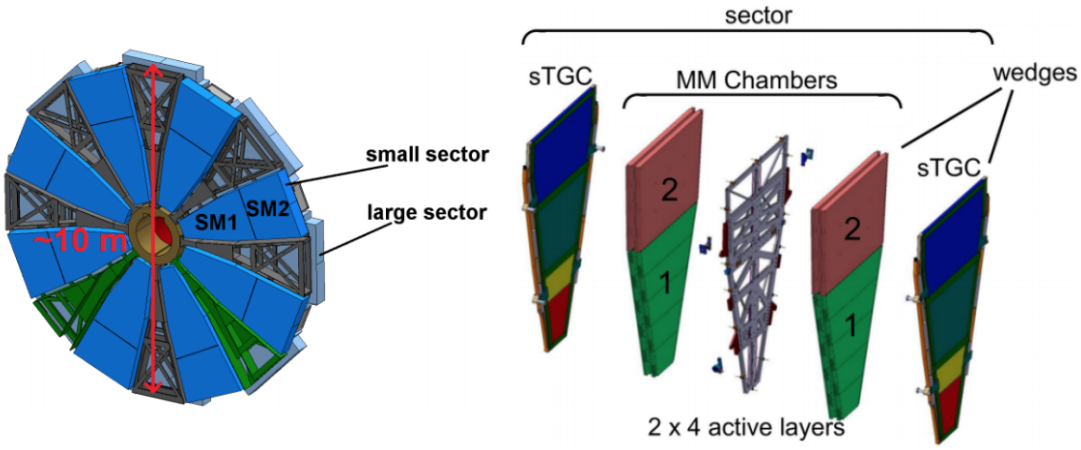

Figure 6.9.: Schematic view of the ATLAS NSW, with marked sectors and blowup of a sector, indicating the numbering scheme of the modules in one wedge and the order of wedges on the support structure, from [94]

6.2. The New Small Wheel and Trigger Upgrade

To prepare for the new high-luminosity environment after Phase-I upgrade of the LHC, the two Small Wheels have to be replaced. The New Small Wheel project was envisioned to cope with the high background radiation region (up to 15 kHz/cm^2)[91]. The general structure is similar to the Small Wheels, keeping the 16 sector structure coming from the barrel region, see figure 6.4. These sectors are sub-divided into smaller units.

- **Sector:** Sectors come in two types: large and small. On each wheel, there are 8 sectors of each type. Each sector contains two wedges of both detector technologies.
- **Wedge:** An Assembly of detectors covering an entire sector in the r-φ-plane, containing one detector technology. Two wedges of Micromegas that have already been put onto the support structure are usually called a double-wedge.
- **Module (or sometimes Quadruplet):** A single independent unit, a quadruplet of four detector planes.
- **Plane:** One functional layer of a detector module with one readout plane, not an independent structural unit.

As with the Small Wheel, the NSW is located between the end-cap calorimeter and the end-cap toroid magnet, covering a range of $1.3 \leq |\eta| \leq 2.7$. Due to the

changes in the available space, a new shielding around the beam pipe has been developed to prevent the ehanced background of high energy hadrons reaching the detector, once the high-luminosity LHC upgrade has been completed. The shielding was desinged using simulations[57]. On this shielding, the new mechanical support structure is mounted. It consists of a cylindrical hub structure with spokes going radially outwards, on which the sectors will be mounted, with the small sectors facing the interaction point. Sectors will be assembled fully before getting mounted on the NSW support structure. A schematic view of the NSW, the position of the sectors and a blowup of one sector can be seen in figure 6.9. Two different detector technologies are used. The sTGCs used primarily for triggering and the Micromegas detectors primarily for tracking. To cope with higher particle rates and radiation levels, new electronics has been developed for the control and readout of the new detectors.

6.2.1. sTGCs

Small strip Thin Gap Chambers, sTGCs, are a developement of the TGCs used in the wheels already. Their physical parameters are the same as the TGCs, but the strips on the sTGCs have a much smaller pitch of 3.2 mm instead of up to 50 mm on the old TGCs. They consist of an array of gold-plated tungsten wires of 50 μm diameter with a pitch of 1.8 mm in the center of two cathodes which are 2.8 mm apart, the same as the TGC that have already been developed for the ATLAS detector. The readout structures are similar to the previously discussed resistive readouts for micromegas detectors in section 2.2.1, with pads on one side and strips on the other side, from which the detectors get their name. These are then covered by a resisitive layer of carbon, protecting the cathodes from sparking and making it safer in the high rate environment. A schematic view of one detector layer, of which each module has four, can be seen in figure 6.10. Each sTGC wedge consists of three different modules.

6.2.2. Micromegas

The basic working principle of Micromegas has been discussed in 2.2.1. The modules are used because of their low dead time compared to MDT and their comparable precision, which allows for a better muon energy measurement. In the NSW, the Microegas modules are primarily used for precision tracking. Each of the layers in one module is 5.2 mm wide and contains (as a primary choice) a mixture of argon and carbon dioxide in the ratio 93:7 at ambient temperature and an over pressure of around 10 mbar. The readout is designed to deliver a precision of the order of 100 μm in the radial (η) direction, while the precision in the azimuthal (φ) direction is around 3 mm. To achieve this, the readout strips are

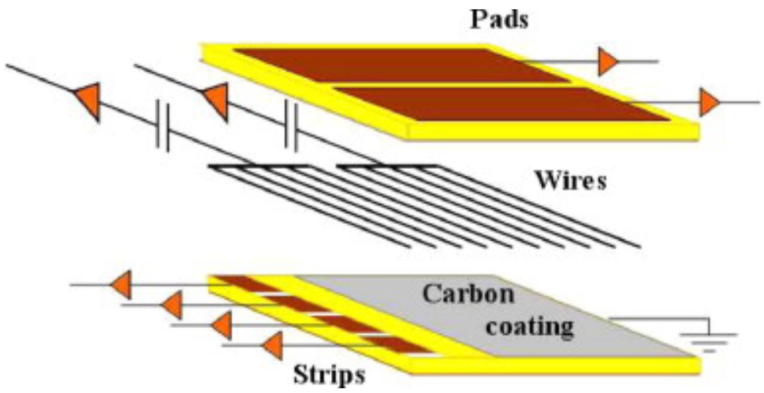

Figure 6.10.: Schematic view of the NSW sTGC layers, from [91]

arranged pointing along the azimuthal direction with a pitch of 425 µm for the small sector and 450 µm for the large sector. The strips are covered by a resistive layer of carbon in strips parallel to the copper strips of the readout. The design resistivity of these strips is 10 MΩ/cm. On top of this layer, pyralux pillars with a nominal height of 122 µm are added. These ensure that the 30-71 mesh used in the detectors maintain the amplification gap. Each wedge is divided radially into two modules with four layers each. They share common attributes. A closer discussion of the second module of the small sector (SM2) can be found in section 7.1.

6.2.3. Electronics

The readout electronics for the NSW are customized Application Specific Integrated Circuits (ASIC) using the IBM 130 nm process to reach sufficient radiation hardness, the so called *VMM*[95]. Several of these ASICs can be put onto one Front-End Board (FEB). The micromegas detectors use 8 VMMs connected to up to 512 strips on one *MMFE8* FEB. The sTGCs use two different FEBs: The strips are read out using 8 VMMs on a s(trip)FEB connected to 448 strips, while the pads get read out by p(ad)FEBs, comprised of 2 VMMs to read 104 pads and one VMM connected to the sTGC wires. An overview of the trigger and data acquisition can be seen in figure 6.11. In addition to trigger and data aquisiton systems, the FEBs contain the Slow Control Adapter (SCA), which is used to configure the detector electronics and provide status information to the Detector Control System (DCS), the central control system of the ATLAS detector. A total of 4096 FEBs are used for the Micromegas detectors, while 1536 FEBs will be used for the sTGCs, allowing for the readout of more than two million strips in the Micromegas and around 354 thousand sTGC channels. Since the confined space of operation

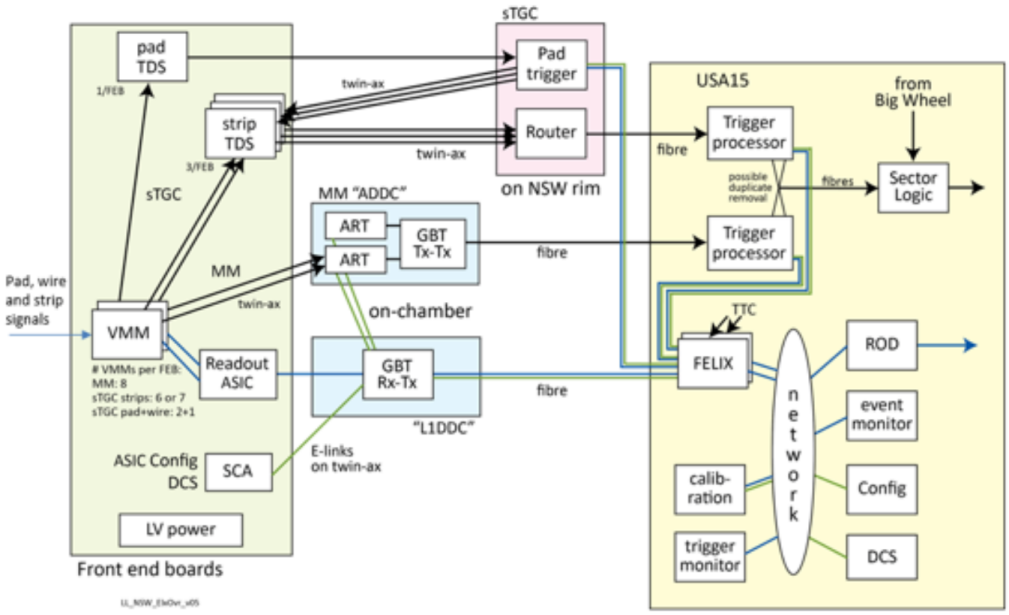

Figure 6.11.: Schematic of the ATLAS NSW trigger system, from [96]

of the electronic is not enough to allow air cooling, water cooling pads have been designed.

VMM The VMM features a charge amplifier with selectable polarity and gains between 0.5-9.0 mV/fC at low noise. It also provides a shaping feature with time constants of 25, 50, 100, or 200 ns, including discriminators for up to 64 channels. It can measure and digitize signal peak height, the time to peak or time over threshold with respect to an external clock, like the ATLAS bunch crossing clock. While the output is buffered, the first hit over threshold is transmitted to contribute to the trigger decision.

Trigger The purpose of the trigger is to identify those collision events that show interesting features like high energy particles, trigger the readout for those events and discard all events that do not show any such features. This reduces the rate of data collected to a managable amount. For an effective trigger, the relevant detector data needs to be read out as quickly as possible. To this end, special readout ASICs have been designed. These ASICs constitute an entire chain from on-detector electronics up to the central trigger electronics, where the data of the entire system is collected to make the decision to trigger the readout of the event. The trigger is split into several levels, where first so called *regions of interest*, i.e. regions of the detector that might contain signals of high energy particles, are

identified. For these regions, the detector systems are read out and a decision is made based on this data. In the following, the trigger chains will be described in more detail for both detector technologies used in the NSW.

The Micromegas VMMs transmit the address of the first hit in the buffer immediately. This so-called *Address in Real-Time* (ART) is transmitted to a dedicated ASIC, which then combines the first hits of 32 VMMs into an array and adds additional information, like the strip number and a code indicating the position of the detector area covered by the VMM, before it is transmitted from the ART Data Driver Card (ADDC) to the Micromegas Trigger Processor using Gigabit Transceiver links.

For the sTGCs, the VMMs send their trigger signal to the pad or strip Trigger Data Serializers (pTDS or sTDS), which are directly located on the corresponding pFEBs or sFEBs. The trigger data is rearranged and then send to the rim of the wheel, where electronics for the Level 0 trigger apply a 3-out-of-4 coincidence filter on the pads. The strips that are below the pads that have fired are then taken for the L1 decision and if positive, the trigger data of both detectors is then merged using an FPGA module and sent to the Front-End Link Interface eXchange (FELIX)[97] and the ATLAS muon system sector logic, where the trigger data is then combined with that of the other End-Cap Muon stations to make the final trigger decision. 512 L1DDCs will be used for each the Micromegas and the sTGC data aquisition, while 32 L1DDCs will be used in the sTGC trigger path. 512 ADDCs will be used in the Micromegas trigger.

Data Acquisiton Up to eight VMMs send their data to the Read-Out Controller (ROC)[98], an ASIC that is placed on the same FEB, after the L1 (or L0 after the Phase-II Trigger Upgrade) has been triggered. The data is rearranged and transmitted to the Level 1 Data Driver Card (L1DDC)[99] and from there to FELIX where the data is then built into an event.

7. Production of Micromegas for the ATLAS New Small Wheel

The New Small Wheel is built in a collaborative effort of universities and institutes around the globe. Two different detector technologies are used (see chapter 6). The Micromegas detectors are built in Europe. There are four different modules, described as Large/Small module and a number, 1 for the inner part and 2 for the outer part. All of the Small Modules 2 (SM2) were built in Germany by the universities of Freiburg, Würzburg, Mainz and the LMU Munich. In this chapter, the structure of the SM2 is described more closely, followed by the setup of the production line in Würzburg, including all production steps taking place in Würzburg.

7.1. The Small Module 2

The Small Module 2 (SM2) is one of the four different Micromegas modules built for the NSW. Each of the sector types, small and large is divided into two modules, counted from the inside. Therefore, the SM2 is the outer module of the small sectors. A picture of the modules can be seen in figure 7.1. They mostly differ in their dimensions and some minor details. As such, this chapter can serve as a general description for all modules, while discussing the SM2 in more detail.

7.1.1. Structure of the SM2

Every module contains four detector layers consisting of five decetor panels of Micromegas. The working principle of these detectors is described in section 2.2.1. The layers of one quadruplet, i.e. a four layer detector module, are arranged to minimize the amount of panels needed to create them. The layers are arranged in alternating orientations, with the single-sided drift panels serving as the outside. The readout boards are double-sided, with one containing readout strips parallel to the sides, called the eta layer, while the stereo readout board has strips that are tilted by $\pm 1.5°$ with respect to the eta layer. The readout boards are pushed against the drift panels such that the mesh on the drift panel gets pushed against the pillars on the readout boards. Between the two readout panels sits a

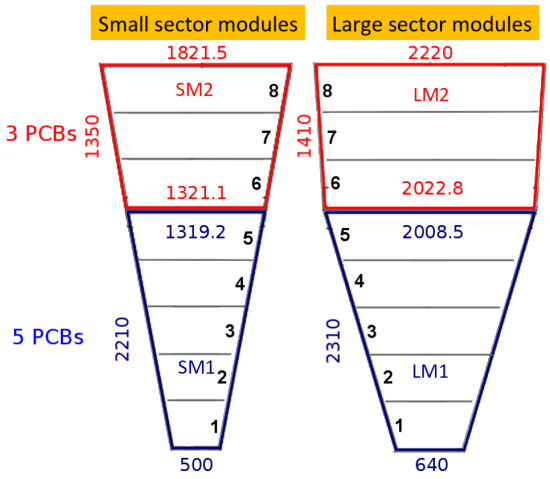

Figure 7.1.: Schematic view of all four different modules. The different readout PCBs are numbered inside the modules and panel dimension are given in mm, from [100]

double-sided drift panel. The correct alignment between the panels is ensured by alignment pins at the corners of the boards. One module is 70 mm thick in total. The gas gaps are are tightened by using an o-ring that is guided by metal bars around the outer perimeter of the module. Each drift panel contains two gas inlets on each corner of the longer of the parallel sides and outlets on the corners of the shorter of the parallel sides. A schematic drawing of the module structure can be seen in figure 7.2. When under pressure, large detectors will start to bulge. The resulting deformities, for example of the readout strips, could reduce the spatial resolution. To prevent this, bars are screwed through the panel. For the SM2, this is done at 6 positions. To prevent leaks, pyralux domes are glued onto the panels at the hole positions, which close the gas volumes when pushed against each other.

7.1.2. Readout Boards

The readout boards are double sided. The core of the boards contains a 10 mm thick aluminum honeycomb structure and aluminum bars that form a frame around the honeycomb structure onto which the already milled and drilled readout PCBs get glued. To ensure that the panel is as planar as possible, the PCBs are placed onto a vacuum table made from granite with a planarity of 10 µm. The PCBs of the second side get glued at the same time, using a stiffback structure that can be put on top of the panel. Distance pieces ensure an even thickness, while the horizontal alignment is guaranteed by dowel pins that fit into holes drilled into the readout PCBs. A picture of this process can be seen in figure 7.3.

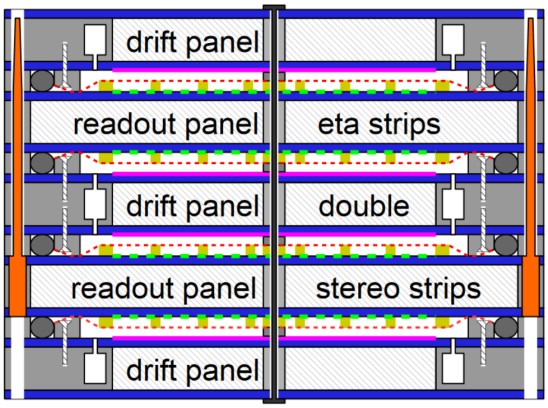

Figure 7.2.: Schematic view of the module with the drift-readout-drift-readout-drift sandwich structure. The five panels are aligned by the pins pictured in red, the black bar in the center is one of the screws to keep the panel from bulging outwards, from [100]

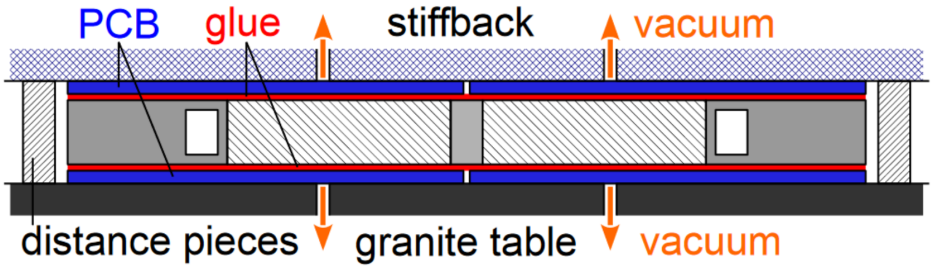

Figure 7.3.: Schematic view of the stiffback procedure for readout board production, from [100]

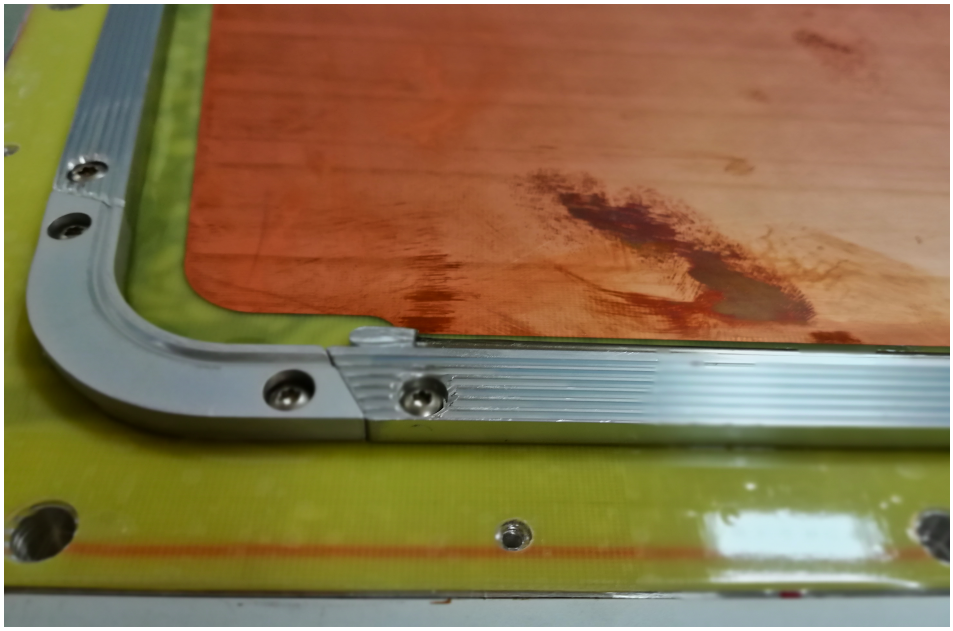

Figure 7.4.: Picture of the corner of the drift panel. The mesh-bar is slanted to the outside and contains grooves. It is glued onto the panel, while the screws ensure electric contact to the panel structure. The pipe next to the bar is connected to the gas outlets. The reddish surface is the cathode.

7.1.3. Drift Panels

The drift panels are constructed similarly to the readout boards. Instead of readout PCBs, the side of the drift panel facing the inside of the detector (or both sides for double-sided panels) are covered by PCBs with large copper surfaces, while the outside surfaces are covered by blank PCBs. Connectors for the drift cathodes are placed at one of the slanted sides of the panel (or both for the double sided panel), while the gas connections are on each corner. The ones at the larger of the parallel sides serve as inflows, while the ones on the shorter side serve as outflows. The gas connectors are internally connected to a piece of pipe running along the mesh bar. Several small holes are put into this pipe, causing a lateral and even flow across the entire detector. The mesh-bars are not only glued onto the panel, but screws secure the electric contact between the mesh on the bars and the grounding on the drift panels. To allow the glue to transfer the forces of the mesh onto the bar, the bar is grooved and slanted. A picture of the described parts can be seen in figure 7.4. Due to the complexity of the machining procedure, the corner pieces do not have multiple grooves. After the panel has been produced, the mesh has

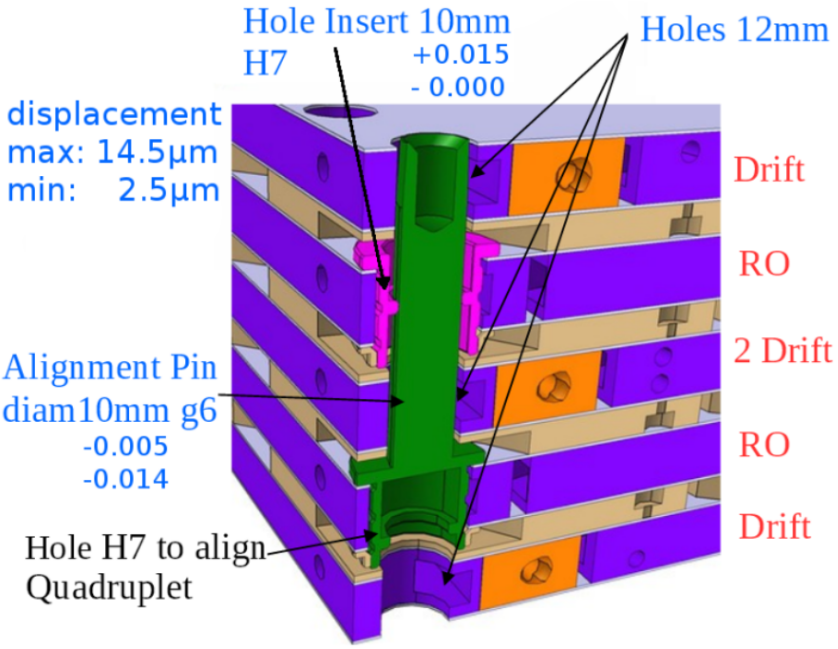

Figure 7.5.: Schematic view of the alignment procedure. The pin is glued onto the stereo readout board.The holes in the other boards align each of it to the tolerances given.

to be added. The procedure for mesh finalization, as it is called, will be discussed in section 7.2.

7.1.4. Quadruplet Assembly

The correct alignment between the panels of one module is critical to ensure a good track reconstruction. As such, the assembly has to focus on alignment. Onto the stereo readout board, alignment pins are glued right after the glue used during panel construction has cured. These alignment pins then slot right into the holes on the corners of the other panels, aligning them to the corresponding requirements. A picture of the alignment with the respective tolerances can be seen in figure 7.5.

In addition to the alignment. The gas volumes need to be tightened. Bars are added onto the outer rim of the drift panel. Between these bars and the mesh bar, a rubber o-ring is placed to serve as a gasket. After the quadruplet is assembled, the gas tightness is tested by putting the module under pressure and measuring the decay of that pressure over time. After that, the panel is tested under high

voltage, first in air, then in a mixture of 97% argon and 7% carbon dioxide. If these tests were satisfactory, the panel is tested on a cosmic ray bench and an efficiency and gain map is taken. If the module performs as expected, it is shipped to CERN, where it is tested again and integrated with other detectors into the Micromegas double wedge. Once the sTGCs are added to either side of the double wedge, the assembled sector will be mounted onto the NSW.

7.2. The Finalization of Drift Panels

The steps in the production of the SM2 performed in Würzburg are cummulatively described as finalization of the drift panels. The mesh, delivered by the weaving-company, is unrolled, checked for errors and put onto a transfer frame and cleaned. After that, holes need to be punched into the mesh to allow for the screws (see section 7.1) to pass through. The drift panel is then prepared for the transfer of the mesh and cleaned one last time, glue is applied and the mesh is transfered. After quality control, the panel is packaged and send to Munich to become part of a full quadruplet. To assure quality and repeatability on each step, all production steps had to be standardized and all persons involved had to be trained to perform these steps reliably. To ensure an ideal environment for the finalization, all steps are performed inside a cleanroom.

7.2.1. Mesh Stretching

The stretching of the mesh can be split into several sub-steps. First, the mesh has to be unrolled from the tube it is delivered on. Then, it has to be inspected for damage, kinks or faults. Once the inspection is done, it has to be transferred onto the already prepared stretching table, where it then has to get clamped in a fixed procedure to ensure even streching onto the frame. After the tension measurement is performed, the mesh is glued onto the transfer frame. After the glue is cured, the mesh is trimmed and the mesh is ready for cleaning.

Mesh Unrolling and Inspection To prevent damage to the meshes during transportation, a tube containing ten meshes is wrapped in several layers of paper and bubble wrap in the factory. Once the wrapping is removed, the rolls have to be carefully handled and should always be stored hanging. Between two meshes, a sheet of paper the size of the mesh pieces has been put, which also covers the next sheet while still on the roll. The dimensions of the mesh and the other components can be seen in figure 7.6. As such, a frame had to be developed that ideally allows to move the roll from storage to the inspection table and unroll it by moving the roll over the table. The frame consists of two independent aluminium profile

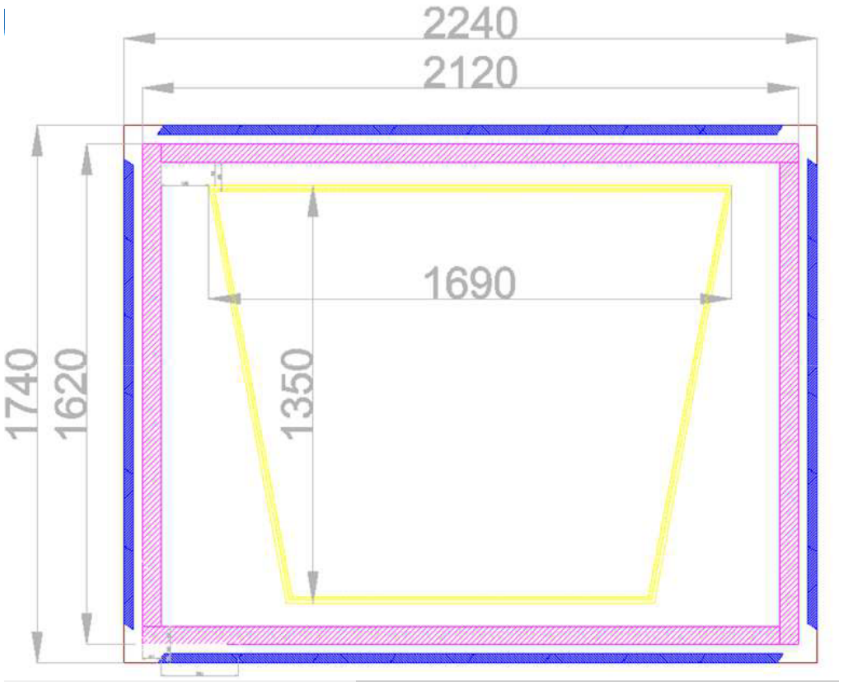

Figure 7.6.: Schematic view of the involved dimensions. Shown are the piece of mesh in black, the clamps in blue, the transfer frame in pink and the panel in yellow.

frames with a mobile base, onto which a pole with a holder for the mesh roll is placed. The holder on each frame has a small roll on the end to allow the tube to move freely. On one side, a lock mechanism was put to prevent uncontrolled rotation of the tube when moving or storing the mesh roll. This mechanism consists of two metal pieces that sandwich the cardboard tube and can be tightened by using a screw.

To ensure a stable construction, the bases of the frames were placed pointing inwards. This meant that the mesh frames had not enough space between them to pass along the inspection table for safe unrolling. Kinks can be produced in the unrolling process, which means the procedure needed to be as safe as possible. Therefore, the bases were rotated around and lead blocks were taped onto the bases to prevent any toppling of the frames. This made the unrolling procedure much safer, since now the mesh only had to be held on the end and the scroll could be moved freely along the table. After the mesh is on the table, a visual inspection is performed. Any kinks, damages, or faults are recorded on the corresponding mesh data-sheet, the label on the mesh specifying the mesh number and any faults found in the factory is removed and the mesh is transferred onto the stretching table that has been prepared during the inspection.

Figure 7.7.: A photograph showing the stretching table. The central plate is in its up position, the transferframe is put onto the clamps, which are arranged and prepared for the mesh transfer.

Preparation of the Stretching Table The stretching table was custom built for the production of the SM2. A picture of the table can be seen in figure 7.7. The central piece of the table is a plate of PVC that can be pneumatically raised or lowered. Onto the tabletop around the plate, pneumatic clamps are placed to allow mesh stretching. 8 clamps are placed along each long side, while 6 clamps are placed along the shorter sides. The clamps are labled 1-8 and A-F for the long and short sides, respectively. Onto the circle of clamps, the transfer frame is placed, onto which the mesh will be stretched before it gets transferred onto the panel. To allow for some self-alignment and to allow for the force to be transferred onto the transfer frame, the clamps are only placed onto the table and can move freely. This freedom is especially important since the transfer frame will deform under the force. For the preparation of the table, if there is an already stretched mesh, it is taken off and a new frame is placed onto the clamps, which are then aligned with the frame. Once the alignment is complete, the central plate is moved up. This will keep the mesh from falling through the mesh frame before it can be fully clamped down and the stretching can be started.

Transfer onto the Stretching Table The process that is most likely to damage the mesh during the mesh stretching is the transfer from the inspection table to

Figure 7.8.: A photograph showing how the mesh is transported from the inspection table to the stretching table

the stretching table. As soon as the mesh is constrained in two dimensions or completely unconstrained, it will start folding and crumpling, causing kinks. As such, care has to be taken to only apply force onto the mesh along one side. To that end, two persons pick up the mesh on opposite ends, making sure that the side they are holding is left to hang freely, forming a parabola, and the other side is being kept on tension. It is then slowly and steadily transferred over to the stretching table and carefully lifted onto the frame. A photograph of this procedure can be seen in figure 7.8.

Stretching and Gluing After the mesh is placed onto the table, two people start clamping down the mesh from opposite corners. The shape of the clamps only allows closing them going clockwise. First, the clamps are only placed onto the mesh, causing any irregularities like missalignment to show up. After any irregularities have been fixed, the clamps are closed tightly and the stretching pressure of 2.5 bar is applied. After that, the central plate is moved down, freeing the mesh and enabling the measurement of the mesh tension by displacement. The *SEFAR Tensioncheck 100* is used to measure the mesh tension. The tool consists of a body with a known mass and a round plate attached to the bottom and a moveable ring plate with a known radius. From the displacement between the center plate and the ring orthogonal to the mesh plane, the tension of the surface can be determined. Due to the fact that it is not necesserily homogenous over the entire mesh, the tension is measured in a 8x6 grid with points in the center of each

clamp. The measuring tool and an example of the mesh tension map can be seen in 7.9.

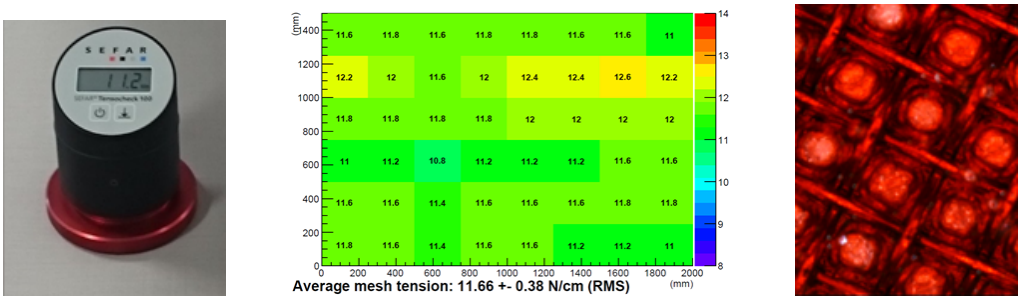

Figure 7.9.: (a) the tension measurement tool, the body is black and the moveable ring plate is metallic red, (b) an example for a tension map of a mesh, (c) photograph of the Kiwobond glue, one can see the touch fastener-like structure with the cured glue hooking the hoops of the mesh.

If the tension is out of specification, i.e. inhomogenious or deviating to much from 10-12 N/cm, the central plate will be moved up again, the mesh unstretched and the clamps can be adjusted. Ensuring a predictable tension creates predictable sagging of the mesh in the finished detector, thereby ensuring a uniform amplification gap. Once the tension map is within specification, Kiwobond 933 Rapid, a two component glue specifically made to glue meshes to frames, is spread through the mesh onto the transfer frame. It fixates the mesh onto the frame, allowing force transfer in the mesh plane, while being easy to remove by pulling the mesh off the frame orthogonally, working similar to a touch fastener (see figure 7.9). An additional advantage of this glue is the ease of cleaning using a cooktop cleaning scraper, making it easy to reuse mesh transfer frames over and over. Once the glue is applied, it needs to cure for several hours. This curing is usually left over night. The next day of production, the pressure on the clamps is released, the mesh is cut down to the outer dimensions of the transfer frame to prevent accidental forces from detaching the mesh and the mesh tension is measured again. After both tension maps have been entered into the mesh data sheet, the mesh is moved to the next step, cleaning, and the table is prepared for the next mesh.

7.2.2. Cleaning of the Mesh

The finalization of the drift panels is done in a cleanroom. As such, any work generating dust or aerosoles should be avoided. The mesh, coming from the factory, might, however, contain grease from the production process, which must be washed

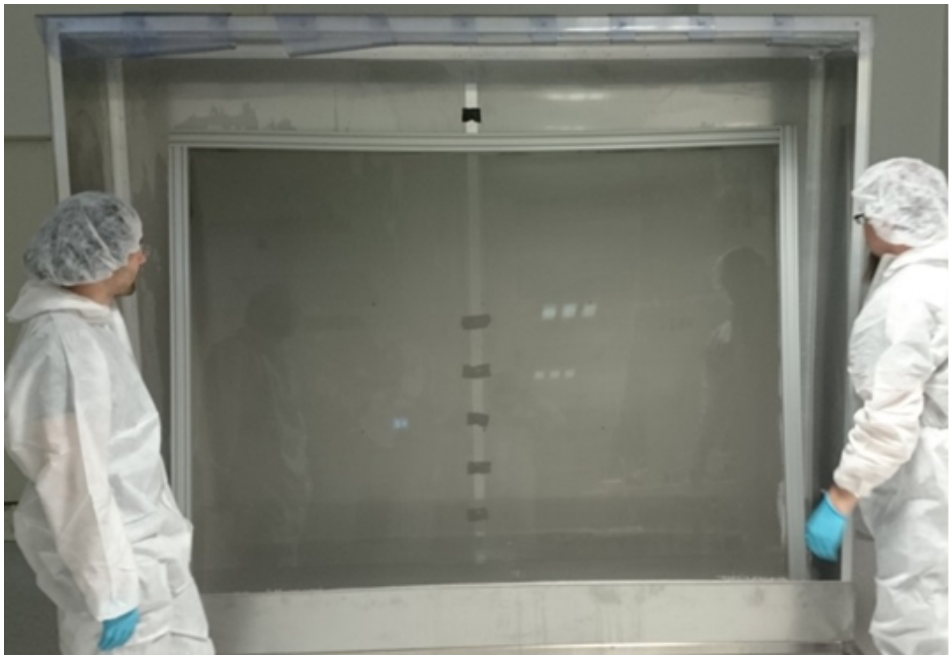

Figure 7.10.: Photograph of the washing box into which a mesh has been placed. The transfer frame is deformed under the forces exerted onto it by the mesh. The plastic curtains were still attached and are folded up.

off before it can be installed in the detector. To facilitate this washing procedure and to protect the cleanroom atmosphere from any water droplets, a special box was designed. It consists of a tub into which the mesh can be placed upright into the box. Three sides, both short and one of the long sides of the tub, are extended above the mesh, allowing the mesh to lean against the large wall. A picture of the box can be seen in figure 7.10.

For the cleaning of the mesh, a high pressure water jet is used. First, NGL 17.40, a special cleaner for meshes, is prepared with a solution of 20 g of the cleaning powder with 2 ℓ of water at 60 °C and is then spread onto the mesh from both sides using a brush. After five minutes of rest to let the cleaning solution take effect, another 10 ℓ of water are used to remove the cleaner using the high pressure jet. The mesh is then rotated again and another 10 ℓ are applied to the other side.

In the beginning, heavy plastic curtains were placed on the opening, preventing any water droplets to get out of the box. During the first repeats of this procedure, the curtains proved to be dangerous to the mesh. Due to the large flux of water, they would be dragged into the box, hitting the mesh. To mitigate this problems, magnets were attached to the inside of the box and the end of the curtains. This worked to prevent the dragging of the curtains, but when the curtains were moved

Figure 7.11.: Photograph of the washing procedure. The high pressure cleaner is pointed through the curtains, which catch any droplets.

up or down before or after the procedure, the magnets could hit the mesh, causing even grater damage. Therefore, they were removed again. With the curtains becoming slippery after the first side, the heavy curtain could slip out of the hand of anyone taking them down, creating enough force to not only cause kinks in the mesh, but to actually cause a tear. As the curtains proved to dangerous to use, they were removed and the box was moved into a separate part of the cleanroom, causing any aerosoles created by the high pressure cleaner to not spread into other parts of the cleanroom, thereby mitigating the original problem the curtains were intended to solve. A picture of the cleaning can be seen in figure 7.11. After the washing procedure is done, the mesh needs to dry over night.

7.2.3. Passivation and Punching

The mesh in the detector is not a full plane, but needs holes through which screws can be put to prevent a bulging of the detector when under pressure, see section 7.1. If those holes would just be punched without preparation, the mesh would start disintegrating around the cut, caused by the now open strands unravelling. To prevent this, the location of the holes is *passivated* before the punching. A small, circular drop of glue is placed onto the mesh and dried. First, the mesh is taken out of storage or the washing box and placed on a table that has 6 blocks of PVC placed at the locations of the holes. Onto these blocks, tedlar foils are placed. Tedlar was chosen because it does not stick on the glue and can be removed easily. A template mylar foil the size of the panel is placed onto the mesh. Through 6 holes in the foil where the bolt would go through on a real panel, marks are made

on the mesh with a marker. Once the locations of the bolts are marked, the glue has to be prepared. The glue used is Araldite 2011, a two component epoxy. It is mixed automatically in a syringe like mixing tip and can be extruded directly onto the surface that has to be glued. The procedure can be seen in figure 7.12.

Two pieces of 5 cm $\times$ 5 cm, one of mylar and one of tedlar, are prepared. Into the piece of mylar, a hole of 1 cm diameter is punched. The piece with hole is then placed onto the tedlar piece, centering the hole. Some glue is put on the upper piece of mylar. Using a metal scraper, the glue is spread over the upper piece, creating a round dot of glue in the hole. The upper part is then removed, leaving a round glue spot on the piece tedlar below. This is then placed glue down onto the marked location on the mesh and a plastic block and a lead weight are placed onto the tedlar to flatten the resulting dot of glue.

At the beginning of the production process, all sheets used were made of mylar, but the mylar showed a habit of sticking to the glue, making it hard to remove from the mesh after curing. With the exception of the piece used to shape the glue dor, the mylar was therefore exchanged for a different material, tedlar, which did not stick to the glue at all while at the same time needing no adaption of the passivation procedure. While the mylar sheets had to be discarded after every passivation, the tedlar could be reused without issues, since no residue would be left on the sheets after the procedure.

After the glue has cured, which takes over night, and the sheets of tedlar have been removed from the mesh, the hole can be punched. The mesh is lifted onto the panel it is to be joined with, aligned in such a way that all six dots of glue are covering the holes a well as possible. The locations are then marked again. While this is happening, three sheets of mylar are placed on each of the blocks on the other table. The mesh is then put back. A special punching tool is then used to create the hole. It consist of three pieces. A clear plastic cylinder with a 6 mm hole in the center is used to guide the tool onto the correct spot on the mesh. After it is aligned with the marking on the mesh, a 5 mm diameter metal pipe with a sharpened end is put into the hole. A cylindrical weight with the same dimesions as the clear cylinder is then put onto the pipe and dropped onto a rim that has been welded onto the lower part of the pipe. The kinetic energy of the weight causes the pipe to be slammed against the mesh with the sharp edge. This will punch a hole with a diameter of 5 mm into the mesh and into one or two layers of the mylar below. Using more force than necessary ensures that the cut in the mesh is as clean as possible, sacrificing a few pieces of mylar. The procedure can be seen in figure 7.13.

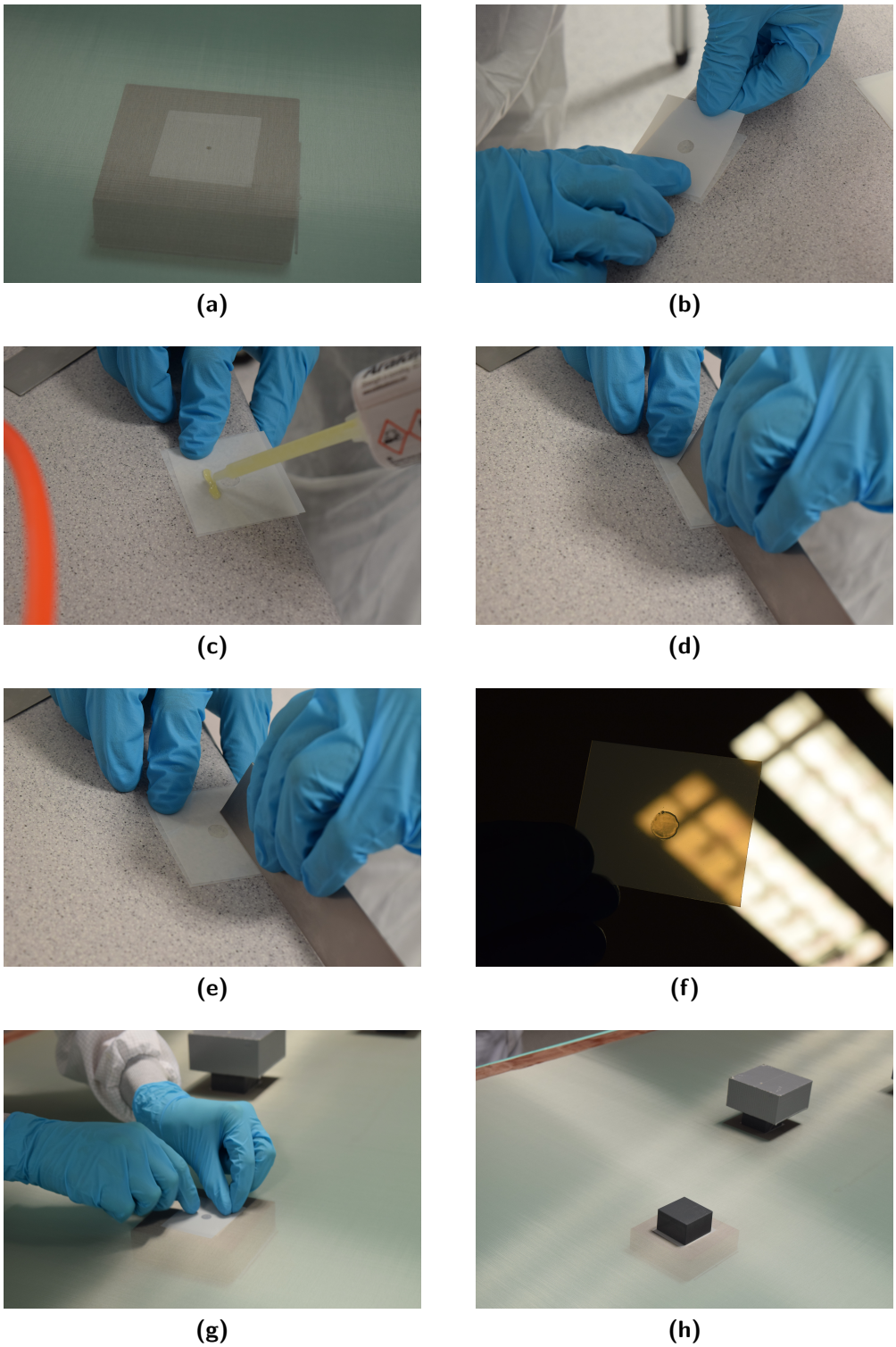

Figure 7.12.: (a) The prepared location, (b) the two sheets of mylar (old procedure), (c) adding glue onto the mylar, (d) and (e) spreading the glue, (f) the resulting glue dot, (g) placing the glue, (h) placing the weights

(a) (b)

Figure 7.13.: (a) aiming using the clear cylinder, (b) the moment the weight is dropped

7.2.4. Transfer of the Mesh onto a bare Drift Panel

The transfer itself can be subdivided into several stages. The panel has to be prepared to allow for the mesh punching. After the holes have been punched, the mesh has to be realigned and position needs to be fixed. Then the mesh is cleaned and glue applied. After the glue has been applied, the mesh and the panel are joined and prepared for the curing of the glue. Since the mesh cannot be moved once it comes into contact with the glue, all steps have to be performed very carefully.

Preparation of the Drift Panel The mesh does not just have to be transferred onto the panel, it has to also retain the tension of the mesh and transfer the force from the transfer frame to the mesh frame on the drift panel. To achieve this transfer, the transfer frame and the drift panel have to be not only aligned in the table plane, but also in the correct heights. As described in section 7.1, there are two different types of drift panels, single-sided and double-sided. Naturally, the double-sided panel is thicker than the single-sided one, by the height of the mesh frames. To compensate for this and allow the use of the same tools, the single-sided panel is put onto shims the size of these mesh bars. From there on, the different panels are treated the same.

By its very nature, the transfer frame is larger than the drift panel. To allow for alignment, the drift panel has to be extended. This is done by adding metal *ears* to the sides of the panels. To allow for some latitude, the ears are connected via adapter bars. The two sets of screws allow for some movement of the ears,

Figure 7.14.: Photograph of the drift panel with mesh during the alignment. Visible are the ears on the drift panel and the cylinders, which are already fixed to the mesh position.

so they can both connect to the drift panel and sit on the table. The height of the ears was designed to allow for the frame to sit on them in exactly the right height. For horizontal alignment, each ear has 3 elongated holes. A cylinder can be screwed into the groove. Once the mesh is aligned in such a way that the holes are placed exactly above the holes in the mesh, the cylinders can be pushed against the mesh and fixated. With three cylinders, this makes the mesh position reliably reproducible. A picture of the prepared drift panel during mesh alignement can be seen in figure 7.14. Once the mesh position is set with the cylinders, the mesh is taken off again, and the cleaning of and glue application on the drift mesh can proceed.

Cleaning and Glue Application Before the glue application begins, the copper anode of the drift panel is cleaned for one last time before the mesh will make cleaning impossible. First, ethanol is used to clean the copper cathode surface and the bars. The copper surface is then cleaned off all residue dust using a static cleaning roll. As a last step of cleaning, every trace of fat is removed from the mesh bars using acetone. Once the cleaning is done, the gluing tool is prepared.

The glue has to be at the same height above the bar every time to guarantee a good connection of the mesh to the bar, while at the same time not extending above the bar to allow the panel to close. As seen in 7.1, the bar has a special shape with grooves that help the glue to anchor into the bar structure. This complicated structure makes using a special tool necessary. The tool can be seen in 7.15. To be able to clean the tool fully using acetone, it has to be assembled freshly for every gluing step and disassembled right after the gluing is finished. This prevents glue from accumulating in the corners of the tool, which would change the spread of the glue after a few days. Assembly is done using the mesh bar on the panel with a taper feeler gauge leave of 0.15 mm height simulating the perfect layer of glue.

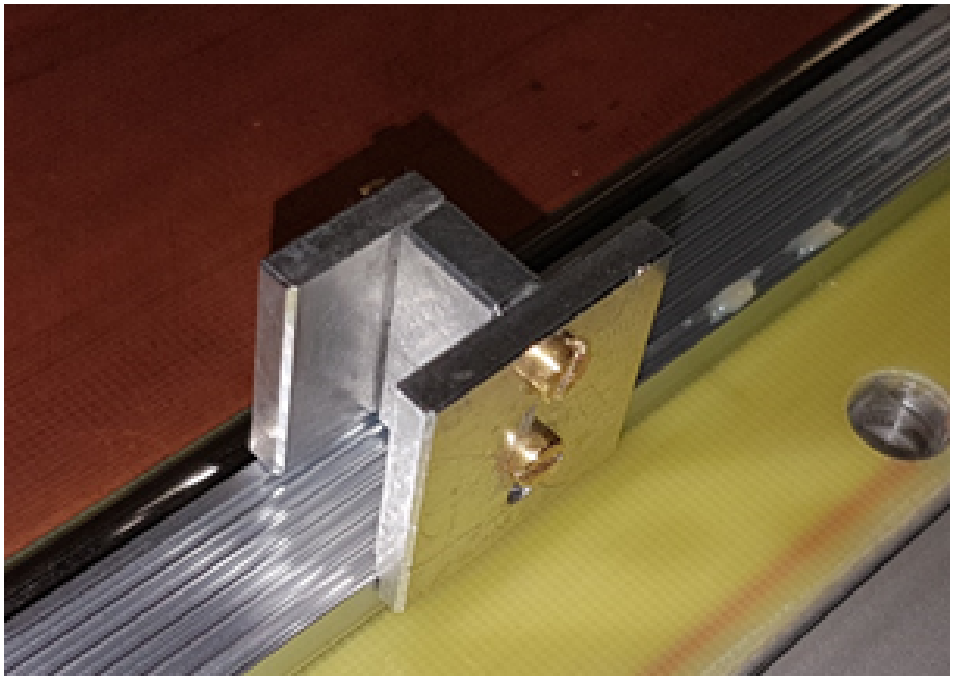

Figure 7.15.: Photograph of the gluing tool on the mesh bars.

Once the tool is assembled, the glue application can begin. Two people are needed to apply the glue, one pushing the tool with constant speed, the other using the glue pistol to add glue into the front of the tool, as can be seen in figure 7.16. Two laps around the panel are made. The first lap of the panel mainly serves to add glue onto the bar, while the second lap is then used to create an even layer of glue. The glue is thick and therefore barely able to flow into the grooves on the bar. To make it more fluid, the glue is heated up to around 60°C. Even then, air can get trapped below the glue, creating bubbles that compromise the glue layer. These bubbles have to be opened up by a third person, using a scalpel, during the first lap, to be then filled during the second. Due to the heat applied, the glue will begin to become hard quickly. Since the procedure relies on the glue being sucked into the mesh holes, the glue application has to be performed within half an hour.

To find the perfect glue layer for the transfer, several trial runs had to be performed. Glue temperature, tool gap setting, movement speed of the tool during application and amount of glue in the tool had to be experimented with, finding the right values by inspecting the end result. Once the glue layer is applied, mesh and drift panel can be joined.

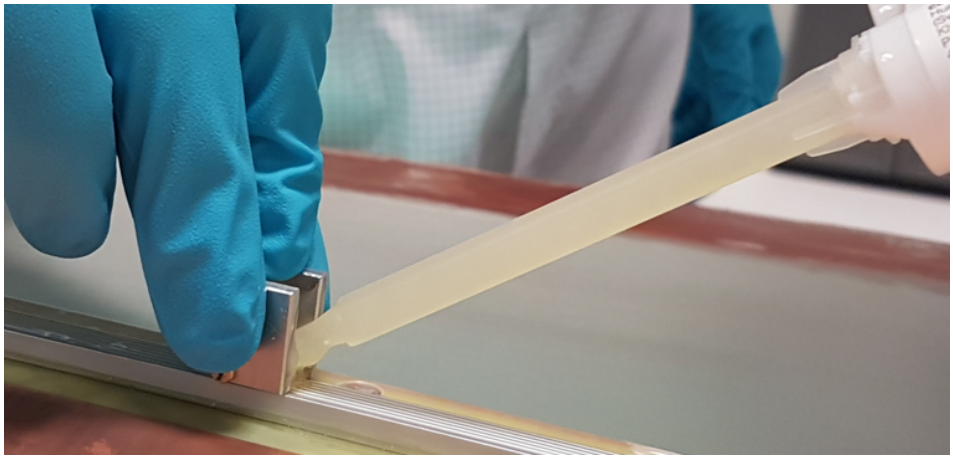

Figure 7.16.: Photograph made during the glue application (first lap). One person is moving the tool steadily along the bar, while another person is applying glue to the front part of the tool.

Joining of Mesh and Drift Panel Just before the mesh is joined with the drift panel, it is cleaned with the static roller on both sides. The frame is then put mesh side down onto the drift panel, using the cylinders on the side to align the mesh. Once the mesh has been placed on the drift panel, it can no longer be removed, since the glue has already touched the mesh. A bar just larger than the panel is then placed on the mesh. The bar has a rubber seal on the inner side, both pushing the mesh further down and protecting the mesh from the corner of the bar. Onto the frame, weights are placed. This secures the contact of the mesh and the bar on the drift panel, pushing the glue into the mesh holes. Through experimentation, it turned out that the best layer of glue was obtain by using more than necessary glue. Since the glue should not extend above the bar, the excess glue has to be scraped off the bar to the outside using a piece of mylar. Especially on the corner, where no grooves have been carved into the bar, this scrape off procedure is necessary. The joined mesh and drift panel, with the glue extruding from the mesh, can be seen in figure 7.17.

The drift panel is then left overnight to let the glue cure. For the single-sided drift panel, the transfer is completed and the panel must now be finalized, while for the double-sided drift panel, the second side needs to be transferred beforehand. During the first transfers, the force would not be fully transferred onto the panel. The reason was found to be the pushing frame hitting the ears while the weights were attached. This was fixed by milling the ears down to half thickness on the first 5 cm close to the panel. This allowed the pushing frame to fully push down the mesh.

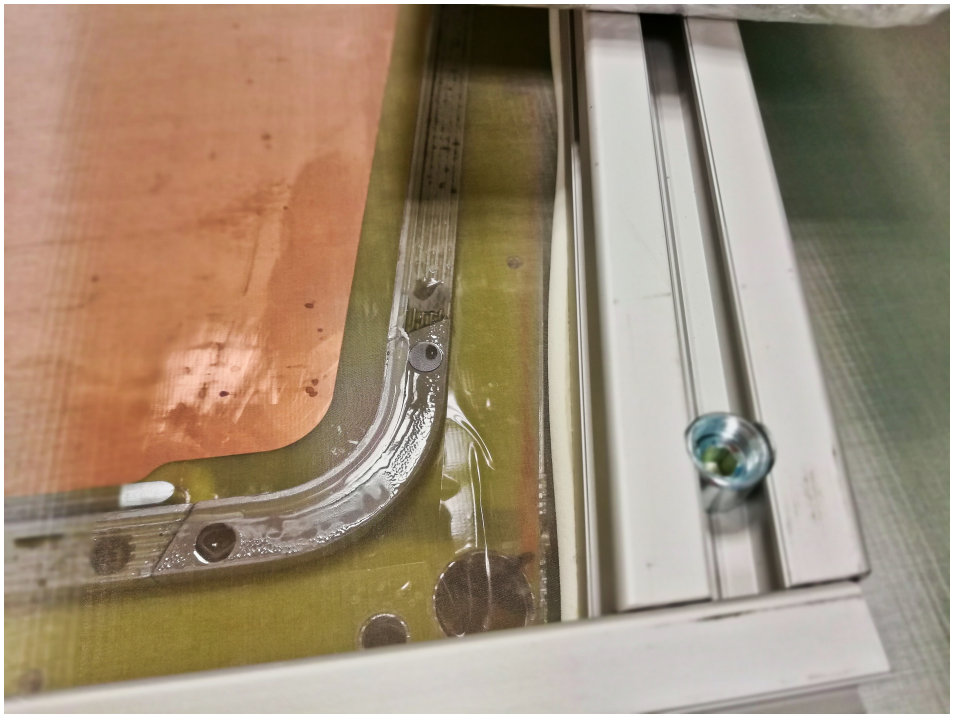

Figure 7.17.: Photograph of the joined mesh and drift panel. The pushing frame is placed on the mesh, the white rubber seal prevents damage to the mesh. Some weights (top edge) are already applied. The glue is extending above the corner of the mesh bar.

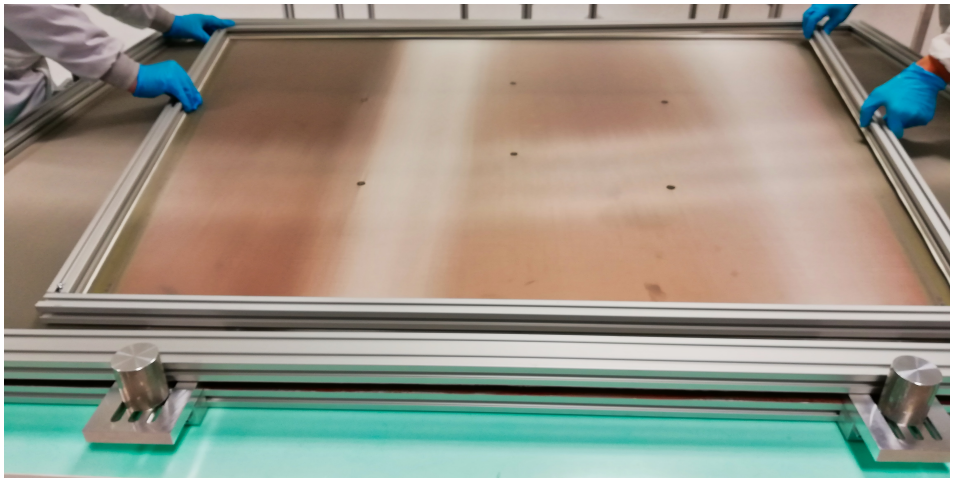

Figure 7.18.: Photograph of a double-sided panel after both meshes have been transferred. The pushing frame has just been put onto the second side. The ears have been attached to the lower transfer frame, while the cylinders align the upper mesh to the drift panel.

Flipping the Double Sided Drift Panel For a double-sided drift panel, the transfer is not over after the first mesh has been joined. To prevent any deformations from the force of the first mesh to influence the transfer of the second mesh, the second transfer takes place with the first transfer frame still attached to the panel. The cylinders for alignment are removed from the ears and connectors are used to fix the transfer panel to the ears. Each connector is connected to all 3 holes in the ears and two slot nuts that have been put into the slot in the transfer frame. This prevents any relative movement between transfer frame and drift panel while the panel is flipped. In addition, buffers made from styrofoam are placed below the mesh bars of the already joined side to take any load of the mesh. To prevent any styrofoam to contaminate the panel, the buffers are covered with kapton foils. Once the panel is flipped, the transfer procedure is repeated for the second side. Once this transfer is completed as well, the double-sided panel can be finalized. A picture of the double sided panel during transfer can be seen in figure 7.18.

7.2.5. Finalization

The finalization of the mesh contains everything needed to finish the drift panel so that it can be used in the detector. This includes the cutting of the mesh, cleaning of the cut and packing for delivery. Once the glue is cured, the transfer frame can be removed. Since the load on the transfer frame is substantial, it is released by using a clamp to unload it. The mesh is then first cut on the inside of the transfer frame, leaving now unloaded pieces of mesh on the panel. The rest of the mesh on

Figure 7.19.: Photograph of the cutting procedure. The mesh has to be taken out carefully to prevent any open wires.

the transfer frame can then be removed, any residual glue on the frame scraped off and the frame reused.

After the frame has been removed, the next step is to cut off the mesh protruding from the mesh bar on the drift panel. The high voltage on the readout board is only around 100 µm away from the grounded mesh. As such, any free mesh wire could cause a short circuit. To prevent this, the mesh is cut inside the glue layer, namely the outermost groove on the mesh bar, using a utility knife. This has to be done very carefully, so that every wire is cut completely and does not get ripped out of the glue when the outer part of the mesh is removed. A photograph taken during this procedure can be seen in figure 7.19.

Once the mesh is cut, the cut has to be checked for any free wires. This is done using a strong light and a magnifying glass. Using tweezers, every open wire is pulled out. These wires are usually very short, but can be long on occasion. An example of a long open wire can be seen in figure 7.20. Once the wires are removed, a piece of adhesive tape is used to get any residue metal and glue off the cut area by sticking it onto the bar and taking it off again. Once the big residue is gone, the static cleaning roller is used once more to remove all smaller pieces that might remain on the mesh bar. For the double sided panels, this procedure is then repeated for the other side. Once the sides are done, the ears are removed. After the cutting procedure is done, the tension of the mesh on the panel is measured once more. This time it is measured in six lines along the parallel sides, of which the longest have six points and the other four have four points each. The panel is then put into a bag of bubble wrap for transport.

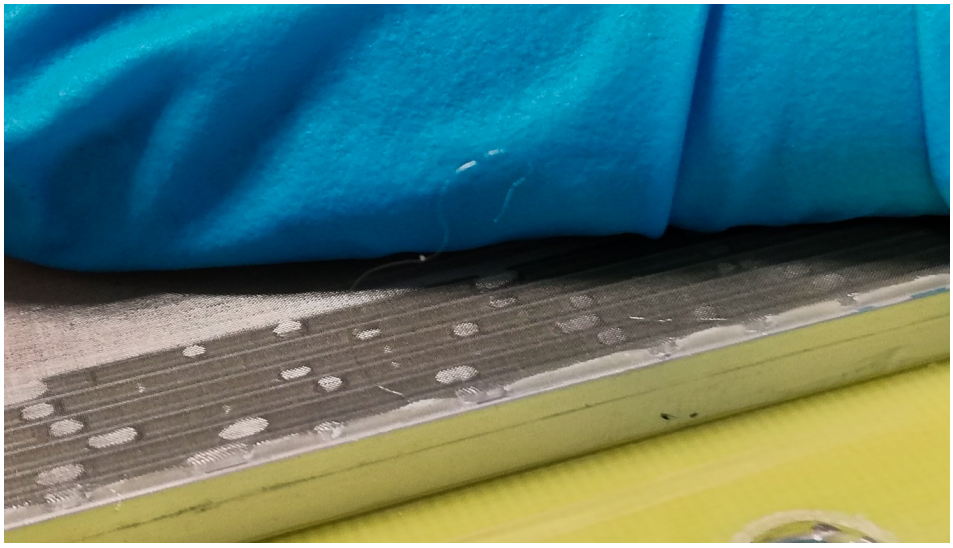

Figure 7.20.: Photograph of an open wire left after cutting. The wire is comparatively long.

7.2.6. Quality Assurance and Quality Control

To ensure tracability and quality accross all drift panels that are finalized in Würzburg, every mesh has to be tracked through the production. First, 140 meshes were delivered with a mesh number on a label on every mesh. This mesh number is associated with a data sheet from the factory containing any irregularities, like weaving errors or similar. None of the meshes delivered had any problems noted on their respective sheet. The meshes are identified by that factory number during all activities on site. On every roll, ten meshes are put in reverse order, i.e. mesh 10 will be runrolled first, with mesh 1 being the last on the roll. The first roll that was used in the production was roll 40-31. This was continued in order until mesh 1. After that, meshes were taken from 140 down to 41. As more drift panels were needed, another 30 meshes were ordered, with number 141-170. These were used from 150-141 first.

Every mesh receives its own data sheet during production. It notes mesh number, transfer frame number, the glue used to glue the mesh on the transfer frame and the pressure used to stretch the mesh on the first page. In addition, the first page contains a field for comments, noting any kinks or other problems that may have arisen during handling. It also contains both of the tension maps measured before and after gluing on the transfer frame. The reverse side contains all informations regarding the transfer, including drift panel number and side for double-sided panels, another comment field and the tension map taken on the panel. An example of the mesh data sheet can be seen in appendix A.

In addition to paper tracability, a local database was set up using Python 2.7 and MySQL. The database used the Munich database as template and introduces tables for meshes and panels to sort all the information before it is being transferred to the central databases at CERN. These include a logistics database, noting when which panel arrived in Würzburg, was finalized and which mesh(es) was (were) used, and when it was send back to Munich. The other database is the quality control database. Every full tension map, including its mean and its rms is added to the database, allowing anyone to check the parameters of the used meshes should any performance issues come to light during commissioning or use of the detector components.

7.3. Effects of the Mesh Geometry on the High Voltage Stability

During the assemby of the first modules, several questions arose. This included the question, how the mesh geometry can influence the high voltage stability of the detector. Several different effects have been investigated to that end: If microscopic damages on the wires can cause high voltage instability and if they can be removed by sanding he mesh, if a mesh with a different geometry performs better and which side of the mesh should be pointed towards the readout.

7.3.1. Damaged Mesh Wires and Sanding

During weaving, transport or at any time during the transfer, wires can be slightly damaged on a microscopic scale. Since the detectors are using fields close to their break through voltage, even very small damage can locally increase the field strength in such a way that a spark can occur. Theoretically, these damages can be removed by sanding off the surface of the mesh. The mesh was sanded with P2500 sand paper on both sides, once in passes from left to right and once from top to bottom. After that, lapping film sheets of 0.3 µm granularity were used. The sanding procedure produces dust and could therefore not be performed inside the cleanroom. The meshes were taken out of the cleanroom into the yard after stretching, sanded and then brought back into the cleanroom for washing. The washing was performed until it had removed all the dust left on the mesh. After the treatment, the meshes were used as normal an put onto panels.

These sanded Meshes were transferred like all other meshes and send to Munich for assembly.

Since the sanding procedure would have meant much more chance for the mesh to get damaged or dirtied by moving it not just out of the cleanroom, but into the open, it was abandoned.

7.3.2. Different Mesh Geometry

The best mesh geometry for signal formation is not necessarily the one that can be used in a large detector. Meshes are fabricated on a large loom. The wires in a mesh can be distinguished by the way they are used in the loom. The warp wires run along the length of the cloth, being fixed in the loom during weaving, while the weft is the wire being moved back and forth along the loom. The number of warp wires is limited by the loom construction. As such, for a given distance between wires, the maximum width of the piece of mesh is directly given. For example, for the usual 45-18 mesh used in small micromegas detectors, 22222 wires are used per meter of mesh. As such, in a machine that can have 50000 warp wires at once, the maximum width of the mesh can be 2.25 m. If larger meshes are needed, the distance between the wires has to be increased to be able to manufacture the mesh in one piece. While the mesh size would have been just enough to cover a SM2 mesh, but not the transfer frame, it would not have been enough to produce meshes for the larger modules. To have the same properties for every module, the same mesh, 71-30, was chosen for all of them[33]. To understand the differences, two meshes of the 45-18 type were extended by gluing other mesh pieces on each side so they could be put onto transfer frames. They were then treated like all other meshes and together transferred on a double-sided panel in such a way that only the 45-18 mesh was transferred onto the panel.

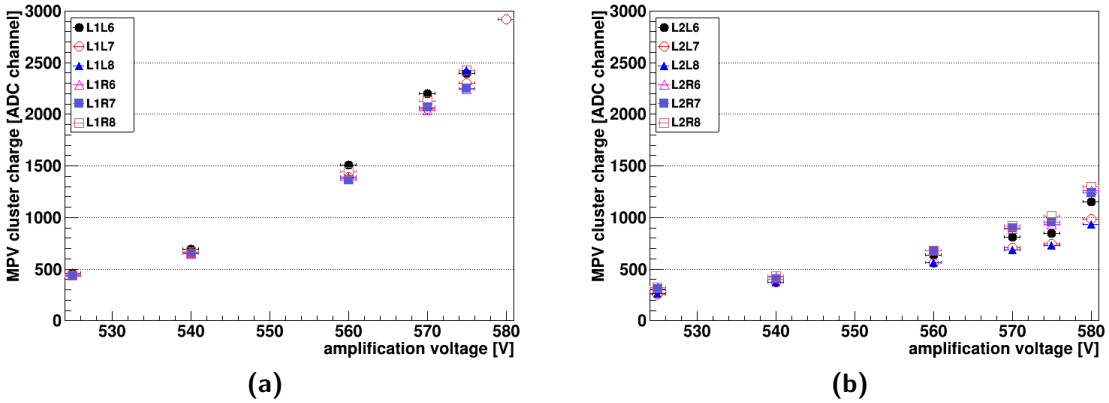

Figure 7.21.: Mean cluster charge for (a) Layer 1 (regular mesh), (b) Layer 2 (45-18 mesh), different points are different PCB (and left or right side)

The panel was send to Munich, and was assembled together with two regular single-sided drift panels into a module and tested there using the internally defined QA/QC procedures. All plots shown in this section have been kindly provided by the LMU Munich ATLASgroup. The 45-18 mesh geometry can be probed by com-

paring the outside layers with the inside layers of this module in the regular tests. This comparison for one inside and one outside layer can be seen in figures 7.21 (the other two layers show the same behaviours, respectively).

One can see that the behaviour for different amplification voltages is much different for the new mesh geometry. It appears to be more stable, showing lower peak heights compared to the regular layer. Therefore, the apparent high voltage instability could just come from higher amplifiactions at the same voltages. If one compares the efficiencies for the same layers, seen in figures 7.22.

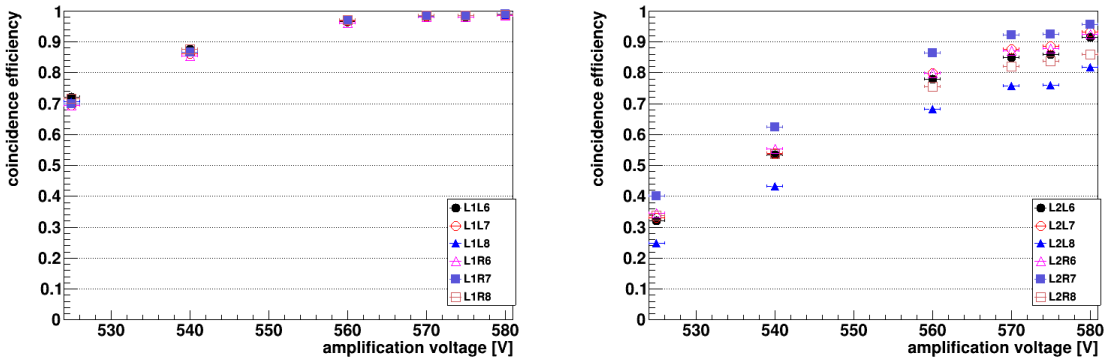

Figure 7.22.: Mean cluster charge for (a) Layer 1 (regular mesh), (b) Layer 2 (45-18 mesh)

As one can see from the efficiencies, the layers with the regular SM2 mesh perform better at lower voltages. The meshes have not been tested at a drift voltage above 580 V, as this was considered the maximum safe voltage, with the efficiency expected to increase to a value close to one if increased even further. In conclusion, the lower voltage compared to the 45-18 mesh used in small-scale detectors might be a result of the switched mesh and not an indication of a broken detector, at least from the side of the mesh.

7.3.3. Mesh Side

During the discussions around damages on the surface and the mesh geometry, the supplier was asked for feedback regarding damage to the mesh. The reply included the information that the side which points up during the weaving process usually exhibits much fewer of these damages than the lower one. This side would usually be the one that is pointing up during the stretching, which means it would point towards the drift cathode during transfer. Therefore, the procedure was adapted in such a way that the mesh would be unrolled so that this side would point down,

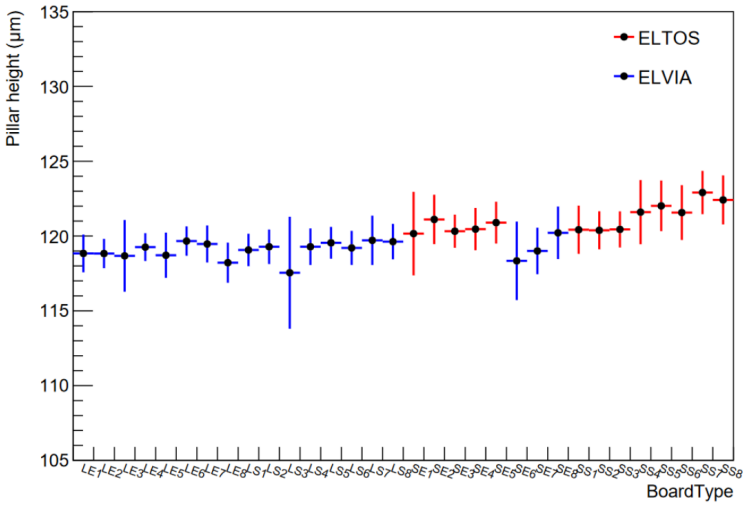

Figure 7.23.: Measured average pillar heights for each board type, error bars are the RMS of the average pillar height distribution across all boards of that type. The deviation between the two producers (in different colors) can be seen clearly, from [101]

resulting in it pointing towards the readout after transfer. This change did not complicate the procedure or make it more likely for the mesh to get damaged. From mesh 101 onwards, all meshes were transferred this way. An effect of this change on the high voltage stability could not be confirmed, however.

7.4. Simulation Study on Gain Variations due to Gap-Size Variations

The readout boards used in the NSW are made by two different companies. Since every readout board type used in the detectors is different in shape, the process varies slightly for every board, causing the mean pillar heights differ between types, with types made by different companies differing even more. A measurement of average pillar heights can be seen in figure 7.23. In the SM2, which uses boards from both companies in one layer, these differences are especially pronounced. To understand the gain differences associated with these gap size variations, simulations are necessary. In addition, simulations can help find the voltages needed for each gap size to set a uniform gain across the detector.

The simulations were made using the same software as used for the gas contamination study, see section 4.3.1. The field map recreates the 71-30 mesh used in the SM2 and the detector is again simulated as infinite plane. In this case,

gap size in µm	Anode Voltages in V	Number of Events
118	560, 570, 580	3000
120	560, 570, 580	3000
122	560, 570, 580	3000
124	560, 570, 580	3000
126	560, 570, 580	3000
128	560, 570, 580	3000
Validation Samples		
131	570, 583	3000

Table 7.1.: List of generated samples for the gap size study.

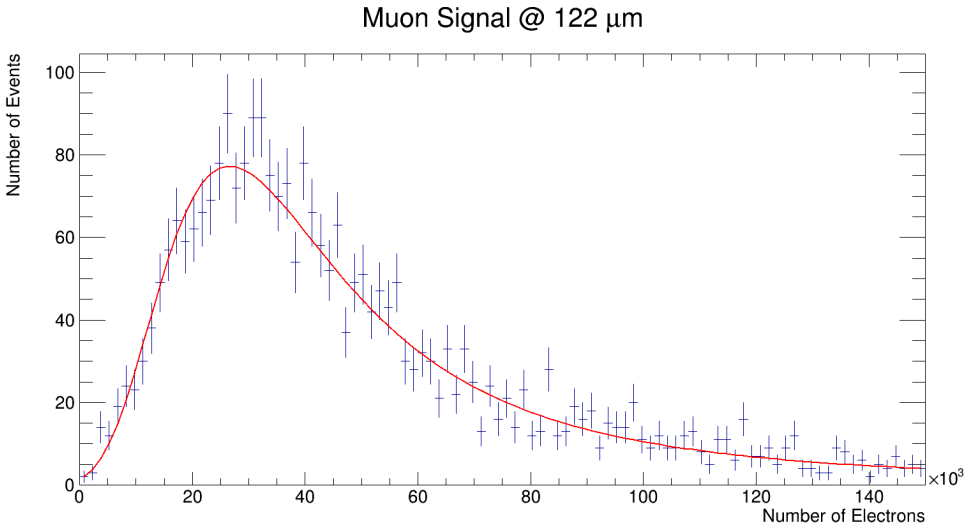

Figure 7.24.: Histogram of the number of electrons found in 3000 muon events at a gap size of 122 µm

the mesh is grounded, while the anode and cathode are set to 570 V and -300 V, respectively. The gap size was simulated at 118, 120, 122, 124, 126 and 128 µm. To allow gauging the effect of the voltage change on the gain in the detector, the anode voltage was varied by 10 V in both directions, 560 V and 580 V. A list of the simulated points can be seen in table 7.1. For each event, one muon is injected into the detector.

As before, the avalanche size for each primary electron, the number of electrons on the anode, the induced signal on the anode and the induced signal after the simulated electronics are extracted. In this case, instead of fitting with a gauss function, the distributions are fitted with a landau function, see section 2.1.1. An example of this fit can be seen in figure 7.24.

From the landau fit, the most probable value for the gain G, electron number N and signal after simulated electronics (the height S and the integral S_{int} of that signal) can be extracted. This can be used to create another set of two dimensional graph that allow fitting of these curves to get the dependency on voltage and gap size changes. While the Voltage only influences the field, the gap-size also influences the available length for the avalanche formation. To understand the effects of both parameters on the gas gain, a fit was performed using

$$G = N \exp\left[A(d - 120\ \mu\text{m}) + B(U - 570\ \text{V})\right]. \tag{7.1}$$

With d being the gap-size, U being the voltage and $N,\ A,\ B$ as fit parameters. To find a good starting value for N on the fit, the function was chosen in such a way that for $d = 120\ \mu\text{m}$ and $U = 570\ \text{V}$ the function becomse $G = N$. The measured gain at those values can therefore be used as starting value for N. The 2D-fit of the gain can be seen in figure 7.25.

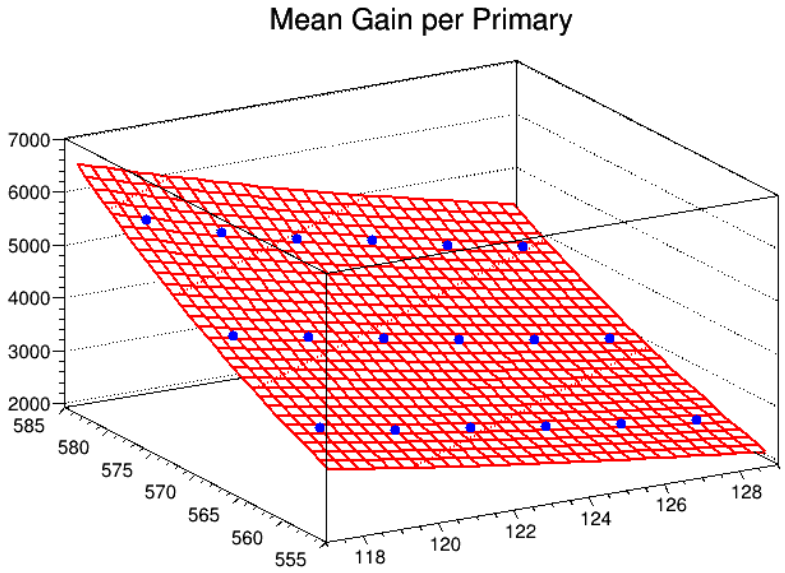

Figure 7.25.: The 2D fit of the gain

To make sure the assumption still results in values sufficiently close to the real value, the fit has to verified. As some exceptional boards exhbited gap sizes of more than 130 µm gap sizes, this verification was done by extrapolation. The value chosen was 131 µm, and the function is extrapolated to that gap-size and a voltage of 570 V. A simulation is performed at these settings and compared to the extrapolated values. The extracted and extrapolated values can be seen in table 7.2.

Value	Extrapolated	Extracted	Extracted / Extrapolated
G	2840	2840.15	1.0005
N	20876.1	20587.2	0.986163
S	12.9274 mV	12.7375 mV	0.986163
S_{int}	5188.07 nVs	5085.73 nVs	0.980274

Table 7.2.: Comparison of extrapolated and extracted values

Value	$d = 131$ µm	$d = 122$ µm	Ratio
G	3890±12	3890±13	1.00
N	28400±460	29000±440	0.98
S	18.5 mV±0.29 mV	18.7 mV±0.27 mV	0.99
S_{int}	7300 nVs±120 nVs	7200 nVs±100 nVs	1.01

Table 7.3.: Comparison of the extracted values at $d_1 = 122$ µm, $U_1 = 570$ V and $d_2 = 131$ µm, $U_2 = 583$ V

As one can see, the extrapolation fits the extracted values within the errors. To visualize this, the graph in figure 7.25 can be sliced at $U = 570$ V and then extended towards 131 µm and the point that has been extracted from the simulation can be added. This extrapolation is shown for all four values in figure 7.26.

In addition to the extrapolation, another question can be answered: Given two different gap-sizes d_1 and d_2, one can try to equalize the gain of both layers given the voltage U_1 applied to the first. Using equation 7.1, one can then find an equation for for the second voltage as

$$U_2 = \frac{A}{B}(x_1 - x_2) + U_1, \tag{7.2}$$

with the fit values obtained in the simulation.

To verify this approach, one such voltage was calculated and then verified by simulating another data point. The values chosen were $d_1 = 122$ µm, $d_2 = 131$ µm and $U_1 = 570$ V. The result of the calculation was $U_2 = 583$ V for all four properties. An additional sample was generated at d_2 and U_2 and compared to the sample that was already generated at d_1 and U_1. The extracted values and the comparison can be seen in table 7.3. As can be seen from the values, the gain equalization worked in the range used inside the ATLAS NSW in this simulation.

Independent of the simulations, the Maximilian Herrmann investigated the average pulse height depending on the average pillar height of the detector during his PhD work[102], the results of which can be seen in figure 7.27. As opposed to the simulation, which has perfect pillar heights all across the detector, a real detector

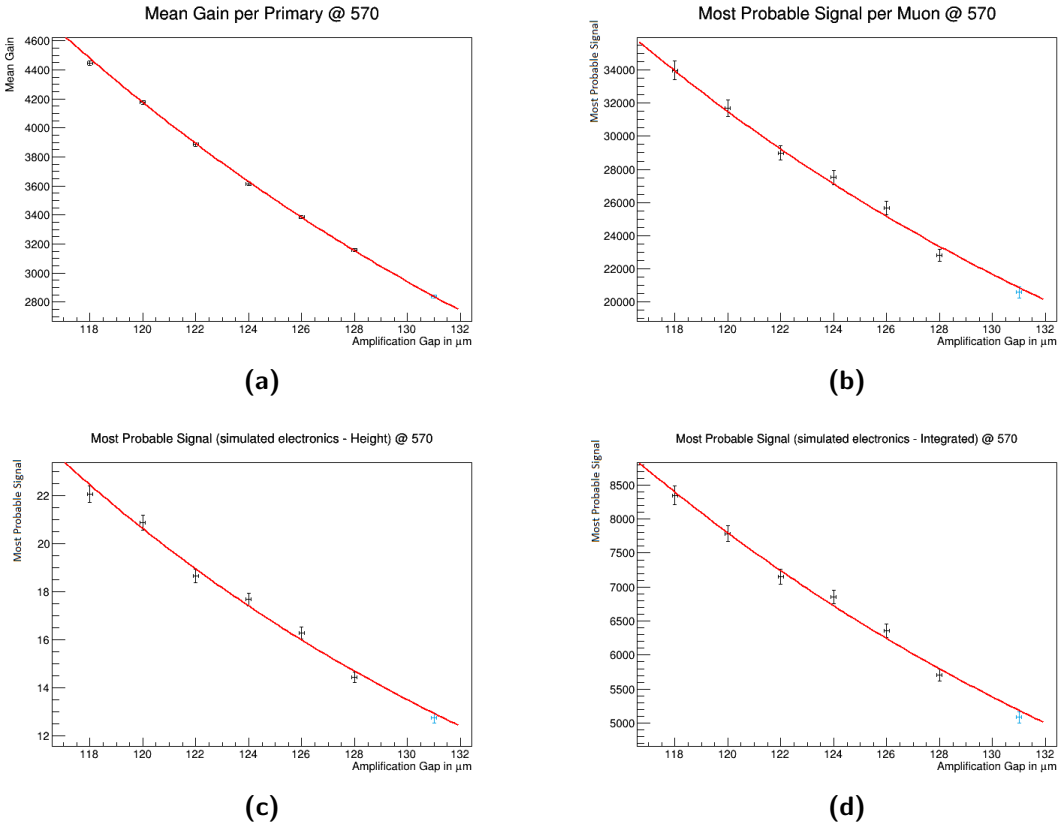

Figure 7.26.: (a) Extrapolation of the gain, (b) of the electron number, (c) of the simulated signal height, (d) of the simulated integrated signal at $U = 580$ V, for all of these the blue point at 131 µm is **not** included in the fit

exhibits a range of pillar heights, which can not be disentangled. For the real detector, therefore, the effect seen in simulation can not be reliably reproduced in the large real detector used in the NSW. A trend to lower signal strength for larger pillars, however, can be seen.

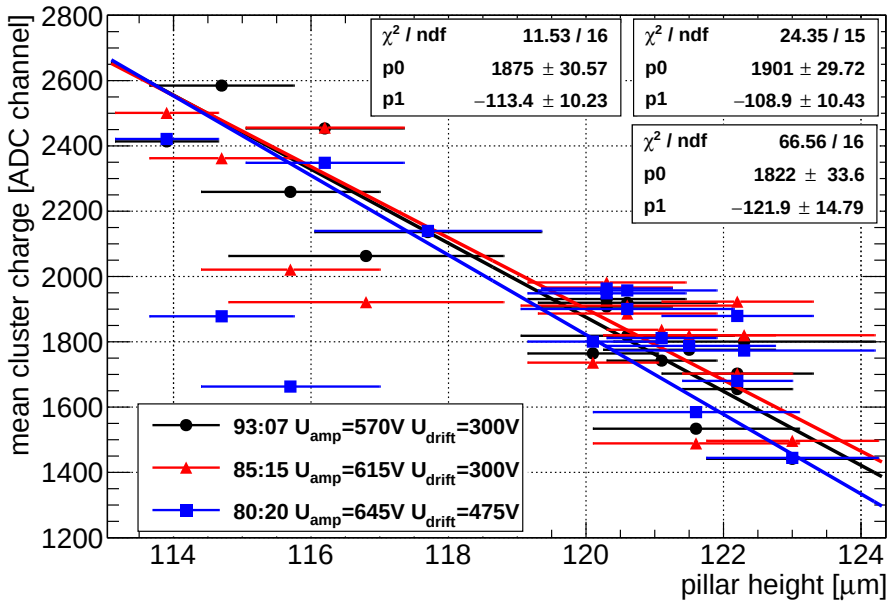

Figure 7.27.: Average signal strength depending on the average pillar height at different gas compositions and voltages. Notice the horizontal bars indicating the variation of pillar heights, from [102]

8. Conclusions and Outlook for the Construction of Detector Modules for the ATLAS New Small Wheel

The first panels were finalized in October 2017. At that point, the procedures for each step were still in development. After the initial development, trial and teaching period, the production intervalls were ramped up in early 2018. In April 2018, first problems with high voltage stability were discovered, halting the production with the exception of a few experimental panels until September that year. Several solutions to the problem had been investigated, including the sanding of the mesh to remove damages on the wires. Some changes to the procedure had been made during this time, resulting in the procedures described in chapter 7. After the investigation into the high voltage instabilities had been concluded, the production speed was increased again. The finalization of the SM2 drift panels was completed in June 2019. A more detailed timeline can be seen in 8.1.

After the experimental phase was over and the procedure was fixed in early 2018, the work load for general production was split across three physicists, and up to six undergraduate students who were employed for this task, as well as one technician from the university workshop. One production day would be performed by one physicist and two students, with support by the technician for the more technically demanding procedures, like cutting the mesh on the panel. During one of these days, all steps would be performed once, resulting in one panel(side) being finalized every work day. For each wheel, 8 sectors have to be equipped with two modules each, resulting in 48 panels per wheel, of which 16 are double sided. For both sides, this means 96 panels have to be made. In addition with six spare panels, of which one broke even before the transfer could be made, a total of 101 panels where finalized, 34 double-sided and 67 one-sided panels, for a total of 135 transferred meshes.

As of the writing of this thesis, Side A has been green-lit for integration into the detector, while quadruplets of all types are being assembled at their respective sites and the integration of sectors onto the Side C wheel has been on-going, with delays

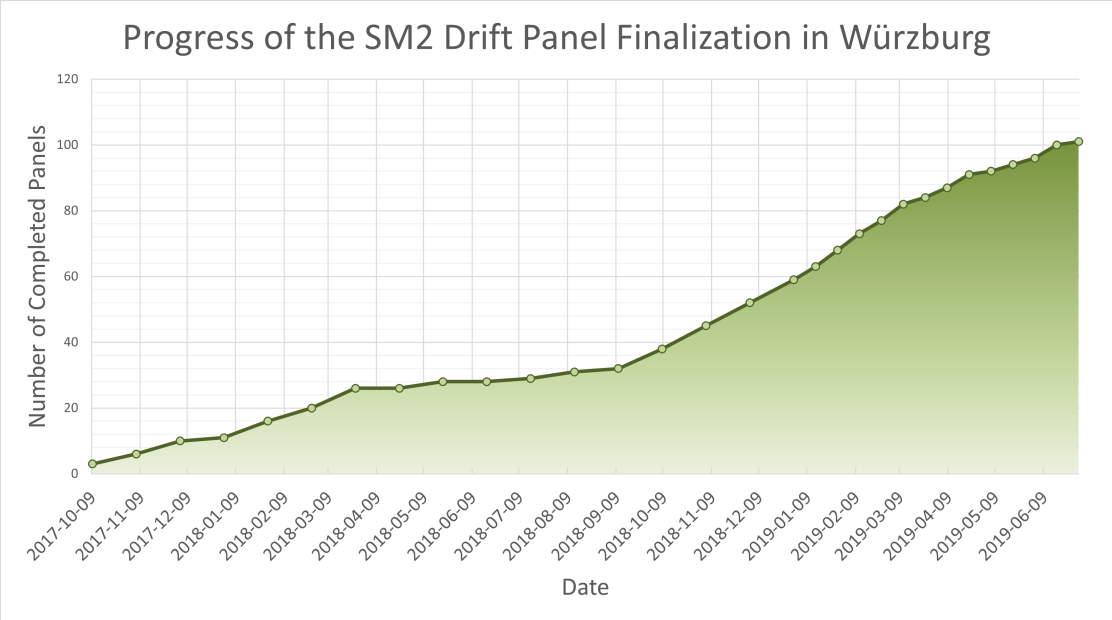

Figure 8.1.: Production progress during the SM2-production in Würzburg.

caused by complications due to the currently ongoing pandemic. The sectors are being completed and tested at CERN and every sector is tested on the wheel while the next one is prepared for integration. The first wheel is to be integrated into the detector later this year, 2021, but unfortunately, the exact timetable of the project, as with all upgrade-projects of the LHC and its experiments running at the moment, cannot be predicted due to current circumstances.

To be able to have more redundancy, several new drift panels are currently being produced. They will be equipped with meshes as soon as they are ready. This work will be performed in Munich under supervision and help from Würzburg, as the production line in Würzburg had to be shut down due to space conflicts in the cleanroom.

A. Appendix: Mesh Data Sheet

Rahmen: R11

Klebercharge: 24

Luftdruck: 2,5 bar

Mesh-Nr.: 042

Anmerkungen:

NSW SM2 Mesh Stretching Data Sheet

Tension Map [**BEFORE** Glueing]

Namen: T, JB, To Datum: 17.05.2019

	1	2	3	4	5	6	7	8
A	10,4	10,4	9,8	9,2	10,4	10,0	10,2	10,6
B	9,8	10,0	9,6	9,2	10,2	9,8	10,2	10,2
C	10,0	10,4	10,0	9,6	10,6	10,2	10,4	11,0
D	10,4	10,4	10,0	9,8	10,8	10,2	10,4	10,6
E	10,6	11,2	10,8	10,4	11,0	10,4	10,8	10,8
F	9,8	10,0	9,8	9,8	10,2	9,8	10,2	10,4

Tension Map [**AFTER** Glueing]

Namen: JB, TS, F.W. Datum: 20.05.2019

	1	2	3	4	5	6	7	8
A	10.4	10.4	9.6	9.0	10.2	9.8	10.2	10.8
B	10.0	10.2	9.4	9.2	10.0	9.6	9.8	10.4
C	10.0	10.4	9.6	9.4	10.2	10.0	10.2	10.6
D	10.4	10.2	9.8	9.6	10.2	10.0	10.2	10.4
E	10.6	10.8	10.4	10.2	10.6	10.4	10.6	10.8
F	9.8	9.8	9.6	9.4	9.8	9.6	10.0	10.2

Panel ID:

13661

Double **Single** ☐

Side1 ☐

Side2 ☒

Mesh-Nr.:

042

Anmerkungen:

Tension Map [**on Panel**]

Namen: T, J, J°

Datum: 03.06.2019

	1	2	3	4	5	6	7	8
A			12,0	10,6	10,8	11,0		
B			11,8	10,0	10,2	10,4		
C			11,0	10,2	10,4	10,8		
D			10,8	10,0	10,2	10,8		
E		11,2	10,2	9,8	10,2	10,6	11,2	
F		12,4	10,8	10,0	11,4	11,2	12,0	

NSW SM2 Mesh Stretching Data Sheet

List of Figures

Glossary

ADDC ART Data Driver Card. ASICcard used to collate the trigger data of the ATLAS NSW Micromegas modules.

ANSYS ANalysis SYStem. A multiphysics finite-elements-software used to solve problems in strucural, fluid and electromagnetic dynamics, among others. In this work it was used to generate field maps for micromegas-detector simulations.

APV25 ASIC designed in the 250 nm process. Used on front-end boards to read out particle detectors in a high rate environment.

ART Address-in-RealTime. Operations mode for the readout of Micromegas trigger signals. The Addresses of the first hit signal in the buffer are delivered immidiately to the ADDC.

ASIC Application-Specific Integrated Circuit. A integrated circuit specifically designed to only perform a given task, as opposed to general-purpose use. Examples are amplifiers or filters for signal applications.

ATLAS A Toroidal LHC AparatuS. One of the two multi-purpose experiments of the LHC at CERN, Geneva, Switzerland. The name was chosen because of its design featuring toroid magnets to create a field in the barrel region.

BNC Bayonet Neill-Concelman. A common connector type for coaxial cables, used in particle physics.

CAD Computer Assisted Design. CADis the process of using modelling software to generate components of machines or other setups before they are produced to test fit and physical properties in a cheap and comparatively fast way as opposed to prototyping.

Cathode Strip Chambers Proportional Wire Chambers with a cathode readout with strps. The distance between the cathode and the wire plance is equal to the pitch of the wires.

CERN European Organization for Nuclear Research (orig. Conseil Européen pour la Recherche Nucléaire). A international organization dedicated to nuclear and particle research, based at the border between France and Switzerland in Geneva. Founded after the second World War, it has become one of the most important centers of particle physics research with contributions coming from around the world.

CMS Compact Muon Solenoid. One of the two multi-purpose experiments of the LHC at CERN, Geneva, Switzerland. The name was chosen because of its design featuring a very compact setup featuring a solenoid creating S-shaped paths for muons in the barrel region.

CSC Cathode Strip Chambers. Used in the innermost sections of the ATLAS Small Wheel instead of MDT chambers. They exhibit lower dead times and are therefore especially suited for the high rate environment after the high-luminosity LHC upgrade.

DCS Detector Control System. The central control system of the ATLAS detector. The status of all detectors is monitored and configurations are made through this system.

FEB Front-End Board. The pFEBs and the sFEBs are two of the FEB-types used to read out the sTGCs in the ATLAS NSW.

FEC Front-End Concentrator. Part of the SRS readout system. Takes signals from up to 16 APV25s, digitizes them and concentrates them before the data is transferred to the readout computer.

FELIX Front-End Link Interface eXchange. Used to both forward trigger data to the central ATLASmuon system sector logic and to form events out of the read out data.

FPGA Field Programmable Gate Array. An integrated circuit which consists of an array of many logic units which can be reprogrammed *in the field* as needed. A middle ground, slower, but cheaper than an ASIC and faster than a standard computer.

Garfield++ C++ implementation of Garfield, a simulation tool for the simulation of gaseous detectors

GEM Gas Electron Multiplier. A type of MPGD that uses a perforated insulating foil with copper layers on both sides to create an amplification volume inside the holes of the foil. Multiple GEM-foils can be stacked to create high gains inside the detecor. A striped readout anode allows for positional reconstruction of clusters.

HEED Program used to calculate the secondary ionisation of media after primary ionisation.

HL-LHC High Luminosity upgrade of the LHC. To increase the phase space that can be accessed in analyses with the LHC, it will be upgraded around 2025 to increase the amount of collisions per second in the detectors.

IBM 130 nm Process A process for the production of electronics components with structure sizes of around 130 nm. As of this date, 5 nm processes have been realized commercially. They are however, not suited for high-radiation environments, which is why the 130 nm process was used for the NSW-detectors.

L1DDC Level 1 Data Driver Card. The L1DDCis used to send the readout data from all ATLAS NSWmodules to the FELIX.

LabView Laboratory Virtual Instrument Engineering Workbench. A graphial programming language from National Instruments used primarily in laboratories for data aquisition and experiment control purposes.

LEP Large Electron Positron accelerator. Accelerated electrons and positrons to up to 209 GeV, used to find the Z-boson. Closed down in 2000 to make space for the LHC.

LHC Large Hadron Collider. The to-date largest particle accelerator build underground at CERN, close to Geneva, Switzerland. It can collide protons and ions at unprecented energies with a goal to access new physics beyond the standard model.

Magboltz Program developed by Stephen Biagi used to generate drift properties of electrons in gases for simulation purposes. The program uses a variety of gas properties to calculate the drift of electrons in a given gas mixture.

MCA Multi Channel Analyzer. A digitizer for signal heights. The height of the input signal is converted into a channel number and send to the PC. In applications where the signal height is proportional to the energy of the particle, the resulting spectrum is an energy spectrum.

MDT Monitored Drift Tube. An evolution of the geiger-müller counter. It is used in the proportionality gain region and fast enough to resolve several clusters of charges generated by a single particle. This allows more precise tracking of the particle.

MFC Mass Flow Controller. Controllers that can regulate the flow of a gas by measuring the force exerted onto a bend pipe. To apply this method, the gas composition must be known.

MicroMeGas Micromesh Gaseous Detector. A type of MPGD using a steel micromesh to separate a small amplification gap of the order of 100 µm from the large drift volume. This confines the ion drift to the amplification gap, reducing dead times. A striped readout anode allows for positional of clusters.

MM400 Device to measure the water vapor content in process gas, produced by Systech Illinois, Ltd.

mmDAQ Readout software for the SRS system. It provides online analysis tools to check the data while it is taken and saves .root files for further analysis.

MMFE8 Micromegas Front-End 8. Front end card for the ATLAS NSW micromegas modules. Contains 8 VMM chips.

MPGD Micropattern Gaseous Detectors. A class of gaseous detectors using micropatterned readouts to allow for spatial resolution in at least one dimension.

NIM Nuclear Instrumentation Modules. A standard for nuclear instrumentation created to unify lab equipment.

NSW New Small Wheel. Replacement of the Small Wheel currently placed in the ATLAS-detector for the high-luminosity LHC-upgrade. To be able to cope with the high rate environment, both sTGCs and micromegas detectors are used.

PCB Printed Circuit Board. Fiberglass board used to implement electronic circuits, used in electronics from home PCs to highly specialized ASICs.

PS Proton Synchrotron. Built in 1959, providing 28 GeV protons to experiments. Still serving today, providing protons to the SPS and subsequently the LHC.

ROC Read-Out-Controller. Used on the front end boards to aggregate the data after a trigger. It will be reformatted before it is handed to the L1DDCto be sent to the FELIX

ROOT Library for C++ used for analysis tasks in particle physics, developed at CERN. This includes data organization, plotting and fitting, among others.

RPC Resistive Plate Chamber. Due to its simplicity very robust and fast detector technology used in the Barrel region of the ATLAS detector for triggering.

SC Synchrocyclotron. The first accelerator built by CERN in 1957.

SCA Slow Control Adapter. Used to send configuration commads to detector modules and to send detector information to the DCS.

SHV Save High Voltage. Connector type used for coaxial cable carrying high voltage. The outer conductor is grounded, while the inner conductor carries the voltage. Both male and female connectors are protected in such a way that the end of the inner conductor cannot be accidentally touched by anyone handling the cable.

SM2 Small Module 2. One of the four different micromegas modules for the NSW. It is part of the small sector, forming the outside part of one wedge. The SM2 is produced by a collaboration of German universities.

SPS Super Proton Synchrotron. Started in 1976, provides protons to several experiments and the LHC.

sTGC small strip Thin Gap Chamber. An evolution of the TGCs used in the ATLAS detector, using smaller strips to improve spatial resolution.

SRS Scalable Readout System. Readout system for particle detectors designed to be scalable so it can both be used in small labs and large experiments. It contains a variable number of front-end-cards that are connected to the on-detector APV25 chips as well as the measurement PC.

SRS Scalable Readout Unit. Central unit that coordinates all FEC cards in an SRS system.

TDC Time to Digital Converter. Allows to measure the time between two NIM signals. The time is digitized and transferred to the measurement PC.

TDS Trigger Data Serializer. Exists in both strip and pad variants. The TDS is located on the corresponding FEB and serializes the trigger data before it is send to the rim electronics.

TGC Thin Gap Chamber. A type of multiwire proportional chamber in which the distance between the wire and the electrodes is smaller than the wire pitch. This allows for faster readout of the detector compared to regular setup.

UDP User Datagram Protocol. A network communication protocol in which the sender sends and forgets the data packet and does not check, if it reaches its destination. Used in the SRS system to facilitate fast data transfer without overhead.

VMM ASIC designed specifically for the needs in the ATLAS NSW upgrade project as a replacement for the APV25. Used on front-end boards for read out off all NSW-detectors.

ZR800 Device to measure the water vapor content in process gas, produced by Systech Illinois, Ltd.

Bibliography

[1] High Luminosity LHC. https://hilumilhc.web.cern.ch/content/hl-lhc-project. Accessed 2020-11-10.

[2] H. Geiger E. Rutherford. An electrical method of counting the number of α particles from radioactive substances. *Proceedings of the Royal Society*, 81, 1908.

[3] W. Müller H. Geiger. Elektronenzählrohr zur Messung schwächster Aktivitäten. *Die Naturwissenschaften*, 16, 1928.

[4] C. Grupen, B. Schwartz. *Particle Detectors*. Cambridge University Press, Second edition, 2011.

[5] W. Blum, W. Riegler, L. Rolandi. *Particle Detection with Drift Chambers*. Springer-Verlag Berlin Heidelberg, Second edition, 2011.

[6] B. Sitar et al. *Ionization measurements in High Energy Physics (in Russian)*. Energoatomizdat, Moskau, 1988.

[7] B. Sitar et al. *Ionisation Measurements in High Energy Physics*, volume 124. Springer Tracts in Modern Physics, 1993.

[8] H.A. Bethe. Theorie des Durchgangs schneller Korpuskularstrahlen durch Materie. *Ann. d. Physik*, 5, 1930.

[9] H.A. Bethe. Bremsformel für Elektronen mit relativistischen Geschwindigkeiten. *Z. Physik*, 76, 1932.

[10] H.A. Bethe. Bremsvermögen von Atomen mit mehreren Elektronen. *Z. Physik*, 81, 1933.

[11] R.M. Sternheimer, R.F. Peierls. General Expression for the Density Effect for the Ionization Loss of Charged Particles. *Phys. Rev. B*, 3, 1971.

[12] E.A. Uehling. Penetration of Heavy Charged Particles in Matter. *Ann. rev. Nucl. Part. Sci.*, 4, 1954.

[13] M. Tanabashi et al. Review of particle physics. *Phys. Rev. D*, 98:030001, Aug 2018.

[14] S. Behrends, A.C. Melissinos. *Properties of Argon-Ethane/Methane Mixtures for Use in Proprotional Counters*. University of Rochester, Preprint, 1981.

[15] J.E. Moyal. Theory of Ionization Fluctuations. *Phil. Mag.*, 46, 1955.

[16] R.K. Bock et al. (eds.). Formulae and Methods in Experimental Data Evaluation. *General Glossary, European Physical Society, CERN/Geneva*, 1, 1984.

[17] G. Musiol et al. *Kern- und Elementarteilchenphysik*. VCH Verlagsgesellschaft, 1988.

[18] U. Fano. Ionization Yield of Radiations. II. The Flucuations of the Number of Ions. *Phys. Rev.*, 72, 1947.

[19] B. Rossi. *High Energy Particles*. Prentice-Hall, Englewood, 1952.

[20] Warrier, Anita and Vijayan, Prof. C. Taking light for a walk. *Resonance*, 18, 11 2013.

[21] P.A. Cherenkov. Visible Radiation Produced by Electrons Movin in a Medium with Velocities Exceeding that of Light. *Phys. Rev.*, 52, 1937.

[22] P. MArmier, E. Sheldon. *Physics of Nuclei and Particles*, volume 1. Academic Press, New York, 1969.

[23] O. Klein, Y. Nishina. Über die Streuung von Strahlung durch freie Elektronen nach der neuen relativistischen Quantenmechanik von Dirac. *Z. Phys.*, 52, 1929.

[24] W.S.C. Williams. *Nuclear and Particle Physics*. Clarendon Press, Oxford, 1991.

[25] G. Hertz. *Lehrbuch der Kernphysik*. Teubner, LEipzig, 1966.

[26] R.D. Evans. *The Atomic Nucleus*. McGraw-Hill, New York, 1955.

[27] J. Townsend. *Electrons in Gases*. Hutchinson, 1947.

[28] F. Sauli A. Peisert. *Drift and Diffusion in Gases: A Compilation*. CERN-84-08, 1984.

[29] D.S. Toffolo J.M. Kirshner. Drift Velocity of Electron in Argon and Argon Mixtures. *J. Appl. Phys.*, 23, 1952.

[30] G. Polya F. Eggenberger. Über die Statistik verketteter Vorgänge. *Z. Angew Math Mech*, 4, 1923.

[31] R. Veenhof H Schindler, S.F. Biagi. Calculatinon of Gas Gain Fluctuations in Uniform Fields. *Nuclear Instruments and Methods in Physics Research A*, 624, 2010.

[32] Heinrich Schindler. *Microscopic Simulation of Particle Detectors*. PhD thesis, Technische Universität Wien, 2012.

[33] Fabian Kuger. *Signal Formation Processes in Micromegas Detectors and Quality Control for large size Detector Construction for the ATLAS New Small Wheel*. PhD thesis, Julius-Maximilians-Universität Würzburg, 2017.

[34] F.M. Penning. Über Ionisation durch metasabile Atome. *Naturwissenschaften*, 15, 1927.

[35] T.Z. Kowalski. Analytical approach and calculation of gas gain in ar-CO2 mixture. *Journal of Instrumentation*, 15(07):P07008–P07008, jul 2020.

[36] Ö Şahin, İ Tapan, E N Özmutlu, and R Veenhof. Penning transfer in argon-based gas mixtures. *Journal of Instrumentation*, 5(05):P05002–P05002, may 2010.

[37] H. Raether. *Electron avalanches and breakdown in gases*. Butterworths, London, 1st Editiion edition, 1964.

[38] C.G. Montgomery, D.D. Montgomery. The Discharge Mechanism of Geiger-Mueller Counters. *Physical Review*, 57, 1940.

[39] S.A. Korff. Operation of Proportional Chambers. *Journal of the Franklin Institute*, 232(1), 1941.

[40] M.E. Rose and W.E. Ramsey. The Behaviour of Proportional Counters Amplification at Low Voltages. *The Physical Review*, 61(198), 1942.

[41] E. Iarocci. Plastic Streamer Tubes and their Application in High Energy Physics. *Nuclear Instruments and Methods in Physics Research A*, 217(30), 1983.

[42] R. Baumgart, C. Grupen, U. Schäfer. Properties of Streamers in Streamer Tubes. *Nuclear Instruments and Methods in Physics Research*, 222(3), 1984.

[43] P. Rieck. Design, Construction and Test of Small-Diameter Muon Drift Tube Chambers (sMDT) for the Phase-1 Upgrade of the ATLAS Muon Spectrometer. *Nucl. Instrum. Meth. A*, 958, 2020.

[44] Y. Giomataris, Ph. Rebourgeard, J.P. Robert, and G. Charpak. Micromegas: a high-granularity position-sensitive gaseous detector for high particle-flux environments. *Nuclear Instruments and Methods in Physics Research Section A: Accelerators, Spectrometers, Detectors and Associated Equipment*, 376(1):29 – 35, 1996.

[45] J.A. Harvey O. Bunemann, T.E. Cranshaw. Design of Grid Ionization Chambers. *Canadian Jounral of research A*, 27, 1949.

[46] H.Raether. Die entwicklung der Elektronenlawine in den Funkenkanal. *Zeitschrift für Physik*, 112, 1939.

[47] P. Fonte, V. Peskov. Summary of what is known about discharges in MPGDs and what will be important to study in the frame of WG2 of the RD51. *Technical Report, CERN*, 2009.

[48] Th. Alexopoulos et al. A spark-resistant bulk-micromegas chamber for high-rate applications. *Nuclear Instruments and Methods in Physics Research*, 640, 2011.

[49] A. Bressan et al. High rate behavior and discharge limits in micropattern detectors. *Nucl. Instrum. Methods A*, 424, 1999.

[50] S. Bachmann et al. Discharge mechanisms and their prevention in the gas electron multiplier (GEM). *Nucl. Instrum. Methods A*, 479, 2002.

[51] The CMS Collaboration. CMS Tchnical Design Report for the Muon Endcap GEM Upgrade. Technical report, CMS, 2015.

[52] H.R. Byers et al. *Compendium of Meteorology.* American Meteorological Society, Boston, 1951.

[53] H.A. Skinner H.O. Pritchard. The concept of electronegativity. *Chemical Reviews*, 55(4):745–786, 1955.

[54] Open-Access Database of Gas Properties, lxcat.net.

[55] N. Skoro, D. Marić, Dragana, G. Malovic, W. Graham, Z. Petrović. Electrical breakdown in water vapor. *Physical review. E, Statistical, nonlinear, and soft matter physics*, 84:055401, 11 2011.

[56] Thorwald Klapdor-Kleingrothaus. *Gas Gain Studies for MicroMegas Detectors and Development of the High Voltage Control System for the Detectors of the ATLAS New Small Wheel Upgrade.* PhD thesis, Albert-Ludwigs-Universität Freiburg, 2019.

[57] Stefan Weber. *Simulation Studies on the New Small Wheel Shielding of the ATLAS Experiment and Design and Construction of a Test Facility for Gaseous Detectors.* PhD thesis, Julius-Maximilians-Universität Würzburg, 2016.

[58] CAEN SpA. *SY2527 Universal Multichannel Power Supply System*, 2012.

[59] CAEN SpA. *A1535/AG535 - 24 Channel 3.5 kV/ 3 mA High Voltage Boards*, 2015.

[60] CAEN SpA. *A7236 AG7236 32 Channel 3.5 kV/1.5 mA (4W) Power Supply Boards*, 2020.

[61] Louis Costrell. Standard Nuclear Instrument Modules. Technical report, National Bureau of Standards, 1964.

[62] U.S. Nim Committee. Standard NIM Instrumentation Modules. Technical report, U.S. Department of Energy, 1990.

[63] CAEN SpA. *N842/N843 8/16 Channel Constant Fraction Discriminators*, 2015.

[64] Phillips Scientific. *Octal Multifunction Logic Unit Nim Model 757.*

[65] Mesytec GmbH & Co. KG. *MTDC-32 (data sheet v2.6_05)*, 2005.

[66] S Martoiu, H Muller, A Tarazona, and J Toledo. Development of the scalable readout system for micro-pattern gas detectors and other applications. *Journal of Instrumentation*, 8(03):C03015–C03015, mar 2013.

[67] J. Fulcher et al. M. Raymond, M. French. The APV25 0.25 µm CMOS readout chip for the CMS tracker. In *2000 IEEE Nuclear Science Symposium. Conference Record (Cat. No.00CH37149)*, volume 2, pages 9/113–9/118 vol.2, 2000.

[68] A Zibell. Development of a read out driver for ATLAS micromegas based on the scalable readout system. *Journal of Instrumentation*, 9(01):C01038–C01038, jan 2014.

[69] CAEN SpA. *A422-A422A Charge Sensitive Preamplifier with Timing (Box), Rev. 2*, 2014.

[70] CAEN SpA. *N968 Spectroscopic Amplifier*, 2016.

[71] Amptek, Inc. *MCA800D Manual*.

[72] Stefan Czerwenka. Aufbau eines Gassystems für Gasdetektoren im Rahmen eines Höhenstrahlungsteststandes. Master's thesis, Julius-Maximilians-Universität Würzburg, 2015.

[73] Florian Wirth. Untersuchung der Verunreinigung von Micromegagas mit Wasser und Sauerstoff durch Kunststoffschläuche, 2019.

[74] Systech Instruments Ltd. *MM400 Series Operation Manual v3.4*, 2017.

[75] Systech Instruments Ltd. *MM400 Series Operations Manual*, 2017.

[76] Robin Boshuis. Untersuchungen der Gasverstärkung in Micromegas-Detektoren als Funktion des Gasdrucks. Master's thesis, Julius-Maximilians-Universität Würzburg, 2018.

[77] International Organization for Standardization. ISO3669:2020, Vacuum technology - Dimensions of knife-edge flanges. Technical report, ISO, 2020.

[78] Bronkhorst. *EL-PRESS series Digital Pressure Meters and Controllers, 9.17.101 rev. I*, 2020.

[79] CERN MPGD Service. https://ep-dep-dt.web.cern.ch/micro-pattern-technologies. Accessed 2020-11-10.

[80] Thomas Schell. Bau und Charakterisierung resistiver Micromegas Detektoren, 2018.

[81] P.F. Green K.T. Gillen. Moisture Permeation of Environmental Seals Used in Weapons. Technical report, Sandia National Laboratories, 1992.

[82] J. Crank. *The Mathematics of Diffusion*. Oxford University Press, 1975.

[83] H. Schindler. *Garfield++ User Guide, Version 2020.4*, 2020.

[84] S.F. Biagi. Monte Carlo simulation of electron drift and diffusion in counting gases under the influence of electric and magnetic fields. *Nucl. Instr. Meth. A*, 421, 1999.

[85] A. Rotondi, P. Montagna. Fast calculation of Vaviov distribution. *Nucl. Instr. Meth. B*, 47, 1990.

[86] Keysight Technologies. *33210A Function/Arbitrary Waveform Generator User Guide*, 2020.

[87] Esma Mobs for CERN. The CERN accelerator complex. CERN-GRAPHICS-2019-002, 2019.

[88] G. Aad et al for the ATLAS Collaboration. Observation of a new particle in the search for the Standard Model Higgs boson with the ATLAS detector at the LHC. *Physics Letters B*, 716(1):1 – 29, 2012.

[89] The ATLAS Collaboration. ATLAS Muon Spectrometer - Technical Design Report. Technical report, ATLAS, 1997.

[90] Jao Pequenao for the ATLAS Experiment. Computer generated image of the whole ATLAS detector. CERN-GE-0803012, 2008.

[91] The ATLAS Collaboration. ATLAS New Small Wheel - Technical Design Report. Technical report, ATLAS, 2013.

[92] F. Bauer, U. Bratzler, H. Dietl, H. Kroha, Th. Lagouri, A. Manz, A. Ostapchuk, R. Richter, S. Schael, S. Chouridou, and et al. Construction and test of MDT chambers for the ATLAS muon spectrometer. *Nuclear Instruments and Methods in Physics Research Section A: Accelerators, Spectrometers, Detectors and Associated Equipment*, 461(1-3):17–20, Apr 2001.

[93] A. Di Ciaccio. The ATLAS RPC trigger chamber system. *Nucl. Instrum. Meth. A*, 572:48–49, 2007.

[94] Bhattacharya, Deb. The Micromegas chambers for the ATLAS New Small Wheel upgrade. *Physica Scripta*, 95:6, 07 2020.

[95] G. Iakovidis on behalf of the ATLAS-Muon-Collaboration. VMM - An ASIC for Micropattern Detectors. *ATL-MUON-PROC-2015-015*, 2015.

[96] P. Gkountoumis. Electronics design and system integration of the ATLAS New Small Wheels. *Journal of Instrumentation*, 12(01):C01088–C01088, Jan 2017.

[97] J. Anderson et al. FELIX: a High-Throughput Network Approach for Interfacing to Front End Eletronics for ATLAS Upgrades. *Journal of Physics: Conference Series*, 664, 2015.

[98] R.-M. Coliban, S. Popa, T. Tulbure, D. Nicula, M. Ivanovici, S. Martoiu, L. Levinson, and J. Vermeulen. The read out controller for the ATLAS new small wheel. *Journal of Instrumentation*, 11(02):C02069–C02069, feb 2016.

[99] Panagiotis Gkountoumis. Level-1 Data Driver Card of the ATLAS New Small Wheel upgrade compatible with the Phase II 1 MHz readout scheme. In *5th International Conference on Modern Circuits and Systems Technologies*, 2016.

[100] J. Bortfeldt. Construction and test of full-size Micromegas modules for the ATLAS New Small Wheel Upgrade. *EPJ Web Conf.*, 174:01003, 2018.

[101] L. Longo. Production and test of Micromegas boards. ICHEP, 2020.

[102] Maximilian Georg Herrmann. *Series Calibration of segmented and multi-layered Micromegas Modules for ATLAS*. PhD thesis, Ludwig-Maximilians-Universität München, 2019.

Acknowledegements

I would like to use the last pages of this thesis to express my gratitude to people who have supported me either professionally or on a personal level.

First of all, I extend my thanks to *Thomas Trefzger* and *Raimund Ströhmer* for giving me the opportunity to join their group to work on the cutting edge of particle physics. Especially the latter I thank for his excellent support whenever question about physics arose and the many very enlightening discussions we had.

I also express my gratitude to my colleagues for the support I recieved, especially *Gia Khoriauli* and *Deb Sankar Bhattacharya* and *André Zibell*. Their support in the lab and in the clean room was always welcome and, especially in the case of the mass production, helped our group to keep the schedule of production. In addition to them, the manpower and expertise provided by the workshop of the faculty of Physics and Astronomy of the University Würzburg has been instrumental in the construction of components for both ATLAS detector production and the lab. In particular, I would like to thank *Utz Baß*, *Carsten Bergmann*, *Rainer Brauner* and *Jürgen Weidner* of the workshop for their support, especially with the SM2, for which they provided significant manpower. I would also like to thank all the students who joined the team for the project as *HiWis*.

To *Martin Kamp* my thanks go for providing space in the clean room of the Wilhelm Conrad Röntgen Research Center for Complex Material Systems, the demands for which grew as the responsibilities of the Würzburg group in the project grew larger and larger.

I also thank *Rui de Oliveira* of the CERN gaseous detector workshop for providing the kits for the resistive Micromegas detectors used in the lab and *Paul Colas*, *David Attié*, *Mariam Bebbiri* and *Stephan Aune* from CEA Saclay and their workshop for the bulk Micromegas detectors.

The construction of the detector modules was a massive effort, of which only parts were performed in Würzburg. I would like to thank everyone in the NSW-community for the incredible effort they put into the project. In particular, the other groups involved in the construction of the SM2, from the *Ludwig-Maximilians-Universität Munich*, the *Johannes Gutenberg-Universität Mainz* and the *Albert-Ludwigs-Universität Freiburg*, I would like to thank for their close collaboration.

The entire project would not have been possible without the untiring effort shown by the late *Stephanie Zimmermann*, whose sudden death shook us all to the core. I would like to dedicate the construction part of this thesis to her memory.

On the personal side, I would first and formost thank my parents, Bettina and Burkhard Swirski, for their unwavering and unconditional support for now more than 30 years of my life. Without them I would not have been able to get to where I am now.

I would also like to thank all colleagues who have become friends and the people I would not have met if I had not taken up this position in Würzburg. I will always fondly remember the after-work board game evenings *Stephan Lück*, *Burkhard Böhm*, *Lucas Klein* and I had together, which sadly had to be put on hold during the pandemic. Also, I would like to thank *Firas Bdiwi*, who with his always welcoming and positive attitude, and some Arabian tea, helped me throuh the more stressfull times, of which there are always plenty in such a project. *Stefanie Wucherer* I would like to thank for her emotional support and great friendship, which made an already special time here in Würzburg even more enjoyable.